Characterization of Flat-Wall Impinging Fuel Spray under High-Pressure Cross-Flow Condition

(高圧横風気流中で平板に衝突する燃料噴霧の特性)

by

Zhanbo SI

Dissertation

Submitted to the Graduate School of Engineering
Hiroshima University
in Partial Fulfillment of the Requirements
For the Degree of

Doctor of Engineering
Hiroshima University
September, 2018

ABSTRACT

Owing to the advantages of good fuel economy and high thermal efficiency, direct injection (DI) gasoline engines have widely been applied in the automotive field. The DI gasoline engines include two combustion modes: stratified charge combustion and homogeneous combustion. In either mode, the air flow movement in the cylinder is strong enough to influence the fuel spray characteristics, such as spray profile, spray breakup, and fuel–air mixing. In addition, the fuel spray might impinge on the piston cavity wall before being fully vaporized due to the high injection pressure and small cylinder. Spray impingement usually influences fuel atomization and combustion, resulting in excessive hydrocarbon (HC) and soot emissions. To examine the effect of cross-flow on the impingement spray characteristics, such as the spray structure, droplet size and velocity distributions, a comprehensive experimental investigation was carried out in a high-pressure wind tunnel. The impingement spray images in a vertical plane and two horizontal planes were recorded by a high speed video camera and a laser sheet technology. By employing the particle image analysis (PIA) optical diagnostic method, the Sauter mean diameter (SMD) and the droplet velocity components were investigated. The main conclusions are summarized as following.

By observing the spray structure in vertical plane, is can be seen that with the increase in cross-flow velocity, the spray area increases significantly, i.e., the cross-flow favors spray dispersion. Moreover, the spray outline distortion caused by cross-flow in the leeward side is larger than that in the windward side. Under the almost same liquid-to-air momentum flux ratio q, when the ambient pressure and cross-flow velocity were varied, the impingement spray outlines in the windward side were almost coincident, particularly at the upper part, but in the leeward side, the outline extended further at lower ambient pressure. With increase in the cross-flow velocity before impingement, the spray tip penetration decreased slightly, while it evidently increased after impingement. The increased cross-flow velocity led to an increase in the vortex height because of the enhanced spray dispersion. The high ambient pressure restrains the spray dispersion and leads to a shorter spray tip penetration and smaller vortex height. From the spray images observation in two horizontal planes, we found that in the plane of y = 25 mm, the movement of the Karman vortex-like structure was observed that resulted in a non-uniform distribution of droplets in the

upper part of the spray in the leeward side. In the plane of y = 45 mm, in the vortex core region, the droplets density was quite low, showing an empty belt.

Droplet size and velocity distributions were measured by employing the PIA system. The results show that the increased cross-flow velocity leads to larger SMD in the windward side of spray and smaller SMD in the leeward side of spray. The two velocity components demonstrate a difference in the behavior of large and small droplets. The smaller droplets are more easily affected by the cross-flow than the larger droplets owing to their larger drag acceleration. The increased cross-flow velocity leads to the droplet splash region shifting to the downstream side, where numerous secondary droplets are formed during impinging. By employing the PIV optical diagnostic method, the flow field of wall-jet vortex was measured. In the quiescent cross-flow velocity ambient the droplet velocity distribution in spray tip formed as a vortex structure after impingement, while the vortex structure of droplet velocity disappeared with the increase of cross-flow velocity. Moreover, a stagnate region exists between the main spray and wall-jet vortex, and the droplets velocity in this region is almost 0 m/s. For near-field spray, the image at a higher ambient pressure shows few ligaments and droplets. The spray outline was wider at the initial stage (0.05 ms ASOI) than that at steady stage (2 ms ASOI) of spray evolution.

The numerical simulations were conducted by the validated spray models based on the CONVERGE software. The simulation results about spray structures, spray tip penetration, vortex height and velocity distributions have been shown and compared with the experiment results.

ACKNOWLEDGMENTS

Firstly, I would like to express my sincere gratitude to my academic advisor Professor Keiya Nishida for his continuous support, guidance and motivation of my PhD study throughout the three years. When I was at the Fluid Engineering and Spray Technology Laboratory, University of Hiroshima, Professor Keiya Nishida has given me so much encouragement and advice in all the time of my research and writing of this dissertation. I extremely proud to have the opportunity to make a research with Professor Keiya Nishida.

Besides my advisor, I would like to thank Professor Youichi Ogata. I have a pleasant time to study with Professor Youichi Ogata in a team. I admire him for his patience and immense knowledge. He has given me some suggestions in the aspect of velocity distribution in the wall-jet vortex region. I would like to thank Dr. Min Guo for his patiently help and advice in my research and daily life for my first year in Japan. I would like to thank my team members Mr. Nagisa Shimasaki and Mr. Yuji Ashida. Without their cooperation, I cannot finish so many experiments in three years. I would like to thank Dr. Jaeheun Kim and Mr. Hongliang Luo for the kind help not only in researches but also in daily life. I would like to thank our Fluid Engineering and Spray Technology Laboratory members for their help. During my study in this three years in Japan, I had the pleasure of learning with them.

I would like to express my sincere gratitude to my parents, sister and my girlfriend. Without their support and encouragement, I would not finish my study in Japan.

Last and not least, my sincere thanks also goes to the staff in Hiroshima University. They provided a very nice environment for us to study in University.

TABLE OF CONTENTS

NOMENCLATURES

A_{drop}	Sum of all droplet surface areas (m^2)
d	Nozzle hole diameter (m)
d_s	Sac hole diameter (m)
D	Diameter of the spray beam (m)
F	Force (N)
H	Spray vortex height (mm)
i	The ith sample
I	Laser intensity (W/cm^2)
L_w	Impingement distance (mm)
L_C	Liquid cone length (m)
N	Total number of sample
m	Mass (kg)
P_{inj}	Injection pressure (Pa)
P_a	Ambient pressure/Atmospheric pressure (Pa)
q	Liquid-to-air momentum flux ratio ($\rho_l U_l / \rho_g U_x$)
Q	Air flowrate (m^3/s)
r	Radius of inlet edge of nozzle hole (m)
Re	Reynolds number
t	Time (after the start of injection, s)
t_{break}	Time when liquid jet begins to disintegrate (s)
t_d	Injection duration (s)
T	Temperature (K)

T_a	Ambient temperature (K)
We	Weber number
X	A constant horizontal distance (mm)
u	Velocity component in x axis (m/s)
v	Velocity component in y axis (m/s)
Ux	Cross-flow velocity (m/s)
U_x	Mean velocity of cross-flow (m/s)
μ	Dynamic viscosity (mm^2/s)
ρ_g	Gas density (kg/m^3)
ρ_l	Liquid densities (kg/m^3)
σ	Surface tension (N/m)
Φ	Spray cone Angle (˚)
ΔP	$\Delta P=P_{inj}-P_a$, pressure drop across the nozzle (Pa)
ASOI	After Start Of Injection
CFD	Computational Fluid Dynamics
DISI	Direct Injection Spark Ignition
EGR	Exhaust Gas Recirculation
GDI	Gasoline Direct Injection
HCCI	Homogenous Charge Compression Ignition
HSV	High Speed Video
ILIDS	Interferometric Laser Imaging for Droplet Sizing
LDA	Laser Doppler Anemometry
LDSA	Laser Diffraction Size Analyzer

LEA	Laser Extinction and Absorption
LIEF	Laser Induced Exciplex Fluorescence
PDA	Phase Doppler Analyzer
PFI	Port Fuel Injection
PLIF	Planar Laser Inducted Fluorescence
PIA	Particle Image Analyzer
PIV	Particle Image Velocimetry
PTV	Particle Tracking Velocimetry
SMD	Sauter Mean Diameter
VCO	Valve Covered Orifice

Chapter 1 Introduction

1.1 Background and Motivation

1.1.1 Energy and environment

Energy is considered as one of the most important development element that is focused by human beings all the time. In addition, environmental problems, which accompany with the development of population growth and economic, are mainly caused by the fossil energy use. Fossil fuel is one of the buried combustible organic materials, which is produced from decayed plants and animals by exposure to heat and pressure in the crust of the earth over thousands and millions of years. The forms of fossil fuel include crude oil, coal, natural gas, heavy oils and so on. Fossil fuel as the non-renewable source that will be used up in many years. When the fossil fuel is depleted, the downstream industries will be influenced. Additionally, the use of the fossil fuel leads to the pollution for the natural environment that the mankind depends on living. Another indisputable fact is the climate warming, which has been reported by many researchers [1-3]. The emission of greenhouse gas is seen as the main reason of the climate warming. Environment is polluted by the greenhouse gases and harmful gases, which harm the health of human beings. It is significantly important to improve energy heat efficiency and develop clean energy for reducing the greenhouse gas emission.

With the increase of the population the world energy demand is increased. There is a research from ExxonMobil [4], following the tendency of the last two decades the energy demand will increase to 1300 quadrillion BTUs (British thermal unit) in 2040 (see Figure 1.1). If the energy conservation and efficient energy can be used implement well, in 2040 the energy demand will decrease to less than 700 quadrillion BTUs. It is interchangeable between the energy conservation and the energy efficiency, the former method proposes people to consume less energy, for example turning your lights off; however, the latter is consuming energy more effectively using different technologies (Energy conservation vs. energy efficiency, 2014). The energy consumption will lead to a series of problems. Because of acquiring from coal and oil the fossil fuel will be exploited excessively. For a long time in the future, although the renewable energy will be used, the main energy is still fossil fuel.

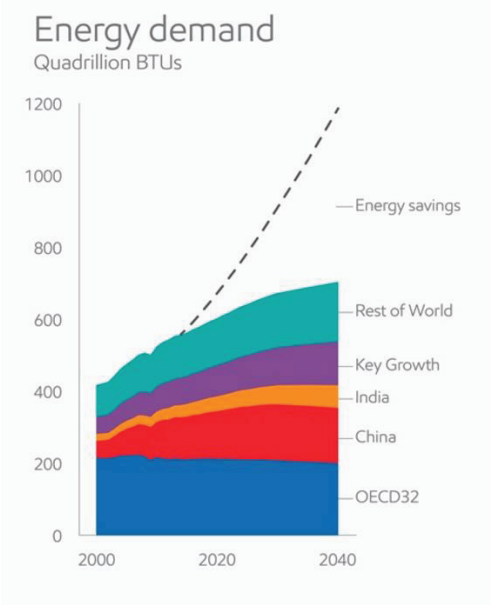

Figure 1.1 Global energy demand forecast [4].

Transportation includes rail, marine, heavy duty, and light duty use the energy. As shown in the Figure 1.2, the main energy consuming sectors include the heavy duty and light duty now and in the future. The main energy used in transportation is fossil fuel. Recently, the researchers make great efforts to study new useful techniques to decrease the consumption of the fossil fuel and reduce the emission. In the transportation, the diesel and gasoline are widely used, which are still main fuel in a long time in the future. Except in the region of Europe, the diesel is usually used in the heavy duty. The gasoline is mainly used in the fleet vehicles, such as the passenger cars and motorcycles.

Figure 1.3 illustrates the energy consumption of transport in the next two decades which shows the energy consumption will increase over time. And the energy policy also changes over time. In the future, oil consumption will be supposed to be decreased because of the fossil fuel harmful gases emissions and conservation [5]. However, in a long period, the main fuel of the fleet vehicles will still be the gasoline.

A large percentage of the environment issues is the emission of the fossil fuel consumption, especially, causing the greenhouse gases emission increased significantly. Many methods applied to save energy, except using the new energies, another meaningful research orientation is the energy efficiency improvement. The technology improvement includes the optimization of the combustion methods [6] and the inhibition of the emission. For example the

CO_2 capture and storage technology improve the energy efficiency and substantially decrease the emission of harmful gases.

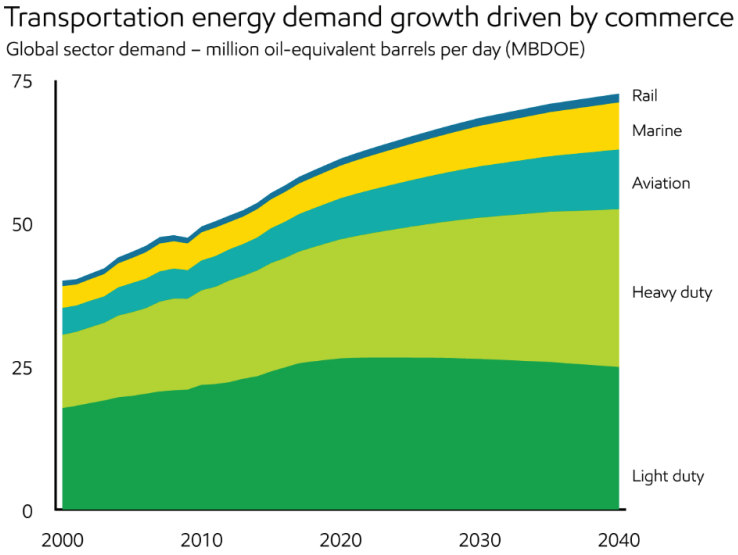

Figure 1.2 Transportation energy demand growth.

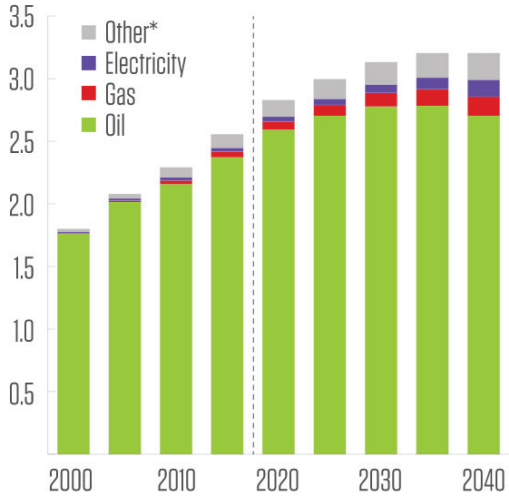

Figure 1.3 Transport energy consumption by fuel type (billion ton).

The environment issues are closely related with the consumption of energy. Not only the researchers concern the pollution and climate warming but also the most ordinary beings are cognizant of the environment damage now, like the heavy haze appearing in some regions. The climate warming is led by the greenhouse gases emissions. The CO2 is mainly produced by using

fossil fuel, which is a part of the greenhouse gases. Recently, the emission of global annual CO2 is 31 billion ton (Gt). As shown in Figure 1.4, based on the research by BP energy outlook (2016), in the evolving transition scenario, the carbon emissions by energy consumption increase by about 10 percent by 2040 with the tendency of the last two decades.

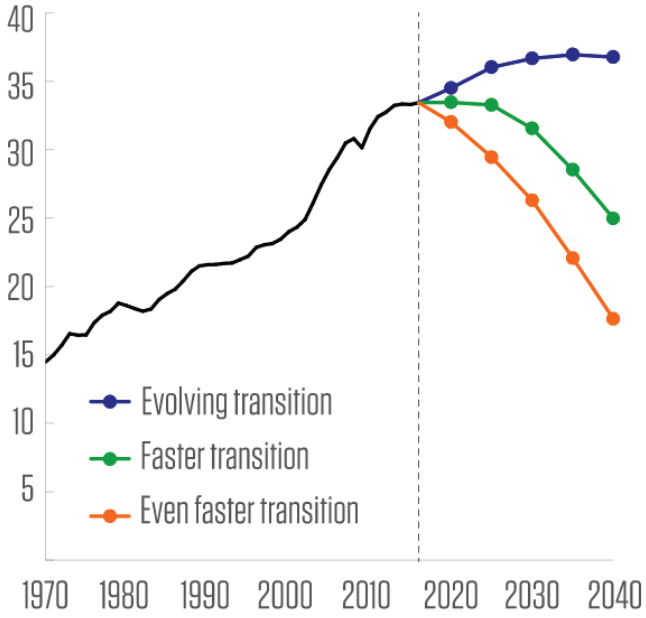

Figure 1.4 Carbon emissions (billion ton CO_2).

1.1.2 DISI engine

In internal combustion engines, the energy is released by burning the fuel inside the engine, which is the difference with the external combustion engines. The fuel-air mixture before combustion and the burned products after combustion are the actual working fluids. The energy are transferred from the working fluid to the mechanical components of the engine [7]. To overcome the atmospheric engine's shortcoming of low thermal efficiency and excessive weight, Otto proposed an engine cycle with four piston strokes, an intake stroke, a compression stroke, a power stroke, and an exhaust stroke. The thermal efficiency was increased to 14 percent. By 1890, almost 50,000 of these engines were sold in Europe and the United States. Further developments had been taken by several engineers (such as Karl Benz and James Robson), the two-stroke internal combustion engines was successfully developed. The exhaust and intake processes occur during the end of the power stroke and the beginning of the compression stroke. By 1892, a new form of internal combustion engine was outlined in the patent of the German engineer Rudolf Diesel. The ignition of fuel is heated solely by compression, which would double the efficiency of other internal

combustion engines. After five years efforts, a practical engine was developed by Diesel and the resources of M.A.N. in Ausburg combined. The appearing of rotary internal combustion engine has been considered as a major development in internal combustion engine field. The first rotary engine was successfully test in 1957, the engine was based on the designs of the German inventor Felix Wankel, and it took many years to develop the relative researches.

Atomization of fuel had impacted on engine development significantly. The earliest fuel used in engines were gas. Gasoline is the lighter fractions of crude oil, and was utilized in the late 1800s. To mix fuel with air in engines, the technologies, which were used to vaporize the gasoline, were developed after the availability of gasoline. After the quality of gasoline was markedly improved in the late 1930, the compression ratios steadily increased, which improved power and efficiency. The air pollutions and improvement in automotive consumption affected the engine design and operation. With the increasing internal combustion engine use, the large fossil fuel was consumed, and the huge harmful gases exhausted into atmosphere. The climate warming became a severe problem, the reducing of engine emission became a compulsory legislation, which was first introduced in California. In that case, the fuel economy and emission reduction became the goal of the researchers and manufacturers.

For early gasoline engines, the mixture formation was implemented with the help of a carburetor. The disadvantages of this method were the high engine-out emission and fuel consumption. Thereafter, the multi-port fuel injection (PFI) system was applied in the gasoline engines due to development of electrical controlling. There are some disadvantages in PFI engines. The fuel film on the port wall and the intake valves could be formed when the injection pressure is relative low, which could cause the bad effects during cold start. The acute interactions between the spray and the air flow in manifold will lead to an intense turbulence in cylinder. To prevent the in-cylinder knocking, the PFI compression ratio is limited to 10:1. Additionally, although the emissions can be controlled in an acceptable level, it contribute to the work of the three-way exhaust after-treatment system [8].

In order to overcome the limitations of the PFI engines, the two combustion technologies were developed, the direct injection (DI) stratified combustion spark ignition (SCSI) technique [9], and the homogenous charge compression ignition (HCCI) technique [10-11]. The lower fuel consumption and NO emission can come true in the DI SCSI engine comparing to the PFI engine [12]. Although the HC emissions increase, the NO emissions are greatly reduced by the HCCI

technique comparing to the PFI engine [13]. The disadvantages of the two technologies are their limited/load range, it means the engine should possess the two combustion modes simultaneously.

For a DISI engine, in the low load/speed operation, the mixed-mode DISI engine works with a stratified charge and lean mixture [14-15]. In the condition of higher load/speed, the engine runs with a homogeneous charge. The homogenous charge operation includes two parts, the medium load regions and higher load regions [16]. In the former, the charge is overall lean (or highly diluted stoichiometric). While, the charge is stoichiometric or even rich in the latter. Exhaust gas recirculation (EGR) is employed to control nitrogen oxides emissions in the high load. The optimal fuel economy determines the level of excess-air and EGR dilution use, and it maintains emission and combustion stability at acceptable regions.

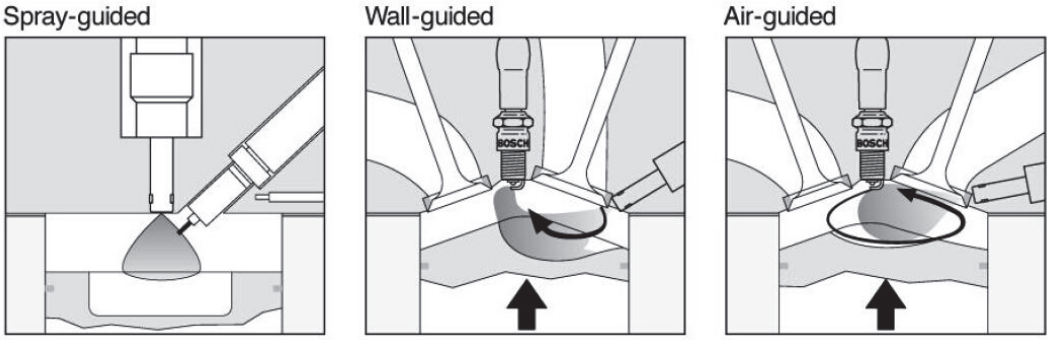

Figure 1.5 Classification of the GDI combustion systems.

Three broad categories of the combustion system exist in the direct injection spark ignition engines, air-guided, wall-guided, and spray-guided, as shown in Figure 1.5. In the spray-guided combustion system, the spark plug is close to the injector [17-19]. In the wall-guided and air-guided system, the spark plug is placed a long distance from the injector. In the wall-guided system, the spray is guided towards the spark plug by the air flow, which is caused by the interaction of spray and the piston combustion cavity. And in the air-guided system the spray is blown by the defined air motion in cylinder [20-21]. The wall-guided combustion system was widely used in the first generation of DISI engine. However, the spray guided combustion system may be employed in the second generation [22].

In addition, owing to the high injection pressure and downsized cylinder, the fuel spray might impinge on the piston cavity wall before being fully vaporized. Fuel spray impingement generally influences fuel atomization and combustion, and will lead to excessive hydrocarbon (HC) and soot emissions [23].

1.2 Objective and Approaches

In a real engine, the study of the effects of air flow on the fuel spray is exceptionally difficult because of the complicated and changeable air flow field [24]. Moreover, the theoretical and fundamental studies under a single condition are insufficient. Therefore, it is necessary to introduce a cross-flow to simulate the influence of swirling air flow on the fuel spray in the cylinder. The cross-flow is a particular air flow that is perpendicular to the direction of spray injection. The aim of this study is to examine the effect of cross-flow on the characteristics of the impingement spray, such as the spray structures, spray tip penetration, spray vortex height, droplet size and velocity distributions. The main objectives as follows:

(1) The effects of cross-flow velocity, ambient pressure and impingement distance on the spray structures in a vertical plane have been investigated using VCO and Sac hole nozzles. And then, spray tip penetration and vortex height were obtained from the impingement spray images for quantitative analysis.

(2) The influences of the ambient pressure and cross-flow velocity on the impingement spray structure in horizontal planes have been experimentally investigated.

(3) The droplet size and velocity distribution of local spray were measured in different locations under cross-flow conditions. Moreover, the relationship between droplet size and droplet velocity components has been analyzed.

(4) The droplets flow field distribution in the vertical plane were measured by PIV optical diagnostic method. The droplet velocity distribution in the wall-jet vortex was discussed in detail.

(5) The effects of cross-flow and ambient pressure on the near-field spray structure and droplet distribution were discussed. And the outlines of near-field spray in various cross-flow velocities were plotted by colored curves.

(6) The numerical simulations were conducted using the CONVERGE software. The simulation results showed the same tendency with the experimental results about of the cross-flow. The impingement spray images in a vertical plane and several horizontal planes were recorded by a high speed video camera and a laser sheet technology. By employing the particle image analysis (PIA) optical diagnostic method, the Sauter mean diameter (SMD) and the droplet velocity components were investigated. The Particle image velocimetry (PIV) was used to measure the droplet velocity distribution in the wall-jet vortex part.

1.3 Outlines

The organization of this dissertation is shown as following.

Firstly, the background of this research was systematically introduced from the energy and environment to the DISI engine. A review of the previous works of the spray mixture formation, spray optical diagnostics and cross-flow were introduced in Chapter 1.

Secondly, Chapters 2 introduces the experimental setups of this study. The experiments included high speed video photography, PIA measurement and PIV measurement.

Thirdly, in Chapters 3, the impingement spray structures in a vertical plane have been investigated by using high speed photography. The effects of cross-flow velocity, ambient pressure and impingement distance on spray tip penetration and vortex height were analyzed quantitatively.

The impingement spray movements in two horizontal planes were investigated in Chapter 4 using a laser-sheet imaging technique.

Under cross-flow conditions, the droplet size and velocity distribution of local spray were presented in Chapter 5. PIA optical diagnostic method was used to obtain the droplet images of local spray. In addition, PIV optical diagnostic method was utilized to measure droplet velocity distribution in the region of wall-jet vortex.

In Chapter 6, the near-field spray structure and droplet distribution were discussed using a long-distance microscopic and high speed video camera.

The numerical simulations of impingement spray was conducted by the CONVERGE software in Chapter 7. The simulation results were expressed and compared with the experiment results.

At last, characteristics of impingement spray in the cross-flow were summarized in Chapter 8. The future work was concluded in the end of this dissertation.

1.4 Literature Review

1.4.1 Spray mixture formation

The engine sprays are used for mixing the liquid fuel with air. In direct-injection engines, the fuel is injected into the combustion chamber to form a combustible mixture with air. The spray and the mixture formation affect the ignition behavior, heat release, pollutant formation and fuel economy. The high injection pressure of fuel will also impart turbulence which complicates the spray phenomena. The subsequent break-up processes of the droplets, which are obtained by the primary break-up, are called secondary break-up. The smaller droplets can be got by the aerodynamic force, which is caused by the relative velocity between droplets and ambient gas. The droplets are decelerated by the resistance of the ambient gas. The strong drag force effect on the spray tip droplets, which results in the droplets lose their momentum more quickly than the droplets near the nozzle. The droplets are continuously replaced by new droplets at the spray tip with the increasing of the penetration. The droplets which are pushed aside by the air motion develop the cone shape of the spray (see Figure 1.6).

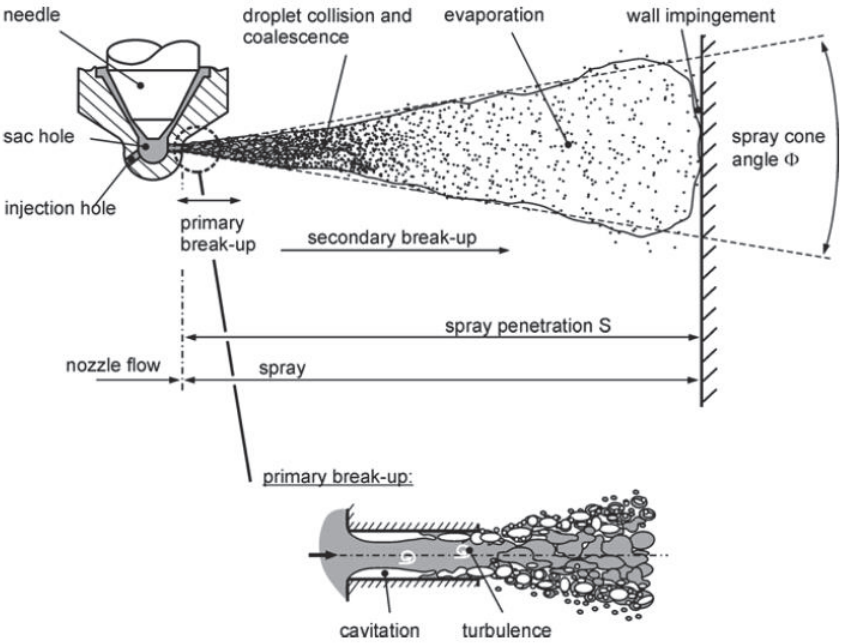

Figure 1.6 Spray break-up process from hole-injector.

The dense droplets are concentrated near the nozzle, and droplets are diluted downstream the nozzle by the entrainment air. Although some droplets and vapor exits in the outer spray regions, the most of the dense droplets are concentrated near the axis of spray. This droplet

distributions are caused by the interaction between the spray and entrained gas. In the dense droplet area, the collisions may happen. And this is the reason why the droplet size and velocity in that area are instable. The coalescence is induced by the collisions, and the broken up small droplets can combine into large droplets by the coalescence.

The boundary conditions, which include gas temperature, gas density, and gas flow in the in-cylinder, are influence the dilute spray downstream of the nozzle. The droplets are sensitive to those conditions in further spray disintegration and evaporation. The maximum penetration of the spray is the distance from the nozzle to the piston bowl. The impingement may occur on the wall, when the injection pressure is high, the injection duration is long, or the cylinder gas density is low. The liquid wall film forms after impingement. Because the wall film is hard to evaporate, and the mixture of air and fuel becomes bad, therefore the partially burning may happen. The final result is that the fuel economy decreases and the emissions increase.

Many fundamental experiments and semi-empirical relation about the behavior of the relevant spray parameters of sprays have been performed and published by many different researchers. The parameters of the spray were concentrated on spray cone angle, spray penetration, break-up length, and average droplet diameter with different boundary conditions. Because it is difficult to investigate the spray behaviors in the real engine, these experiments have usually been taken with quasi-stationary sprays, the main injection phase of full cone sprays can be referred by the results. In the following. The most detailed semi-empirical relations were investigated by Hiroyasu and Arai [25].

There are two phases in the penetration development of the spray over time. The first phases refers to the procedure form the beginning of injection (t = 0 ms ASOI, needle begins to open) to the moment when the liquid jet begins to disintegrate ($t = t_{break}$, Eq. 1.1), in which S linearly grows with time (Eq. 1.2). During the second stage ($t > t_{break}$), the spray tip consists of droplets, and the penetration S becomes a function of $t^{\frac{1}{2}}$, as shown in Eq. 1.3. The penetration should be continuous during the whole procedure, hence the coefficients in Eqs. 1.1~1.3 can be obtained because Eq. 1.2 is equivalent to Eq. 1.3 at the moment of breakup.

$$t_{break} = \frac{28.65\rho_l d}{(\rho_g \Delta p)^{\frac{1}{2}}} \tag{1.1}$$

$$t < t_{break}: \quad S = 0.39 \left(\frac{2\Delta p}{\rho_l}\right)^{\frac{1}{2}} t \tag{1.2}$$

$$t > t_{break}: \quad S = 2.95 \left(\frac{\Delta p}{\rho_g}\right)^{\frac{1}{4}} d^{\frac{1}{2}} t^{\frac{1}{2}}, \tag{1.3}$$

where, S is the vertical penetration, $\Delta P = P_{inj} - P_a$ is the pressure drop across the nozzle, ρ_g and ρ_l are the gas and liquid densities, d is the nozzle diameter and t is the time ASOI. The penetration increases with increasing injection pressure, while it will be reduced when the gas density increases. The fuel jet momentum is enhanced when the nozzle diameter increases, and the penetration enlarge due to the increased momentum. When the ambient temperatures exceeds 590 K, the effect of the gas temperature on spray penetration is hardly observed. Based on this, the further empirical equations are deduced by Dent [26] and Fujimoto et al. [27]. The effect of gas temperature T_g on the spray penetrations was added in the empirical equation, as shown in Eq. 1.4. That is important for the practical engine when the combustion temperature is high.

$$\mathrm{S} = 3.07 \left(\frac{\Delta p}{\rho_g}\right)^{0.25} \cdot (t \cdot d)^{0.5} \cdot \left(\frac{294}{T_g}\right)^{0.25}. \tag{1.4}$$

The spray cone angle is also an important parameter of a spray. Many researches experimental and empirically illuminated the relations with the conditions. For sac hole nozzles, the authors give the following relation for the stationary spray cone angle [25]:

$$\Phi = 83.5 \left(\frac{L}{d}\right)^{-0.22} \left(\frac{d}{d_s}\right)^{-0.22} \left(\frac{\rho_g}{\rho_l}\right)^{-0.22}. \tag{1.5}$$

where, Φ is the spray cone angle, d_s is the sac hole diameter, and L is the length of the nozzle hole. If the L/d ratios is small, the cavitation structure keep in the injection hole, and can enter the combustion chamber with fuel. The collapsing happens outside the nozzle, which enlarges the spray cone angle. A small value of d/d_s promotes the increasing of effective cross-sectional area at the entrance of the nozzle hole, enhances the static pressure at this point and restrains the inception of cavitation. The density ratio ρ_g/ρ_l plays an important role on the spray cone angle comparing with other parameters. The spray cone angle decreases when the ambient gas density increases. It indicates that the spray diffusions are restrained by the increased ambient gas density. Another relation of the spray cone angle was given by Heywood [28],

$$\tan\left(\frac{\Phi}{2}\right) = \frac{4\pi}{A}\left(\frac{\rho_g}{\rho_l}\right)^{0.5} f(\Upsilon) \tag{1.6}$$

where, A is a constant, which depends on the nozzle design and it may be obtained from experiments or approximately calculated as $A = 3.0 + 0.28(L/d)$. The $f(\Upsilon)$ is a weak function about the physical properties of the liquid and the injection velocity [29], as shown in Eq. 1.7. If the injection pressure is very high, the Υ increases, than the $f(\Upsilon)$ tends to $\sqrt{3}/6$ [30].

$$f(\Upsilon) = \frac{\sqrt{3}}{6}(1 - \exp(-10\Upsilon)), \Upsilon = \left(\frac{Re_l}{We_l}\right)^2 \frac{\rho_l}{\rho_g}. \tag{1.7}$$

The Sauter mean diameter (SMD) is usually used in quantity characterizing the average droplet in a spray, it can describe the extent of the spray break-up. The SMD is the diameter of a model droplet, the diameter is defined as the volume-to-surface-area ratio, which is equal to the ratio of the sum of all droplet volumes (V_{drop}) in the spray to the sum of all droplet surface areas (A_{drop}):

$$\left(\frac{V_{drop}}{A_{drop}}\right)_m = \frac{\left(\frac{\pi}{6}\right)SMD^3}{\pi SMD^2} = \frac{SMD}{6}, \tag{1.8}$$

$$\left(\frac{V_{drop}}{A_{drop}}\right)_{spray} = \left(\sum_{i=1}^{n} d_i^3\right)/\left(6\sum_{i=1}^{n} d_i^2\right). \tag{1.9}$$

$$\text{SMD} = \frac{\sum_{i=1}^{n} d_i^3}{\sum_{i=1}^{n} d_i^2}. \tag{1.10}$$

When the SMD is small, it means the surface per unit volume is large. The enlarged surface provides more effective evaporation and mixture formation. It is well-known that the SMD is quantity in characterizing the spray formation process, however it can be used to describe the droplet size distribution of the spray. It is possible that two sprays with same SMD value can own quite different droplet size distributions. The empirical relation of the SMD based on experimental result was given by Hiroyasu et al [31-32]:

$$\frac{SMD}{d} = 0.38Re^{0.25}We_l^{-0.32}\left(\frac{\mu_l}{\mu_g}\right)^{0.37}\left(\frac{\rho_1}{\rho_g}\right)^{-0.47}, \tag{1.11}$$

where, μ is the dynamic viscosity. The Sauter mean diameter (SMD) increases with the gas density increasing, because the coalescence of droplets intensifies with increased initial droplet diameter, which is caused by the enlarged nozzle hole diameter. The higher injection pressure enhances the

atomization, and thus decreases the value of SMD. It is important to remember that the measurement of droplet sizes should be taken place in the lean spray area or at the long distance form the nozzle. The results of a complete spray always include a high uncertainty, however, it is meaningful to estimate the spray in a qualitative way.

To understand the detail of the spray break-up process, the fuel is an intact liquid core or large ligaments and droplets should be made sure. Because this two kinds breaking ways are different. The fuel may form an intact liquid core than divide into the separation of droplets downstream the nozzle, or the fuel already forms large ligaments after leaving the nozzle. Some researchers investigated this using electrical conductivity measurements [33-34], which was used to explore the inner structure of the spray. The electrical resistance between the nozzle and a fine wire detector, which located in the spray jet, was measured. The core lengths results measured by different researchers presented different value, but it is agreed by most researchers that the core length is dependent on the ratio of liquid and gas density, and that is proportional to the nozzle diameter *d*, as the Eq. 1.12 shows.

$$L_C = C \cdot d \cdot \sqrt{\frac{\rho_l}{\rho_g}} \tag{1.12}$$

where, C is a the empirical constant, which are obtained experimentally, and it usually in the range of 3.3~11. The radial extent of the core region increases along the spray axis from the nozzle, and in the core region the construction is not pure liquid [35]. It is considered by the researchers this region consists of a very dense cluster of ligaments and droplets. With the laser optical technology use in the experiments [36-37], the inner spray structure have been observed, the results showed the break-up zone includes high liquid content areas, which are separated from each other. By the help of the real size transparent nozzle introducing, the whole process have been cleared. In the high pressure injector, the spray begins already inside the nozzle holes, because the turbulence and cavitation disintegrate the spray before leaving the nozzle [38]. Another more detailed relation is presented by Hiroyasu and Arai [25].

$$L_b = 7 \cdot d \left(1 + 0.4\frac{r}{d}\right) \cdot \left(\frac{p_g}{\rho_l u^2}\right)^{0.05} \cdot \left(\frac{L}{d}\right)^{0.13} \left(\frac{\rho_l}{\rho_g}\right)^{0.5}. \tag{1.13}$$

where, u is the initial velocity of spray, and r is the radius of the inlet edge of the hole. The effect of the inlet edge rounding is added to the relation in Eq. 1.13. The L_b increases with a rounded

inlet edge, which weakens the cavitation in the nozzle hole. $p_g/\rho_l u^2$ is the expression of the influence of cavitation and turbulence.

Primary break-up is the first disintegration of the coherent liquid into ligaments and large droplets. The break-up mechanisms are summarized in Fig. 1.13. The aerodynamic shear forces at the interface of gas and liquid are formed by the high relative velocities, this shear forces result in the disintegration of droplets. The strong turbulence which is form inside the nozzle and entrained in the liquid increases the primary break-up. The instable growth of waves influences the break-up only in the edge of the spray, the main reasons, which are proven, are the effects of turbulence and cavitation formed in the nozzle hole.

The turbulence induced disintegration is considered as one of possible break-up mechanism in the primary break-up. When the strong radial turbulence happens inside the nozzle, the turbulent eddies can form in the liquid, the thus the liquid can be collapsed by the strong eddies Wu et al. [39]. Turbulence induced primary break-up is regarded as one of the most important break-up mechanisms of high-pressure sprays.

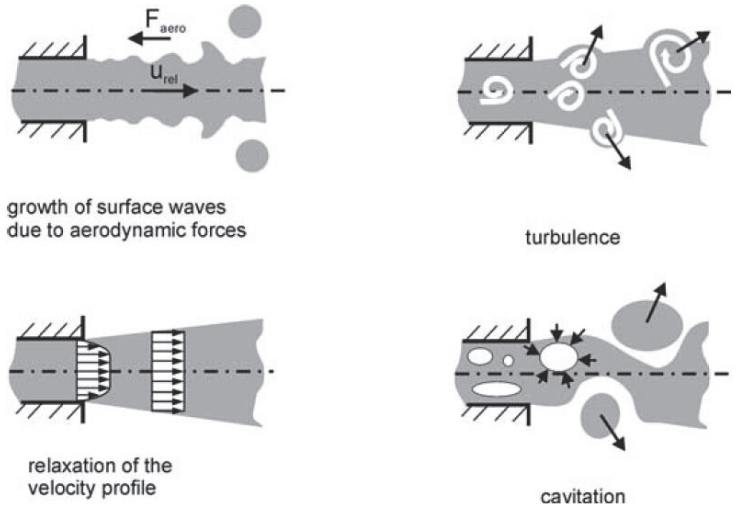

Figure 1.7 Mechanisms of primary break-up.

The relaxation of the velocity profile is considered as a potential primary break-up mechanism. Assuming *L/d* ratios are large and the liquid with cavitation in the nozzle hole, the velocity profile may change at the moment the liquid leaving the nozzle. Because the wall boundary condition disappears, an acceleration of the liquid edge region accelerated by the viscous forces, and the velocity profile turns into a uniform profile, as shown in Figure 1.7. This process

may lead to the break-up in the outer edge region. However, the assumption in the case of high-pressure injection is almost invalid, because the cavitation occurs, and *L/d* ratios are small.

The cavitation-induced disintegration is another important mechanism for primary break-up. In the high pressure nozzle, the cavitation structures form inside the nozzle holes. The strong acceleration of the liquid by the difference of the injection pressure and ambient pressure is one of the factors of the cavitation formation. The other factor is the strong curvature of the streamlines at the inlet edge. Therefore, the liquid and gaseous phase exist inside the nozzle holes simultaneously. The pressure difference (between injection pressure and ambient pressure) and the nozzle geometry decide the intensity and structure of the cavitation zones. The pressure difference between the bubbles and ambient pressure makes the cavitation bubbles imploding. It is very difficult to clarify the main reason, which caused the primary break-up, between the turbulence affect and the cavitation bubble collapses. Sometimes, the turbulence can transfer to cavitation [40-42]. Hence, the two main primary break-up mechanisms are turbulence induced disintegration and cavitation induced disintegration, and the two mechanisms exist simultaneously in the high pressure spray.

The secondary break-up is mainly caused by aerodynamic forces, which consist of friction and pressure. The aerodynamic forces forms by the relative velocity between droplet and ambient gas. An instable growth waves are induced by the aerodynamic forces, this waves distribute on the interface of gas-liquid or the whole spray. Therefore, the droplets disintegrate by the strong waves. And this disintegration happens again and again, which results in the droplets break into smaller droplets. There are many break-up mechanisms for this disintegration, vibrational break-up, bag break-up, bag/streamer break-up, stripping break-up, and catastrophic break-up. Usually, all the break-up mechanisms can happen in the pressure spray.

1.4.2 Spray/jet in cross-flow

In engines, in order to reduce emission and fuel consumption, the air flow is used as an important method to ensure the mixture in different modes. The air flow is controlled by the design of the inlet ports, the cylinder head, and piston crown geometry primarily. Figure 1.8 shows the simultaneous fuel concentration and flow field measurements for a single motored-spray cycle at crank-angle resolution in the SG-SIDI engine under stratified fuel operation using PIV technology [43]. Images reveal the highly turbulent conditions that exist during the injection even and shortly

afterwards as well as the short time interval after the injection event in which an ignitable mixture is located near the spark plug (32º – 30º BTDC). The gray color-scale for equivalence ratio is incorporated with a color-scale (blue and green) to highlight the regions of lean mixtures within the flammability limits (Φ = 0.6 – 0.9, shown in blue) and regions of stoichiometric mixtures (Φ = 0.9 – 1.1, shown in green).

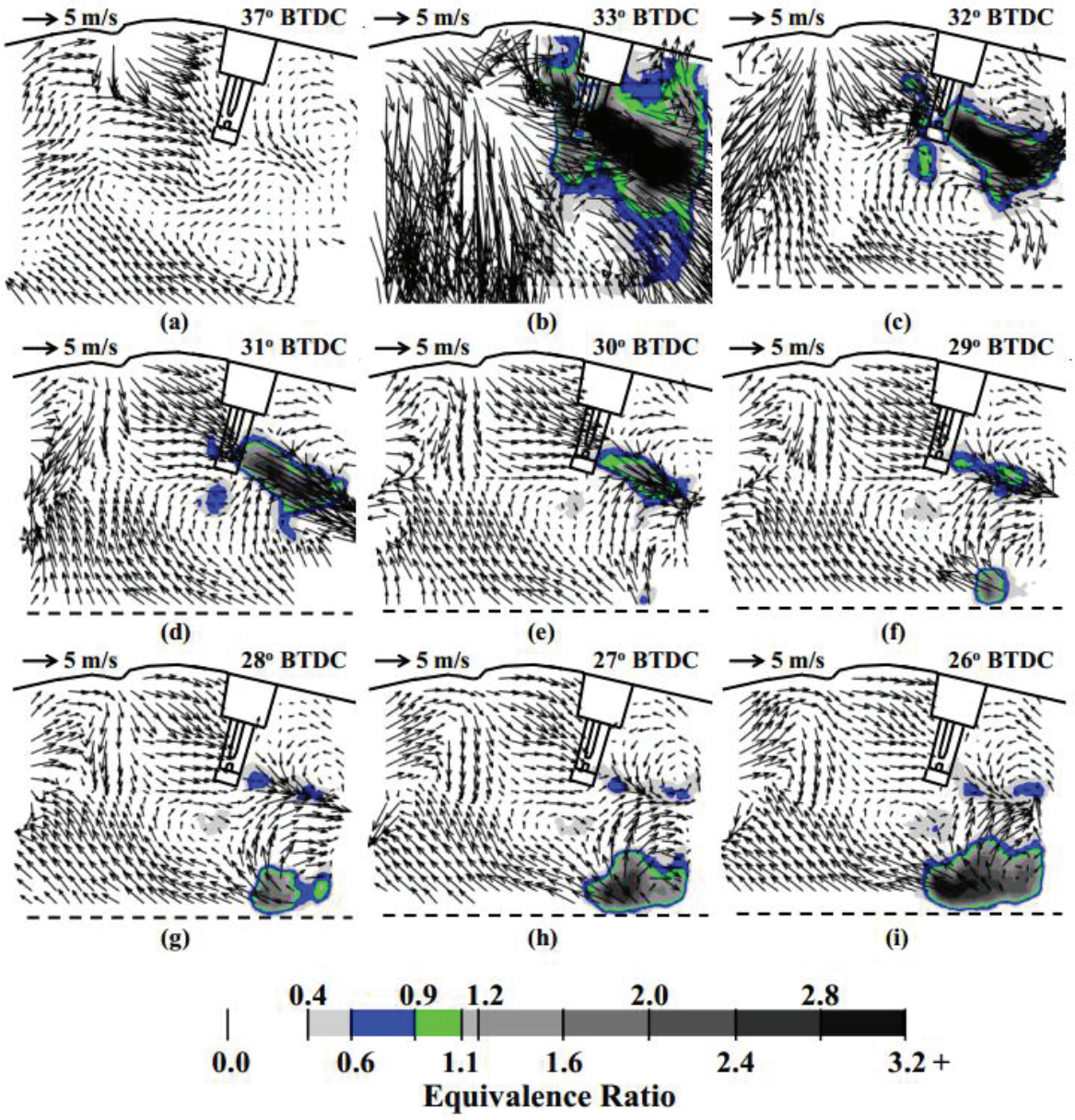

Figure 1.8 Simultaneous fuel concentration and flow field measurements for a single motored-spray cycle illustrate the conditions that exist near the spark plug during the typical spark timing.

The highly turbulent flow conditions that exist from the spray event. It is shown that the spray plume impacts the spark plug and primarily penetrates through the spark gap, creating high velocities downstream the spark plug. Strong velocities exist after the injection event and decrease in magnitude as time elapses from the end-of-injection. In a similar manner, rich fuel-air mixtures exist near the spark plug after the end-of-injection and quickly lean out with time. Specifically, a rich fuel cloud exists downstream the spark plug at 31° BTDC and leans out near stoichiometric of 0.9 a crank-angle later (30° BTDC). Beyond this timing, the fuel distribution directly downstream the spark plug is fuel-lean and becomes leaner quickly with time.

Velocities surrounding the fuel-air mixture adequately describe the motion of the fuel-air mixture downstream the spark plug and within the piston bowl. Well after the injection event it is also shown that the flow field portrays a similar less turbulent 2-D flow pattern as shown prior to the injection event.

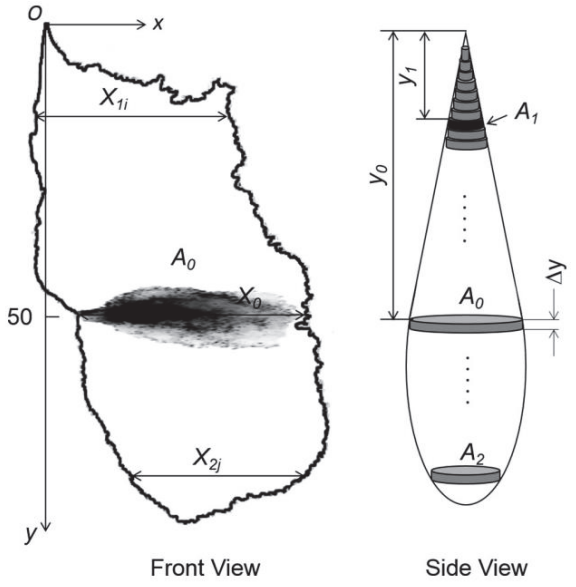

Figure 1.9 Definition of spray volume.

Recent studies on the spray characteristics in a cross-flow field focused on the interactions between the free spray/jet and cross-flow. Moon et al. [44] used a slit injector to study the effect of a cross-flow on free spray profiles. It was noted that the variations caused by a cross-flow were different at various parts of the spray. A significant variation was present at the bottom part of the spray, while a slight variation was found near the nozzle exit. Guo et al. [45] measured the spray area and spray volume of a free spray and evaluated the effect of the air-fuel momentum flux ratio on the spray profiles, as shown in Figure 1.9. They reported that the spray volume showed

an approximately linear increasing trend with the development of the free spray under a constant cross-flow velocity.

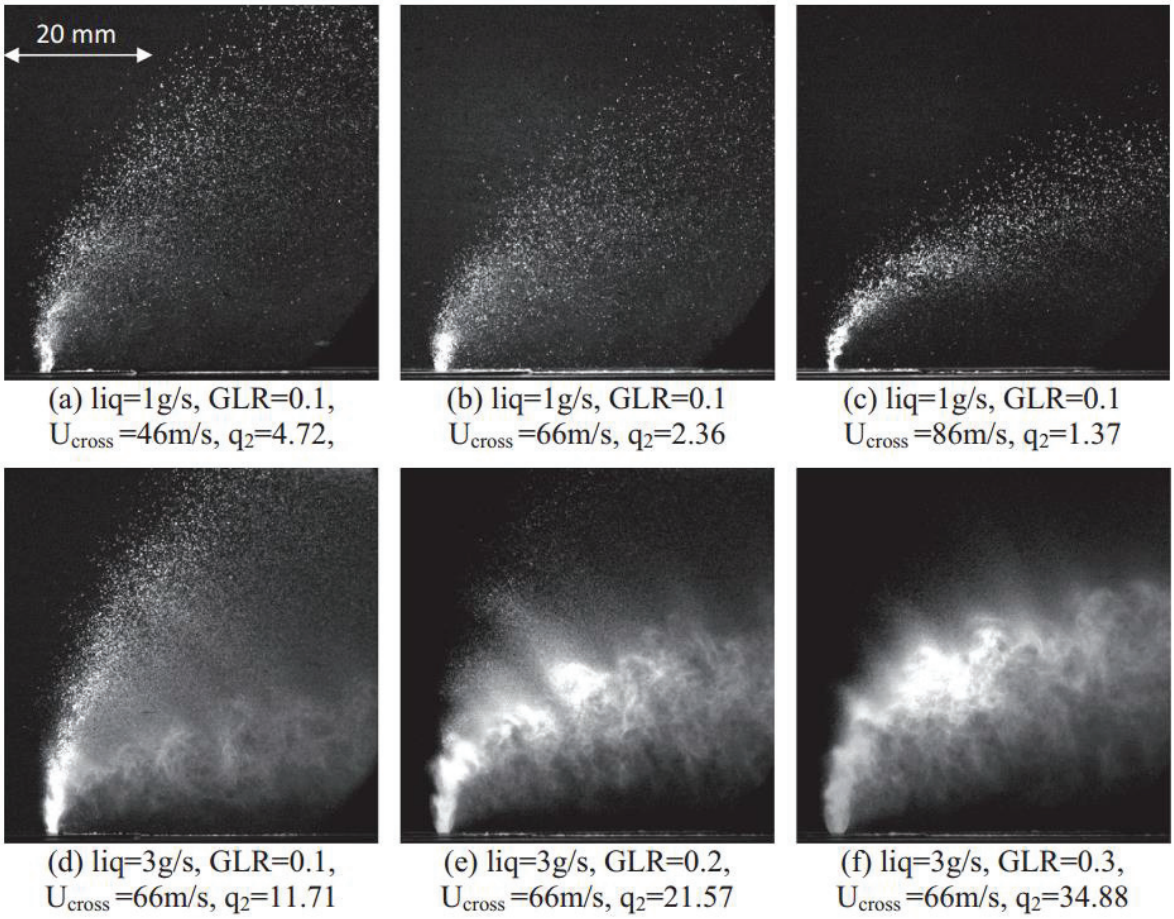

Figure 1.10 Instantaneous images of spray in cross flow for water.

The breakup of free spray injected into a cross-flow field was reported by some researchers [46–48]. Their works clarified that the cross-flow could promote secondary breakup and have a marked impact on the transport of secondary droplets. Based on a spray structure observation, Getsinger et al. [49] investigated the stability characteristics of jets in a cross-flow. They indicated that a counter-rotating vortex pair appeared behind a jet column under the cross-flow condition. Sinha et al. [50] performed experimental studies utilizing a laser shadowgraph and particle tracking velocimetry to derive the spray trajectory and droplet velocities. They proposed a novel correlation for the spray trajectory combining the momentum ratio with the liquid surface tension. They found that at similar air-blast spray conditions, but different cross-flow air velocities. The change in velocity causes a change in momentum ratio. Then the penetration decreases with

decrease in momentum ratio, as show in Figure 1.10. In addition, at the same liquid flow rate but varying GLR. The crossflow air velocity is also maintained the same. Hence, the change in spray structure and dispersion is the effect of GLR.

An experimental investigation of the bag breakup of round non-turbulent liquid jets in gaseous crossflow at room temperature and pressure is described by Ng et al. [51]. A remarkable feature of liquid jet breakup in cross-flow is the surface waves appearing along the downwind surface of the liquid column. The downwind surface waves are shown in Figure 1.11. These downwind surface waves were observed on the surface of the liquid jet for the following range of test conditions: cross-flow Weber number between 10 and 30 and momentum flux ratio between 220 and 1200.

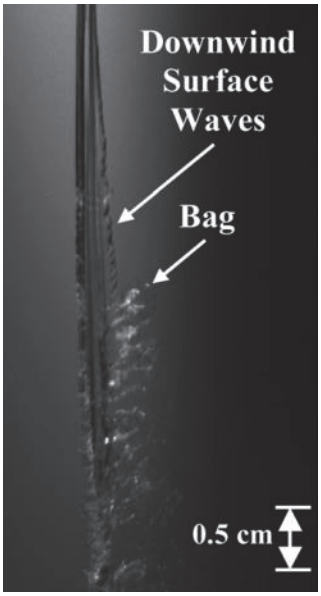

Figure 1.11 Downwind surface waves of round non-turbulent liquid jets in uniform gaseous crossflow within the bag breakup regime.

The above studies have provided an insightful comprehension of the effect of cross-flow on free spray, but did not consider impingement. Fuel spray impingement generally influences fuel atomization and combustion, and will lead to excessive hydrocarbon (HC) and soot emissions. Therefore, the study of the effect of cross-flow on impinging spray is more relevant than that of free spray for a DISI gasoline engine.

1.4.3 Spray/wall interaction

Owing to the high injection pressure and downsized cylinder, the fuel spray might impinge on the piston cavity wall before being fully vaporized. The spray/wall interaction has been paid wide attention from the automobile engineers. The outcome of droplet impingement is described by regimes, whose onset depends on the relative magnitude of the several forces acting upon the surface of the droplet, on the microscopic and macroscopic geometry of the target surface, and on the thermodynamic properties of the droplet–surface–surroundings system. Among the possible mechanisms of droplet–wall interaction, the following are considered by Bai et al. (2002) as illustrated in Figure 1.12:

- Stick: the droplet sticks to the wall in a nearly spherical form;
- Rebound: the droplet bounces off the surface after impact;
- Spread: the droplet adheres to the surface and forms a liquid film on the wall, which spreads out periodically until all the energy is dissipated;
- Splash: as the liquid film spreads out, a crown is formed owing to the kinematic discontinuity [52] and lateral cusps emerge, which become unstable and eventually break up into smaller fragments.

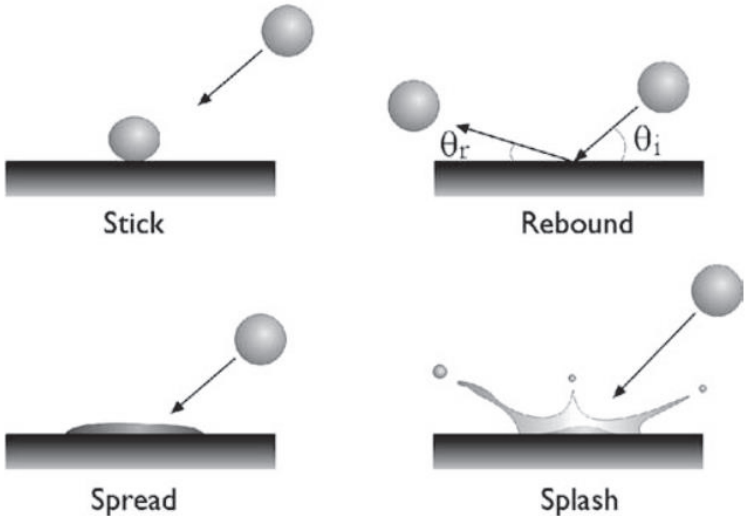

Figure 1.12 Outcome of single drop impacting on a solid surface.

Panão et al. [53–54] reported the application of the Mie-scattering method and shadowgraph technique to provide a macroscopic observation of an impingement spray in a cross-flow. They observed that the main spray structure shifted downstream with increasing cross-flow

velocity. Based on the results, two stagnation points were also identified in the impingement region and upstream respectively, as shown in Figure 1.13. Arcoumains et al. [55] have investigated the influence of a preexisting liquid film on an impingement spray under cross-flow velocities of 5 and 15 m/s and atmosphere pressure. They found that the wall film became thicker in a cross-flow that decreases the diameter of the droplets generated from secondary breakup. In these studies, the interaction between the wall-jet vortex structure and the post-impinged droplets was also discussed.

However, these studies are still not sufficient to explore the effects of cross-flow on the impingement spray characteristics, especially for the spray structures in different dimensions and rolled-up vortex motion.

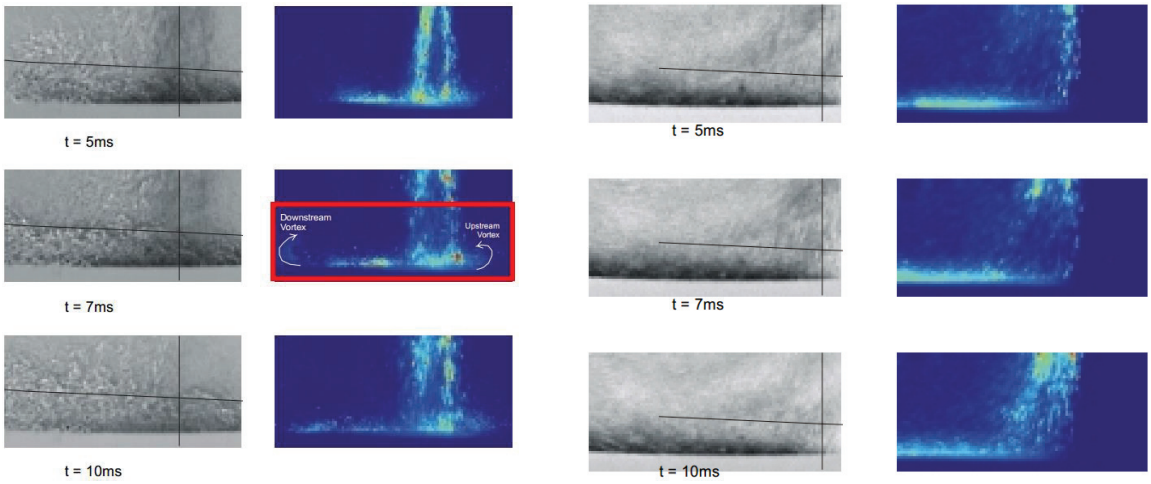

(a) $U_x = 5.3$ m/s (b) $U_x = 17.3$ m/s

Figure 1.13 Mie Scattering and Shadowgraph results with cross-flow.

About the droplet size measurement of impingement spray, Moriyoshi et al. [56] used the interferometric laser imaging droplet sizing (ILIDS) measurement to study the impinging spray development process in a cross-flow. Their results indicated that the relative mean velocity between cross-flow and droplet had a marked impact on the spray atomization, and small droplets were guided downstream by the cross-flow. Panão and Moreira [57] measured the droplet sizes and two velocity components of an impinging spray using a phase-Doppler anemometer (PDA) system. They analyzed the contribution of cross-flow to the interaction mechanism of individual droplets with the wall surface. These works clarified that the number of droplets in the stick regime decreased under the cross-flow condition. Arcoumains and Cutter [58] used a phase-Doppler anemometer (PDA) system to investigate the effect of cross-flow on the droplet size and velocity characteristics of an impingement spray. These works clarified that the overall mean droplet size

and velocities became larger under cross-flow conditions owing to the smaller droplets entrained by the cross-flow. The formation of a droplet cloud was also observed in the downstream of the spray.

Moreover, some authors used simulation results analysis the impingement spray characteristics. Andreassi et al. [59] implemented a model in a modified version of the KIVA 3V code. They compared experimental and numerical spray vortex shapes at 8 and 18 ms after SOI for the L = 3 cm case, as shown in Figure 1.14. There is a quite good agreement between the computed concentration field and the experimental PIV image. They pointing out that, besides being less accurate, the usage of logarithmic law of the wall does not allow to capture many phenomena like the boundary layer detachment, whichever the grid refinement, as it simply forces a wall parallel velocity on the first grid node.

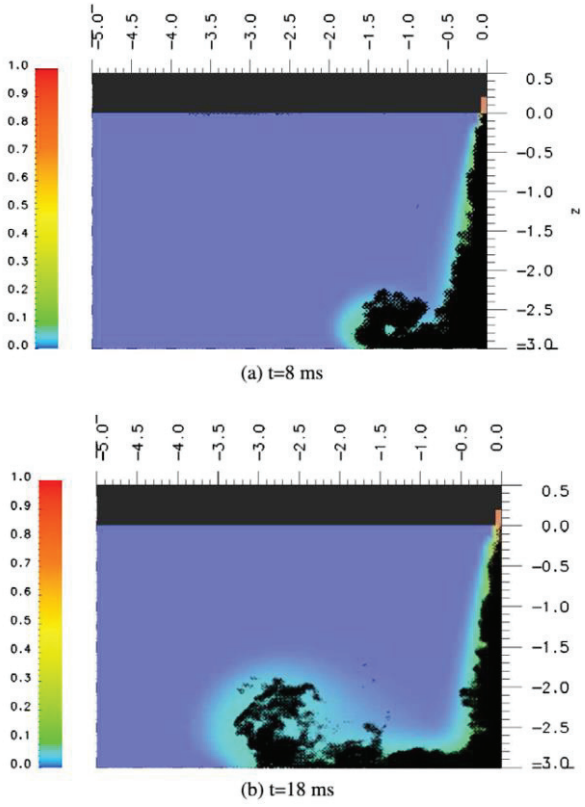

Figure 1.14 Comparison of experimental and numerical spray vortex shapes.

1.4.4 Optical diagnostic techniques

Spray usually injected from a nozzle with a very high velocity, and the fuels are transparent in general, hence, the direct observation and analysis of spray have some difficulties.

To observe the impingement spray structure and evolution of spray, the high speed video photography is widely applied in the experiments. Some droplet size and velocity measuring methods, such as Phase Doppler Anemometry (PDA) and particle image velocimetry (PIV), were applied to detect the droplet diameter and velocity in spray.

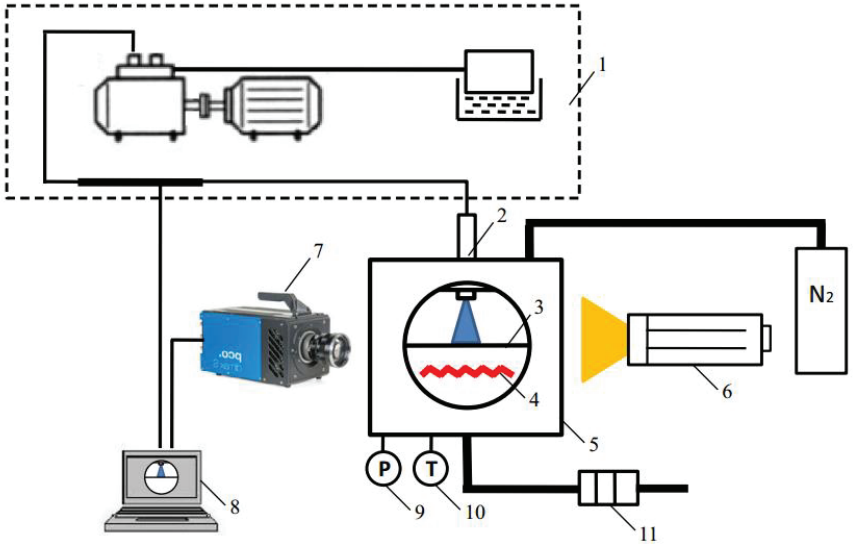

Figure 1.15 Visualization system for spray-wall impingement (1-common-rail system, 2-nozzle, 3-impinged wall, 4-heating system, 5-volume constant vessel, 6-light source, 7-ICCD camera, 8-data acquisition system, 9-pressure sensor, 10-temperature sensor, and 11-vacuum pump).

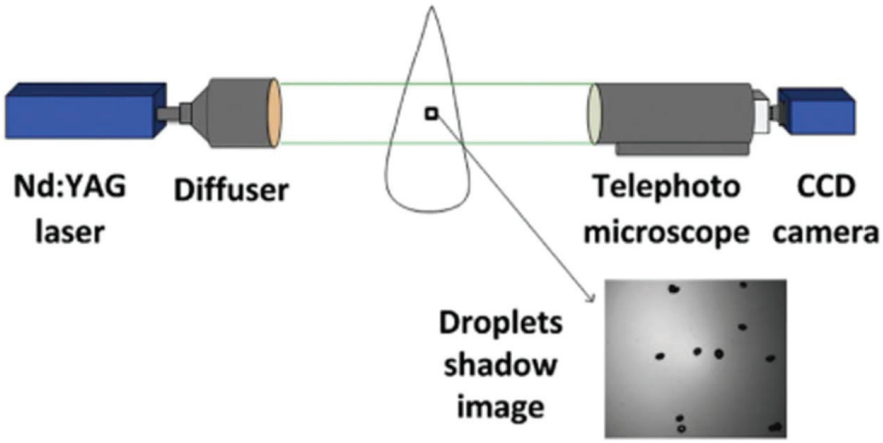

Figure 1.16 Schematic diagram of spray microscopic characteristic measurement system.

High speed photography experiment was carried out by Yu et al. [60]. A high speed video camera and a xenon lamp were used in this study with a shutter speed of 1/10,000 s and a resolution of 1024 × 1024 pixels. The visualization system was shown in Figure 1.15.They analyzed the

spray–wall impingement characteristics of n-butanol/diesel blended fuels under various environmental conditions. The parameters spray tip penetration R_w and spray vortex height H_w were used to evaluate the impingement characteristics.

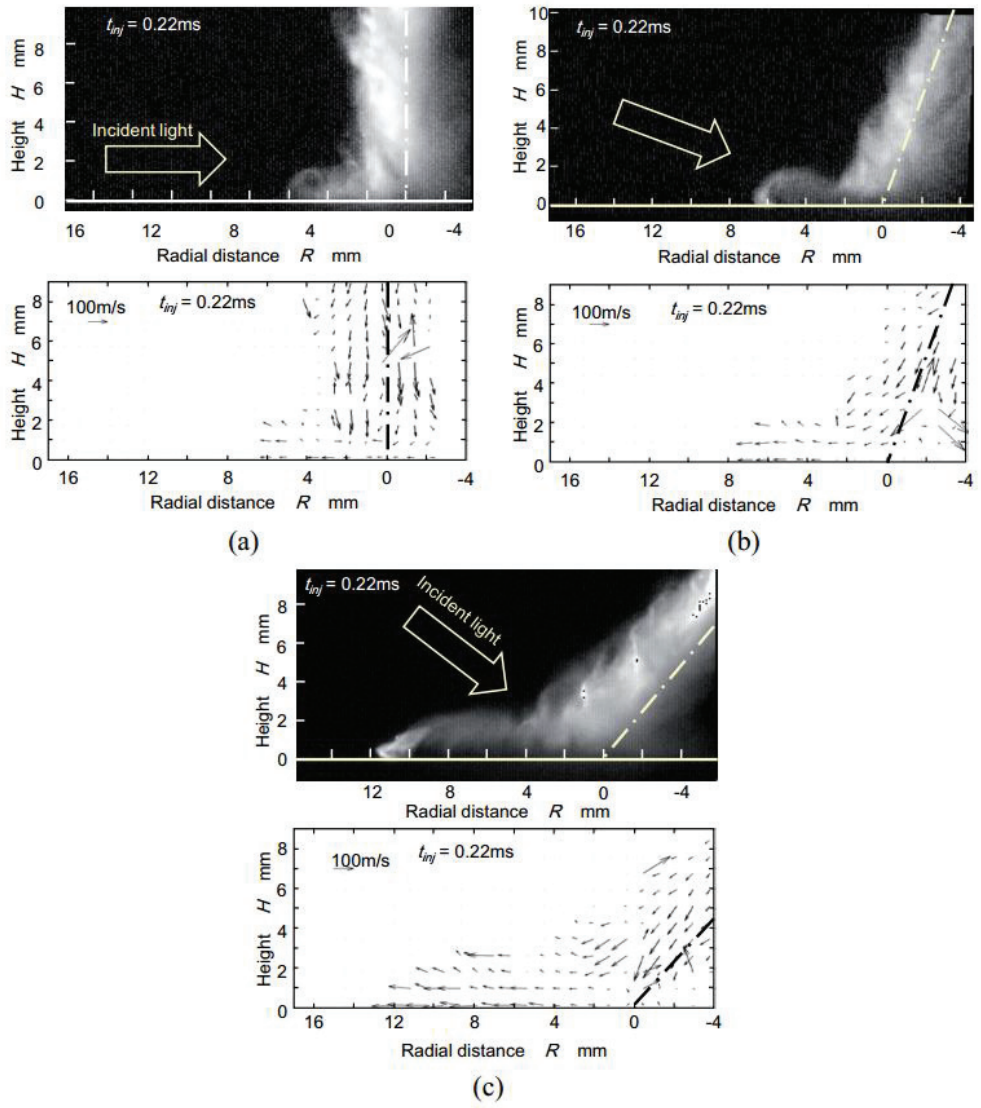

Figure 1.17 Tomographic images of post-impingement spray for various impingement angles and its velocity fields; (a) θ_d = 0 deg; (b) θ_d = 20 deg, and; (c) θ_d = 40 deg.

By means of particle droplet image analysis (PDIA) optical diagnostic method, Zhan et al. [61] investigated the spray microscopic parameters such as Sauter Mean Diameter (SMD), droplet diameter distribution probability curve, cumulative volume curve and characteristic diameter. The sketch of the particle droplet image analysis (PDIA) system for the local spray

microscopic characteristics detection was shown in Figure 1.16. A single pulsed Nd: YAG laser with the wavelength of 532 nm is used as the light source. A diffusor is attached to the laser for the homogeneous illumination. A CCD camera (ImagerProSX 5 M), attached with a long focus microscope (Queststar QM1) is used to capture the local droplet distribution in spray. The precise displacement control (1 μm) of the electric positioner ensures the accurate determination of the scanning target position.

Zama et al. [62] measured the velocity field of an impingement diesel spray with time-resolved particle image velocimetry (PIV). To obtain a two-dimensional tomographic image, diesel spray was impinged to a slender bar instead of a flat wall in their study. As a result, velocity distribution of the impingement diesel spray in time series was obtained for various impingement angles. They used PIV system to study the effect of inclination angle on the velocity field of post-impingement diesel spray. Figure 1.17 shows tomographic images and vector maps for 0, 20, and 40 deg of inclination angle. The spray tip location of 20 deg impingement was slightly shifted downward to a position greater than 0 deg. Furthermore, the spray tip at 40 deg obviously developed more than those of the previous two images. The rolling-up motion at the tip showed unique features corresponding to the inclination angle of impingement.

As for the near-field spray, the previous work only concentrates on the study in quiescent atmosphere. The breakup process was explained by Bae and Kang [63] using a long-distance microscope. They observed that the ligaments were produced by the disturbed spray surface and small droplets were generated at the end of the ligaments. Tang et al. [64] used an optical long-distance microscope to investigate the spray primary breakup. And they found that the high injection pressure promoted the spray primary breakup while the high ambient pressure restrained it. In addition, the initial spray of diesel is easier to breakup into ligaments and droplets because of smaller surface tension and viscosity compared to that of biodiesel under atmospheric condition, as shown in Figure 1.18. However, the near-field spray behaviors in a cross-flow were not completely clarified in the previous works owing to the lack of near-field spray information under cross-flow conditions.

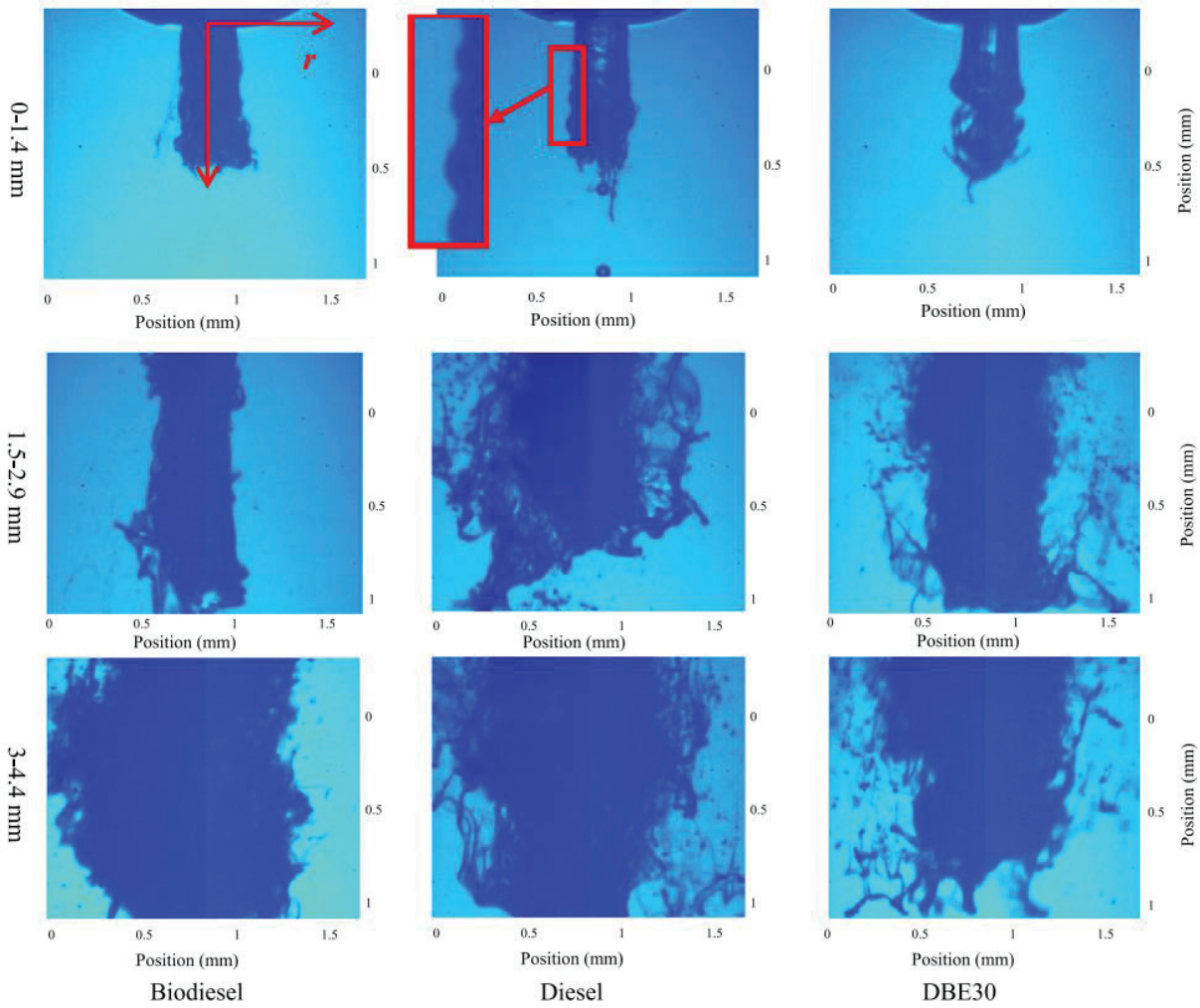

Figure 1.18 Comparisons of the near nozzle spray evolutions for different fuels at P_{inj} = 800 bar, P_{amb} = 1 bar.

1.5 Summary

In this chapter, the background and motivation of this research was represented from the energy consumption, carbon emissions and performance of DISI engine. The investigation of characterization of impingement fuel spray in cross-flow ambient is benefit for the fundamental researches of the DISI engine. By descripting the spray-wall interaction and cross-flow in DISI engine, it can be seen that the air flow and wall impingement in a direct-injection spark-ignition (DISI) gasoline engine affect the fuel-air mixture formation and the quality of fuel combustion. A review of the previous works of the spray mixture formation, spray optical diagnostics and cross-flow also were introduced here.

By analyzing the optical diagnostic techniques, for the impingement spray structure observation, a high speed video camera and laser sheet will be used in this study. PIA system will be used to measure the droplet size and velocity distribution of local spray. The droplet velocity distribution in wall-jet vortex will be measured by PIV system. A high speed video camera connected with a long-distance microscope was employed to obtain the near-field spray images.

Chapter 2 Experimental Apparatus and Procedures

2.1 High-Pressure Wind Tunnel

The circuit wind tunnel was used to provide the air flow under high pressure by Tajima et al. [65]. However, the complex structure and cost are the significant problems for air flow experiments. In this part, another method is introduced to obtain the air flow under high pressure ambient using pressure tank. The principle schematic is shown in Figure 2.1. Compressed air is stored in the pressure tank, the valve 2 keeps partly opening, when the valve 1 is opened, the pressure in observation chamber can increase rapidly, and the velocity in observation chamber can also be obtained. Because the throttling of valve 2 and the supplement from pressure tank, the pressure in observation chamber will not change to atmosphere rapidly. In that case, the velocity and pressure conditions can be kept in observation chamber, the matching of them can be control by valves. When the velocity and pressure meet the experimental conditions, the measurement can be triggered by a quick-response control system.

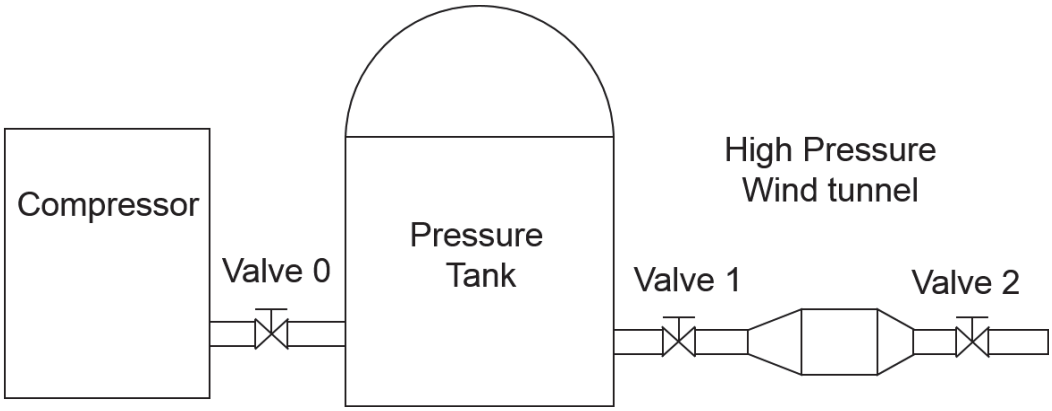

Figure 2.1 Schematic of cross-flow wind tunnel system.

Figure 2.2 is a schematic of the high pressure wind tunnel that was applied to provide a uniform cross-flow field. It consists of the diffusion section, the rectification section, the contraction section, the observation chamber and two control valves. Guide vanes are used in the diffusion section to diffuse the air flow, and mesh screens are utilized in the rectification section for uniform air flow, as shown in Figure 2.3. The uniform cross-flow is acquired in the observation

chamber located downstream of the contraction section. The cross-flows with various velocities and pressures are obtained by adjusting the open areas of valve 1 and valve 2.

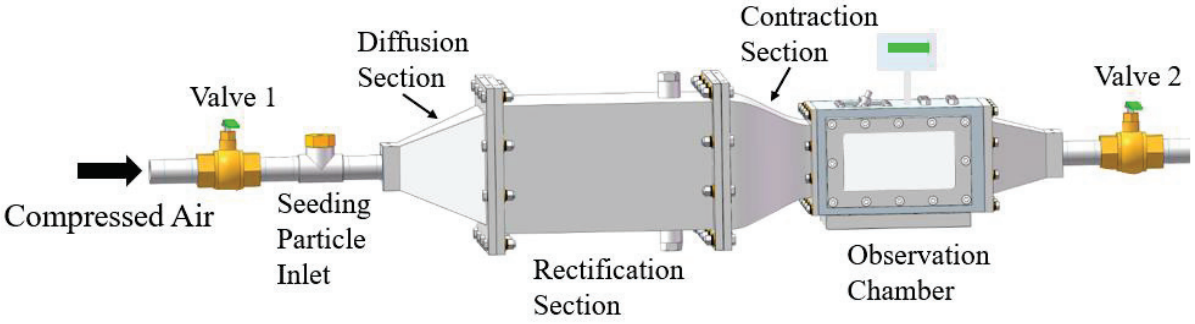

Figure 2.2 Schematic of high pressure wind tunnel.

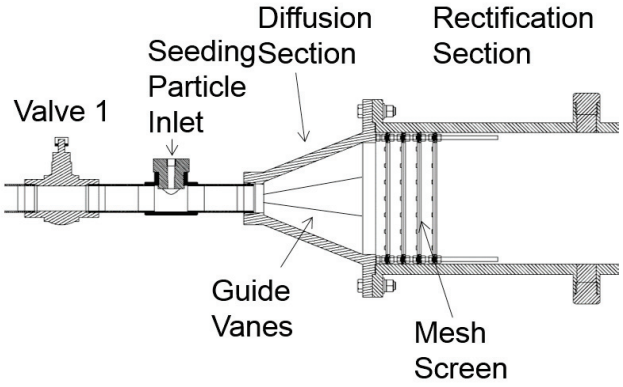

Figure 2.3 Details of diffusion section and rectification section.

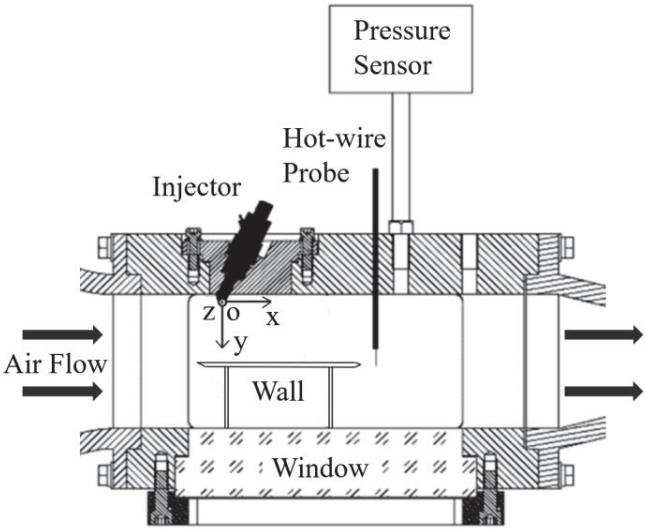

Figure 2.4 Details of observation chamber and coordinate system definition.

The window size of the observation chamber is 200 mm in length with a 100 × 100 mm^2 inner section, as shown in Figure 2.4. The window is composed of Pyrex. A valve covered orifice (VCO) type nozzle was fixed on the upper surface of the chamber with a 25° spray angle to maintain the spray direction perpendicular to the direction of the cross-flow. The hole diameter of the single-hole VCO nozzle is 0.15 mm. A hot wire anemometer possessing a short response time was assembled to monitor the cross-flow velocity, and a high sensitivity pressure transducer was employed to measure the ambient pressure in the chamber. The impingement wall was composed of transparent acrylic with 140 × 90 mm^2 size placed below the injector, and the impingement distance could be adjusted from 25 mm to 75 mm. The nozzle tip position was defined as the origin O of this coordinate system. The direction of cross-flow is along the positive x-axis, whereas the injection direction is along the positive y-axis.

The uniformity of the cross-flow velocity distribution in the observation chamber was examined using PIV technology. The test section was in the xoy plane and above the impingement wall. Figure 2.5-(a) represents the velocity vector distribution under a cross-flow of 5 m/s and an ambient pressure of 0.4 MPa. The velocities were approximately 5 m/s and the direction distributions were almost uniform except in the areas behind the nozzle and near the wall. In order to show the detailed velocities, the cross-flow velocities in lines of x = 0 and 40 mm are plotted respectively, as shown in Figure 2.5-(b). In this study, the velocity curves are the average results obtained by conducting the tests five times. The difference of the maximum and average velocities is the positive error bar, and the negative error bar refers to the difference of the minimum and average velocities. It is noted that from y = 0 to 2 mm, the cross-flow velocity in the line of x = 0 mm is lower than that in the line of x = 40 mm owing to the effect of the nozzle tip, and from y = 48 mm to the wall, the velocity decreases gradually. Within the domain of y = 2 to 48 mm, the velocity is approximately 5 m/s that offers a uniform condition for the impingement spray.

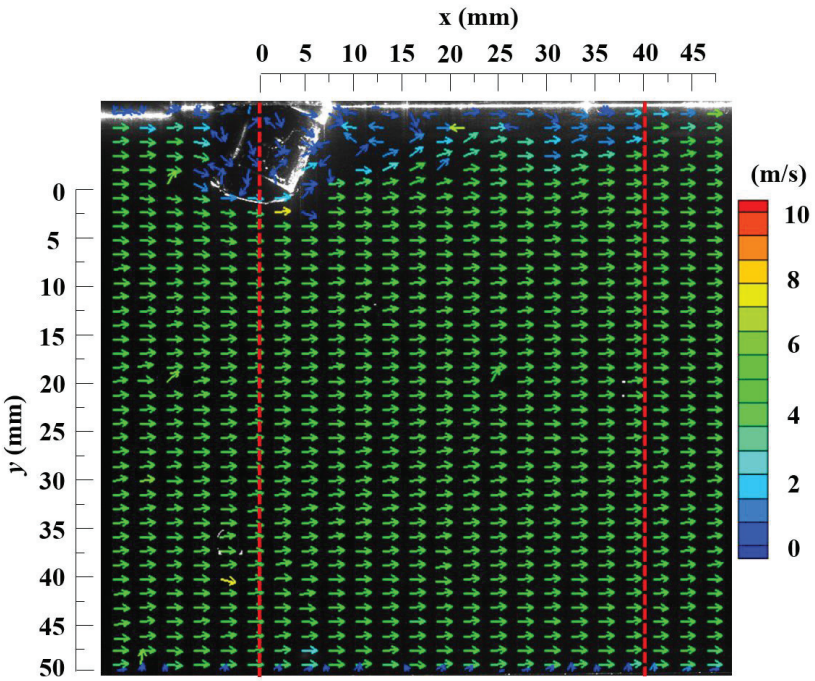

(a) Velocity distribution above the wall.

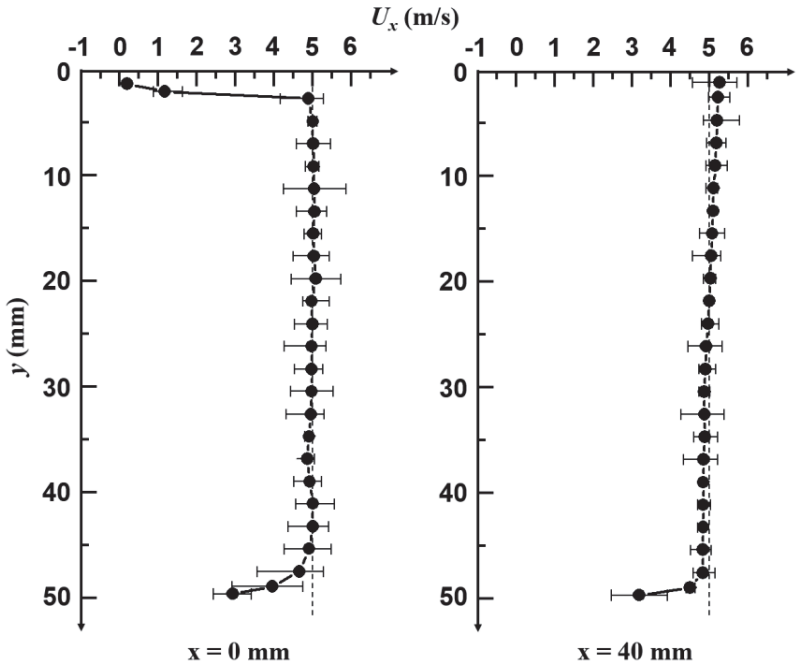

(b) Details of velocity distribution in lines of x = 0 and 40 mm.

Figure 2.5 Cross-flow velocity distribution above the wall at P_a = 0.4 MPa, U_x= 5 m/s

2.2 Trigger Control System

The triggering in the pressure wind tunnel experiments was decided by meeting two conditions, pressure and velocity in observation section. The pressure and velocity were always changing in this section, the experimental conditions should meet them simultaneously.

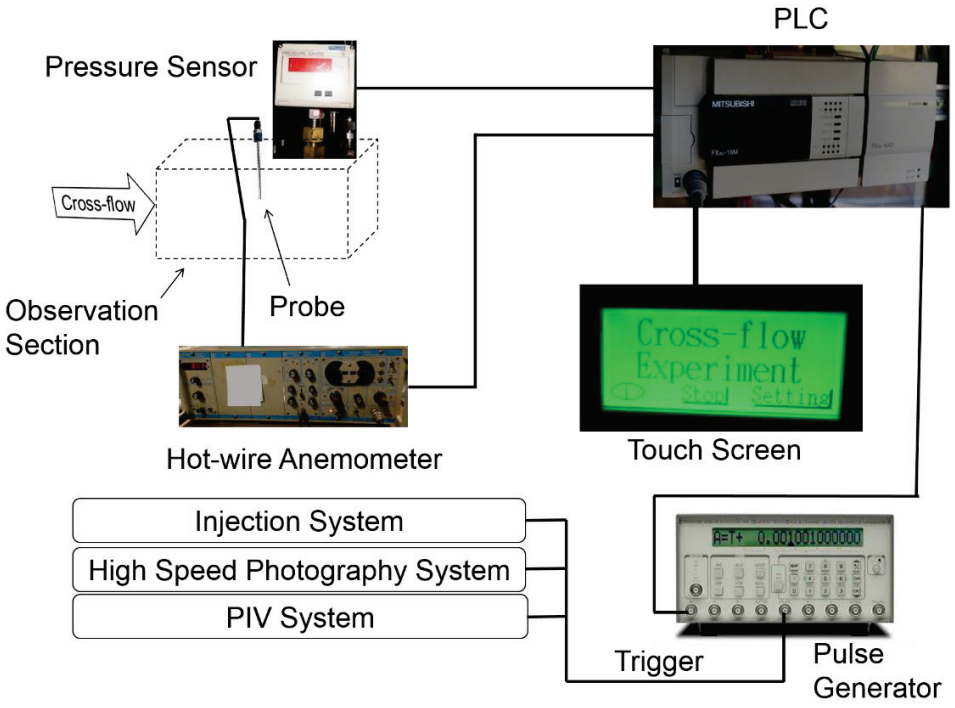

Figure 2.6 Control system for pressure wind tunnel.

A pressure sensor (NSK, GC75243) and hot-wire anemometer (KANOMAX 0251R-T5) were employed to detect the pressure and velocity signals simultaneously, as shown in Figure 2.6. The response times of them are short than 1 ms. Those signals of the pressure sensor and anemometer were converted from analog signals to digital signals by an analog-digital conversion (Mitsubishi, FX3U-4AD). The converted signals were transferred into a Programmable Logic Controller (PLC, Mitsubishi, FX3U-16MR/ES), which could compare with the two signals by wrote program. The interface of the system was a touch screen (Mitsubishi, GT1020-LWD), by which the pressure and velocity value could be displayed and operations could be taken. An experimental system for this experiments was written into the touch screen. When the pressure and velocity signals met the experimental conditions, a pulse would be outputted by PLC. This pulse was received by the pulse generator, which can control the injection system, high speed video

camera, and PIV system. In this experiment, the velocity measurement was intrusive way, because the difficulty of the velocity measurement in a sealed space with changing pressure.

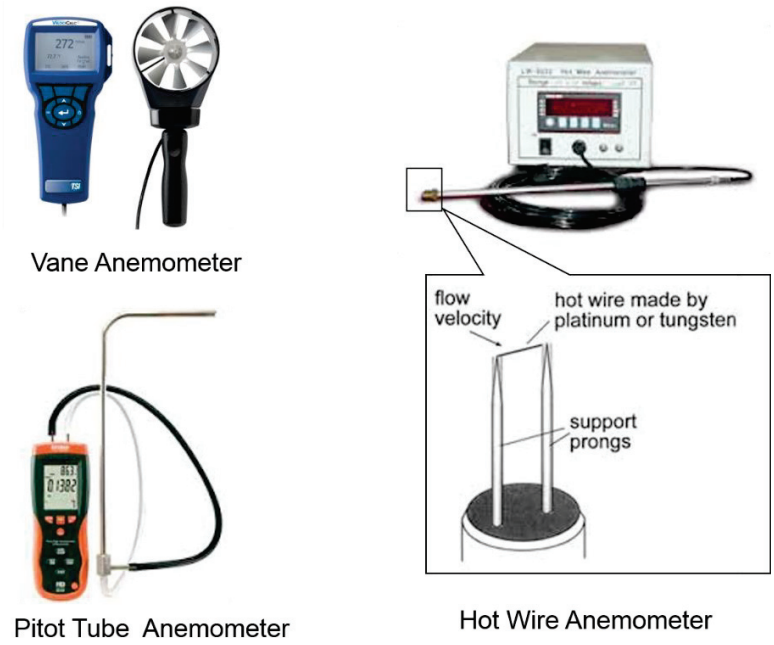

Figure 2.7 Typical Anemometers.

The mechanical anemometer, such as cup anemometer, vane anemometer, is widely used in the natural wind measurement. The principle of them is that the velocity is converted into electric signals using a set of cup or vane. The field of the air flow would be influenced very much after measuring. The Pitot tube anemometer is a very useful anemometer, which is poplar in aviation. The Pitot tube anemometer is a pressure-based velocity measuring device [66]. Hot-wire anemometer is a thermal anemometer, which can measure the velocity and turbulence. The hot-wire anemometer measures the rate at which heat is transferred form a heated filament to the flow in which it is immersed [67-69]. The structure of the probe is shown in Figure 2.7, the hotwire is made by platinum or tungsten.

In this investigation, the vane anemometer was excluded due to the effects on the air flow and the structure of the probe part. The Pitot tube anemometer could be used in the measurement, however, the transferring process was very complex due to the unsteady pressure, and the response time was also a problem. Hot-wire anemometer was used in this study, the response time of the anemometer is smaller than 1 ms, and the results were not influenced by the pressure changing. The testing point for the hot-wire probe was set on the middle of the observation

chamber, because in that area the velocity is more stable and the turbulence is the smallest.

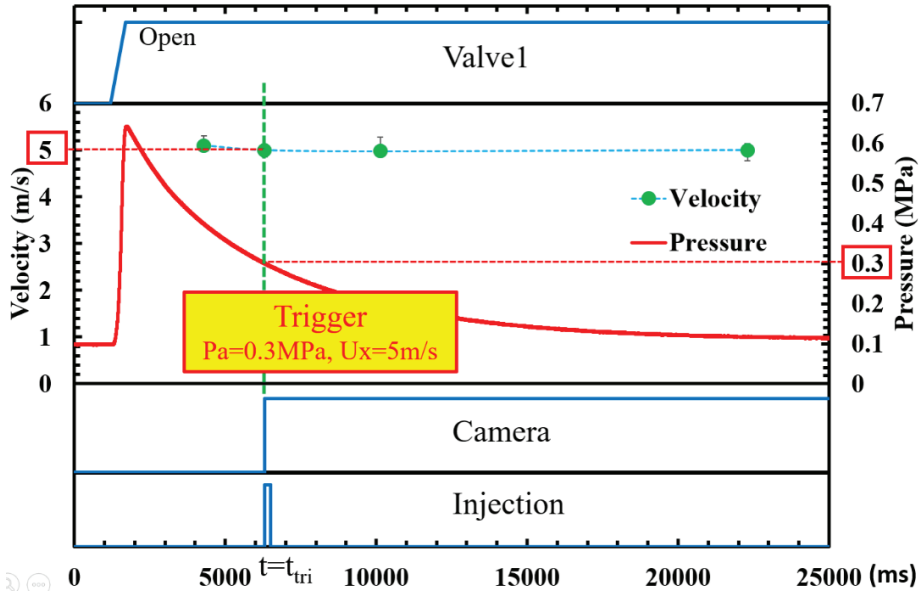

Figure 2.8 One example of operation for P_a=0.3MPa and U_x=5m/s.

The timing sequences of valve 1, cross-flow velocity, ambient pressure, camera, and injection under a cross-flow velocity of 5 m/s are shown in Figure 2.8. In this case, when valve 1 was fully opened the pressure in the chamber increased rapidly to a peak value and then dropped gradually. When the cross-flow velocity and ambient pressure would achieve the trigger condition (P_a=0.3MPa, U_x=5m/s), the pulse generator would be triggered to operate the spray injector and camera.

2.3 Experimental Methods

2.3.1 Spray visualization

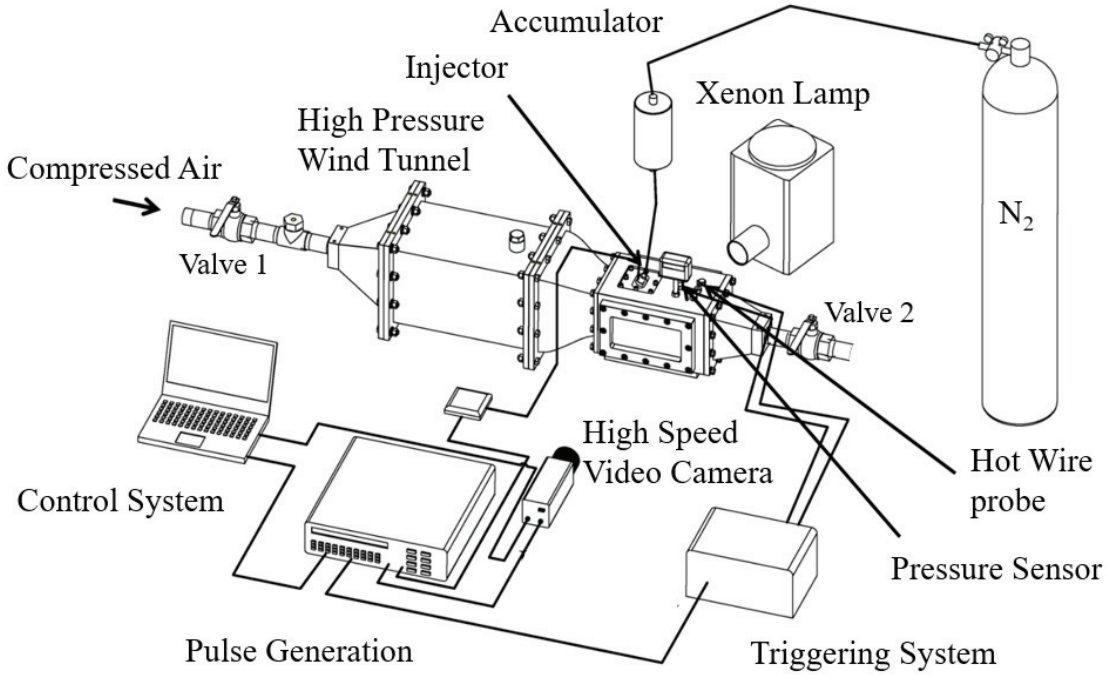

Figure 2.9 Direct photography using high speed video camera and xenon lamp.

To investigate the characteristics of the impingement spray structures in cross-flow, experiment of high speed photography has been taken, such as spray images in vertical and several horizontal planes. Direct photography of the impingement spray using high speed video camera and xenon lamp is shown in Figure 2.9. High pressure nitrogen was used to promote the process of spray. The injection duration was controlled through a pulse generator while injection time was operated by the fuel spray controller.

To obtain the three-dimensional spray images, the experimental devices were adjusted to suit the situations, as shown in Figure 2.10. The light source used in the experiment was a continuous wave laser sheet (DPGL-2W, Japan Laser Corp.) with wavelength of 532 nm and thickness of 1 mm. A high speed video camera (Photron FASTCAM SA-Z) was applied to record the tomographic images of the impingement spray with a frame rate of 20,000 fps and frame size of 896 × 760 pixels. To observe the impingement spray movements in the vertical and horizontal planes, the laser sheet illuminated the spray from the bottom and the side of the window

respectively, as shown in Figure 2.10-(a) and Figure 2.10-(b).

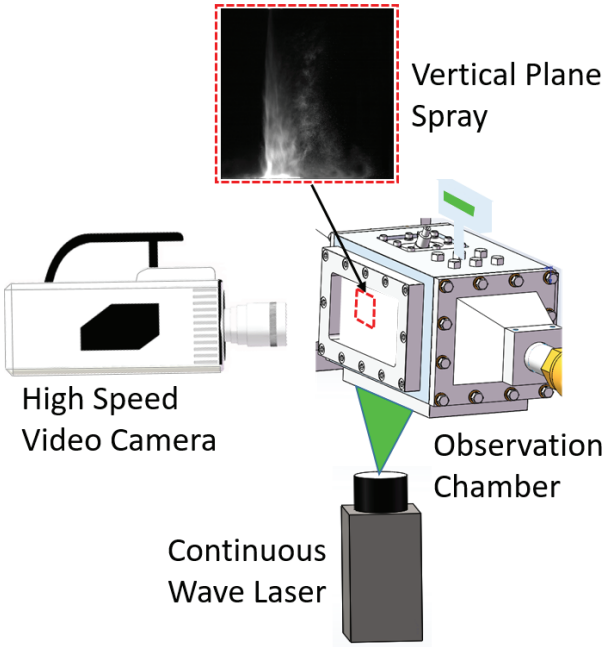

(a) Observation in a vertical plane

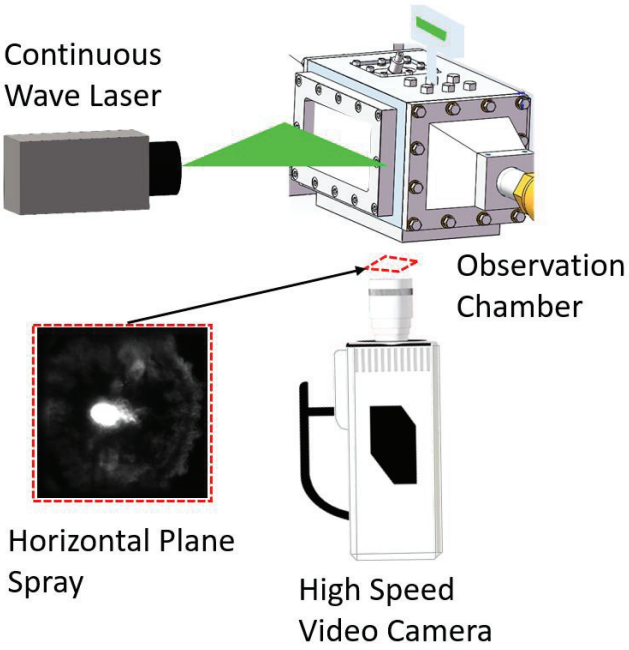

(b) Observation in a horizontal plane

Figure 2.10 Optical arrangement for impingement spray observation.

Figure 2.11 gives the optical arrangement of the near-field spray observation. There are three pieces of equipment in this imaging system: a xenon lamp (SX-131 UID501XAMQ), long-

distance microscope, and high speed video camera. In this study, diffused backlight illuminated the near-field spray with the frame rate of 40,000 fps and frame size of 1024 × 512 pixels. After calibration, the field of view is 4880 × 2440 μm^2.

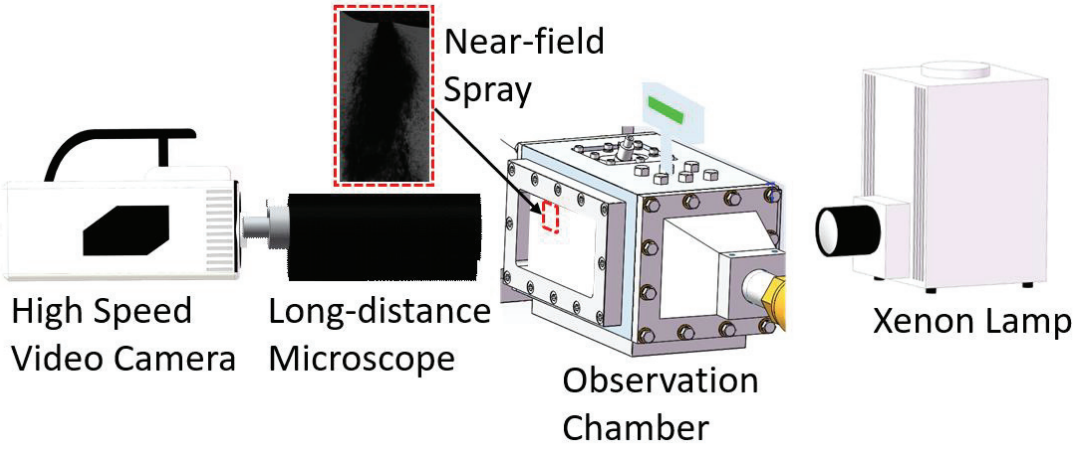

Figure 2.11 Optical arrangement for near-field spray observation.

2.3.2 PIA (Particle Image Analyzer)

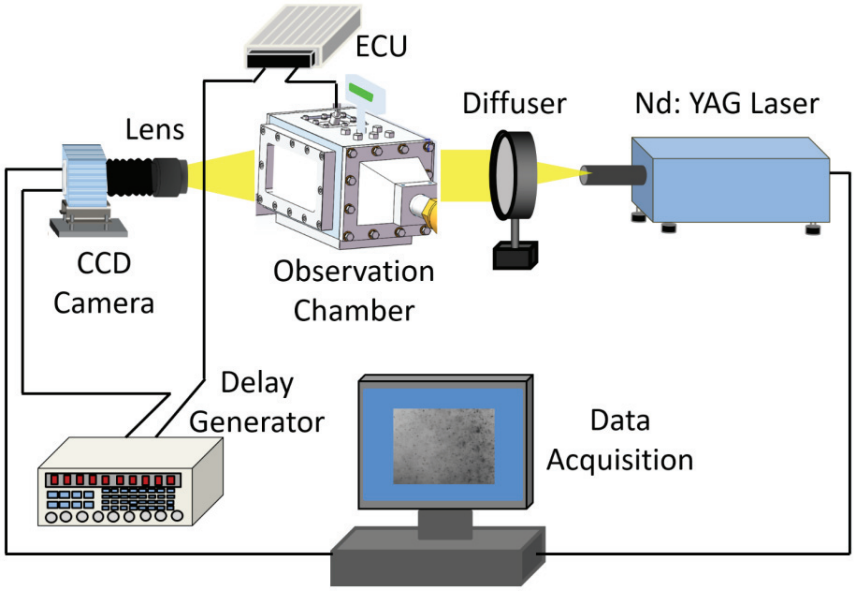

Figure 2.12 Schematic diagram of PIA system.

Figure 2.12 shows the schematic diagram of the PIA system for the detection of microscopic spray characteristics. A Nd: YAG laser with the wavelength of 532 nm was employed as the light source. A laser pulse of 6 ns duration has an energy of 10 mJ. The light beam was

expanded by a diffuser with the diameter of 100 mm to provide a uniform backlighting. A charge-coupled device (CCD) camera (Flowtech Research Inc., FtrNPC) linked with a long-distance microscope was used to capture the droplet distributions. The camera axis was collinear with the laser beam.

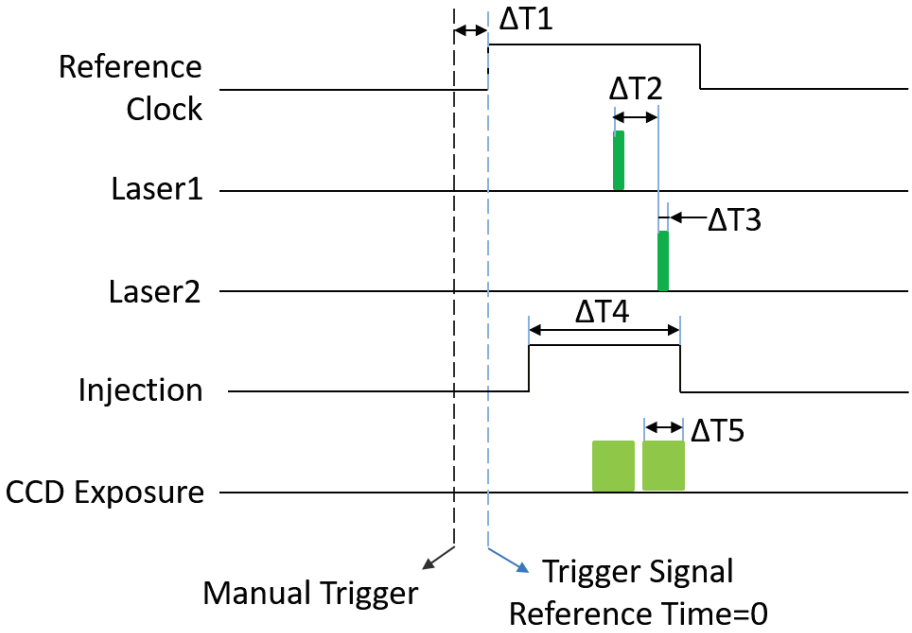

Figure 2.13 Timing chart for triggering signals of PIA system.

Figure 2.13 shows the timing chart of different triggering pulses for the PIA experimental study. The triggering pulses of the laser, the injection, and the CCD camera are synchronized by a synchronizing signal generator VSD 2000. The delay △T1 refers to the time between the manual trigger and the rising edge of the reference clock signal. △T2 (0.6 μs) indicates the interval between two laser pluses and △T3 (6 ns) indicates the laser pulse duration. The injection duration △T4 is 4 ms and the exposure time of the CCD camera △T5 is 200 μs.

2.3.3 PIV (Particle Image Velocimetry)

The velocity measurement in the single point of the cylinder can be taken by hot-wire anemometry or laser Doppler anemometry/velocimetry (LAD/LDV), which are used to measure the flow velocity and turbulence with high spatial resolution. The hot-wire anemometry can output a continuous recordings of velocity over time, however, the velocity direction cannot be obtained and the accurate calibration should be done before measuring. To understand the whole field

velocity distribution, and to quantify the velocities in the complex unsteady in-cylinder flows, particle tracking velocimetry (PTV) and particle image velocimetry (PIV) have been developed. Two dimensional maps of velocity of the testing plane in cylinder can be acquired. In PTV and PIV measurements, small particles, which can be illuminate and recorded by camera, are fed into the flow field. TV has been used for the characterization of induction-like flows in water analog engine [70]. A variation on PTV is streak photography, which can record the movement of the particle during the exposure period. PIV provides a means of achieving high spatial resolution two-dimensional velocity measurement. In PIV measurement, the particle displacement in a short period is calculated by two frozen images illuminated by the sheet laser, which can emit two high-energy laser pulses. The recorded image is divided into many small areas, in which the mean velocity is determined by performing a spatial correlation of the region. Because the spatial correlation process of PIV is not based on the single particle movement, a sufficiently high density of particles can be used in the measurement, hence the more complete and detailed velocity maps can be obtained than that in PTV. The micron-sized particles are allowed to use and the measurement can suit high-frequency flows due to the application of high-energy, short pulse duration laser illumination.

Particle image velocimetry (PIV) is originate from laser speckle photography (LSP), which has been used for measuring surface displacement fields. The principle of the PIV technique is that the velocity vector is calculated from the displacement of an element of fluid in a known time interval. The PIV technique requires a thin slice of the flow field to be illuminated by a laser light sheet in the simplest form. Particles in the flow within the light sheet scatter the light. The scattered light is detected by a camera which is placed at a right angle to the light sheet (Figure 2.14). The laser light sheet is double-pulsed (switched on and off very quickly twice) at a known time interval, Δt. The first frozen images of the initial positions of particles by the first pulse of the laser is taken by the camera. The second frame of the camera is exposed to the light scattered by the particles from the second laser pulse. Two images are obtained, the first showing the initial position of the particles and the second their final positions due to the movement of the flow field. Alternatively, the double exposed particle images can be recorded on the same photographic film.

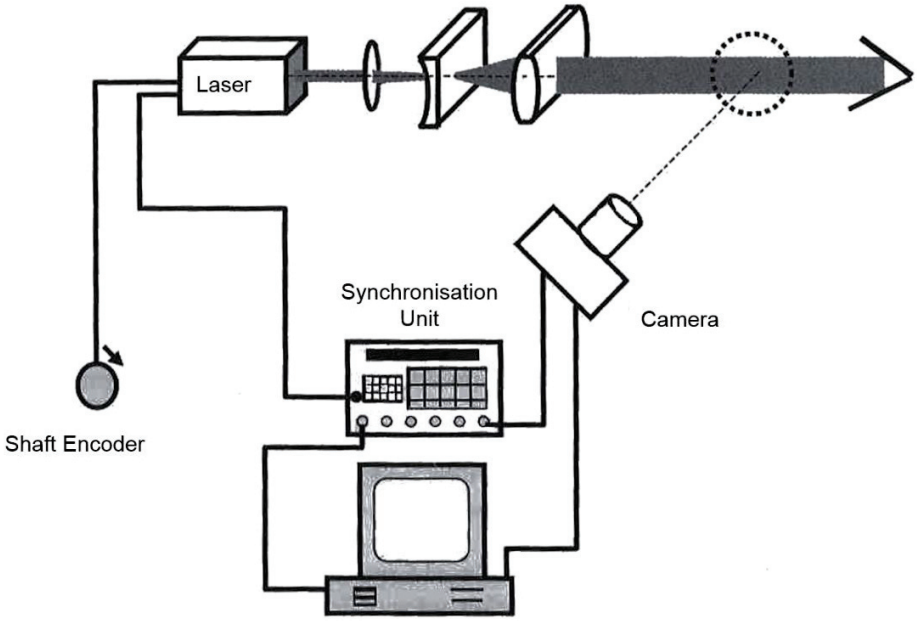

Figure 2.14 Typical PIV experimental setup.

The intersection volume between the region illuminated by the laser light sheet and the field of view of the imaging optics determines the region of the flow to be measured (see Figure 2.15). The interrogation area (IA) is defined as the smallest resolvable area of the film or detector. The interrogation volume (IV), which is projected back onto the measure region of IA, constitutes a single velocity vector. The displacement of the particle in the object plane (Δx and Δy) and the displacement in the image plane (ΔX and ΔY) have a correlation as,

$$\Delta x = \frac{1}{M}\Delta X, \text{ and } \Delta y = \frac{1}{M}\Delta Y \tag{2.1}$$

$$\mathrm{u} = \frac{\Delta x}{\Delta t}, \text{ and } \mathrm{v} = \frac{\Delta y}{\Delta t} \tag{2.2}$$

where, M is the magnification factor of the imaging optics, Δt is the time separation between the two laser pulses, u and v are the velocity projections on the object plane.

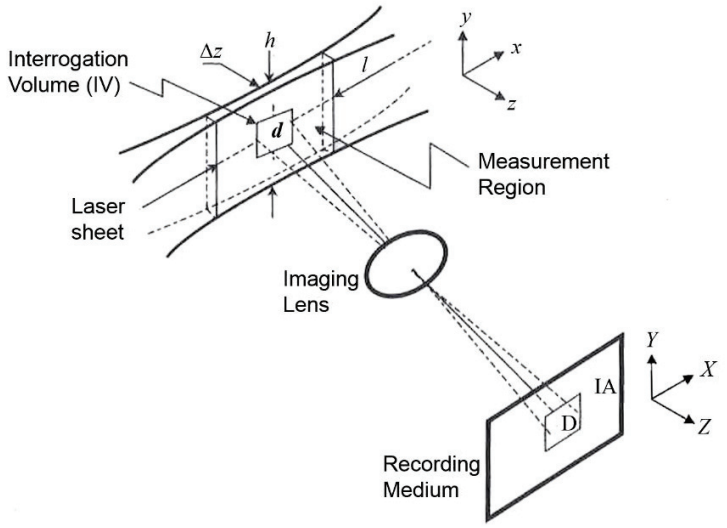

Figure 2.15 Definition of measurement region and measurement volume.

Illumination source and light sheet is preeminent important part in PIV system. Lasers are ideally suited as the light source for PIV measurements due to the conveniently collimated and intense form light. The average intensity of a particle image can be increased by shorter wavelengths compared to longer wavelengths. The blue-green wavelength light performs better in photographic emulsions than red light. The frequency doubled Nd: YAG pulsed laser is the most commonly employed in the PIV measurement. Two types of Nd: YAG lases have been used in PIV system, the single-cavity Nd: YAG laser with the double pulse option, and the twin-oscillator, twin-amplifier frequency doubled Nd: YAG laser. In the former, the first laser pulse is triggered externally, and the timing of the second pulse is adjusted by a potentiometer on the double pulse option, the pulse separation are limited to typically 20 μs to 200 μs, however, the energy of each pulse is weakened. In the latter, each of the pulse is triggered separately, there is no reduce of the pulse energy, however, the accurate co-alignment of the two separate outputs should be utilized in the system.

The supply of seeding particles is often significant for the quality and feasibility of PIV measurements. The requirements of particle seeding for PIV measurements are summarized by [71], including particle flow-following ability, particle light scattering characteristics, particle number density in the flow, tendency of particles to foul optical windows, tendency of particles to abrade cylinder surfaces, and ability of particles to withstand high-temperature environment in a fired engine.

There are two main categories of the PIV recoding modes: methods that capture the

illuminated flow onto a single frame (single-frame/double-exposure PIV) and methods that provide a single illuminated particle image for each illumination pulse (double-frame/single-exposure PIV). It is normal that the single-frame/double-exposure approach is used in photographic PIV recordings while the double-frame/single exposure is adopted in digital recording.

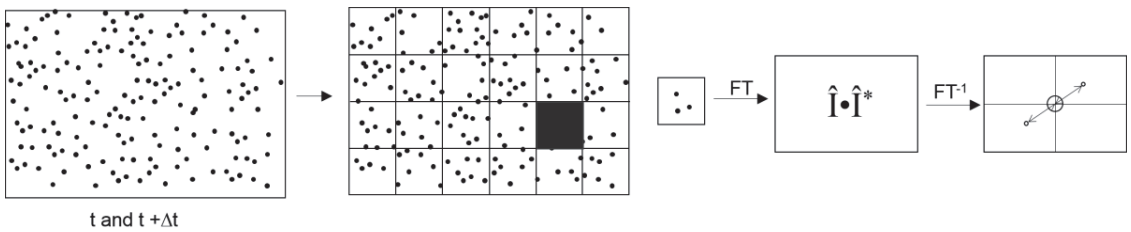

(a) Analysis of single frame/double exposure recordings: the fully digital auto-correlation method.

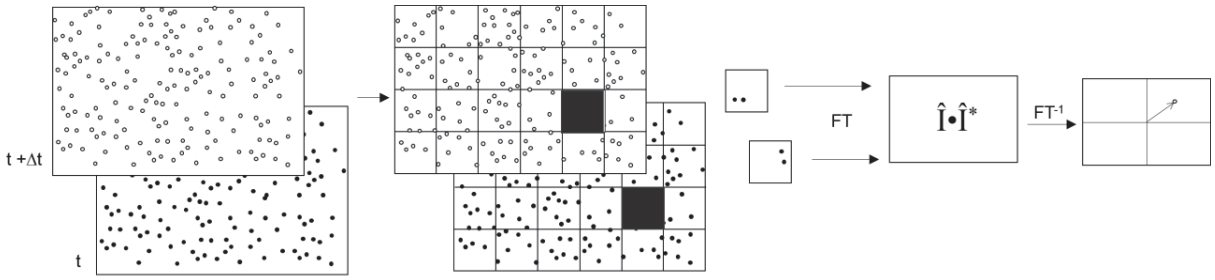

(b) Analysis of double frame/single exposure recordings: the digital cross-correlation method.

Figure 2.16 Two methods of recording analysis.

The cross-correlation algorithm owns the advantages of reducing the in-plain loss of correlation and increasing the correlation peak strength. The comparison of the flow chart of the auto-correlation and cross-correlation by FFT analysis are shown in Figure 2.16.

The two frames are sub-divided into a number of interrogation windows, the cross-correlation function $R_{II}(S,\Gamma,D)$ is calculated in each interrogation window. The displacement peak is determined, they correspond to the vectors of the particle image displacement. There are three terms including in the cross-correlation function,

$$R_{II}(S,\Gamma,D) = R_C(S,\Gamma,D) + R_F(S,\Gamma,D) + R_D(S,\Gamma,D) \quad (2.3)$$

where the R_C and R_F are the contribution of the background noise in the correlation plane. R_D represents the component of the cross-correlation function, which corresponds to the correlation of image of particles. Those image particles are obtained from two exposures.

$$R_D(S,\Gamma,D) = R_T(s-d)\sum_{i=1}^{N} V_0(X_i)\,V_0(X_i+D) \tag{2.4}$$

where d is the particle displacement in the image plane, s is the separation vector in the correlation plane. Therefore, the displacement correlation peak reaches a maximum when s=d for a given distribution of particles in the flow. The composition of peaks in the cross-correlation function is shown in Figure 2.17.

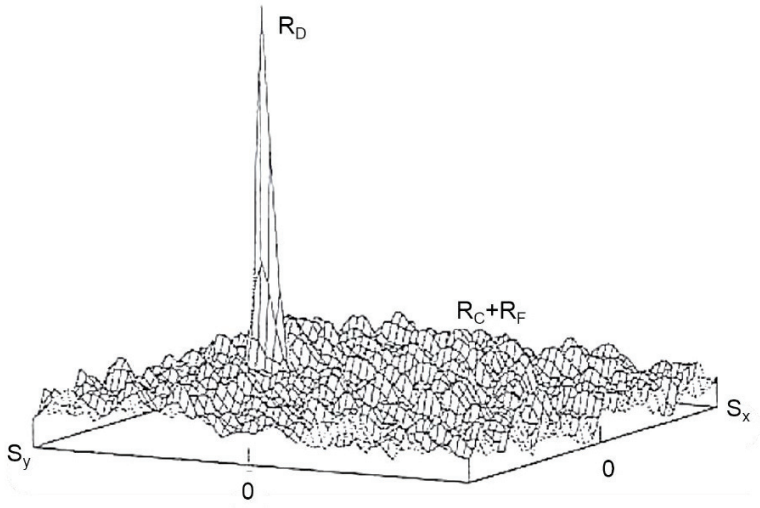

Figure 2.17 Composition of peaks in cross-correlation function.

The integral formulation of the cross-correlation function,

$$R_{II}(x,y) = \sum_{i=-K}^{K}\ \sum_{j=-L}^{L} I(i,j)\,I'(i+x,j+y) \tag{2.5}$$

The plain of the image is sub-divided into a number of interrogation windows with I rows and j columns. The I and I' are the variable intensity value coinciding to the samples of two images. The product of all overlapping pixel intensities generates one cross-correlation value for each sample shift (x, y). The composition of correlation plain is formed using this operation in a range of shifts. It should have a peak in the correlation plain, in which shift value aligns the particles of the samples with each other. In that case, the particle displacement in image plane can be calculated in the sample window according to the peak correlation value.

2.4 Summary

The experimental setups were presented, the details of the components were shown, such as the functions and arrangements. The composition of the wind tunnel is described in detail. The cross-flow velocity distribution was checked. The experimental setups were presented, the details of the components were shown, such as the functions and arrangements. The composition of the wind tunnel is described in detail. The cross-flow velocity distribution was checked.

The high speed photography was applied using Mie scattering method, and the spray structure, spray tip penetration, and spray vortex height could be analyzed by those images. The light source, which include the Xenon lamp and the continuous wave laser (sheet), were applied in this study. PIA system was employed to measure the droplet size and velocity distributions in local region in various locations. The PIV system was employed to measure the velocity distributions of the impingement spray. The principle of the PIV optical diagnosis method was introduced in this part.

Chapter 3 Impingement Spray Structure in Vertical Plane

In this part, the influences of the cross-flow velocity, ambient pressure and impingement distance on the spray structures in a vertical plane have been experimentally studied to provide physical insight into the impingement spray motion by using VCO and Sac hole nozzles. Spray tip penetration and vortex height were obtained from the impingement spray images for quantitative analysis.

3.1 Experimental Condition and Nozzle Type

3.1.1 Experimental condition

Table 3.1 Experimental conditions

Injection Conditions		
Fuel (Dry-solvent)	Density (20 ℃,1 atm) : 770 kg/m^3 Kinetic Viscosity (20 ℃,1 atm) : 1.3 (10^{-6}) m^2/s Surface Tension (20 ℃,1 atm) : 23.9 mN/m	
Injector Type	VCO, Single-hole	Sac hole, Single-hole
Hole Diameter : d (mm)	0.15	0.15
Injection Mass : Q_{inj} (mg)	4.36	4.36
Injection Duration : T_d (ms)	4	2.7
Injection Pressure : P_{inj} (MPa)	10	10
Ambient Condition		
Ambient Gas	Air	
Ambient Pressure : P_a (MPa)	0.1, 0.4	
Ambient Temperature : T_a (K)	293	
Cross-flow Velocity : U_x (m/s)	0, 2, 5, 10, 30, 50	
Impingement Distance : L_w (mm)	25, 50, 75	

The detailed experimental conditions are listed in Table 3.1. Dry-solvent was utilized as a test fuel in this study, since its physical property is close to that of gasoline. In addition, the dry-solvent possesses a higher ignition point. The density and viscosity of the dry-solvent are 770 kg/m^3 and 1.3 (10^{-6}) m^2/s (at 20 °C), respectively. The surface tension is 23.9 mN/m (at 20 °C). The injection duration was 4 ms and three impingement distances L_w were tested (25, 50 and 75 mm) under the cross-flow velocity range from 0 m/s to 50 m/s. The injection pressure was 10

MPa and the ambient pressure varied between 0.1 and 0.4 MPa. The measurement at every condition was repeated three times.

3.1.2 VCO and sac hole nozzles

The VCO nozzle and sac hole nozzle are widely used in the direct injection engines. For VCO nozzle, the injection hole is sealed by needle blocking, however, the sac hole nozzle has an additional volume at the bottom of the needle seat, as shown in Figure 3.1. The sac hole nozzle can produce a symmetric overall spray due to the increased distance between the needle seat and injection hole. The large liquid volume between needle and cylinder leads to that the fuel flows into the cylinder after the end of injection, resulting in increased hydrocarbon emissions. Compared with the sac hole nozzle, the VCO nozzle is superior in avoiding the fuel flowing into the cylinder after the end of injection. The fuel spray injected by the VCO nozzle is generally not well dispersed and increases soot emissions [72]. That spray usually shows asymmetric structure, especially under a low ambient pressure. So it is necessary to analysis the spray formation and spray feature of the VCO nozzle.

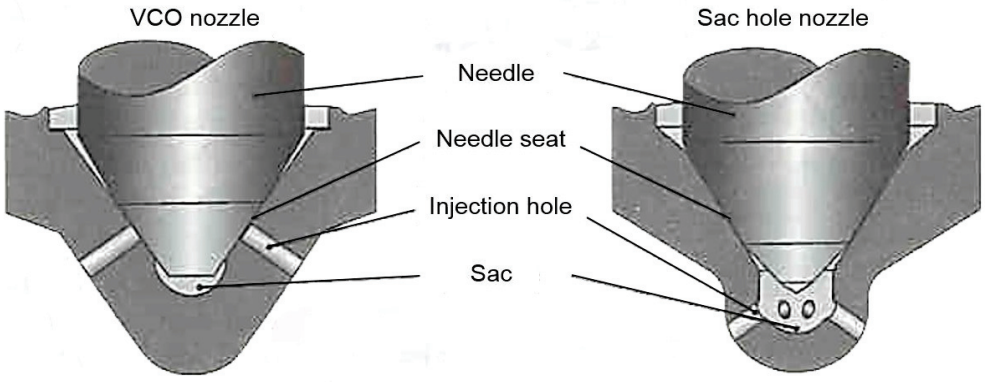

Figure 3.1 Geometric structures of sac hole and VCO nozzles

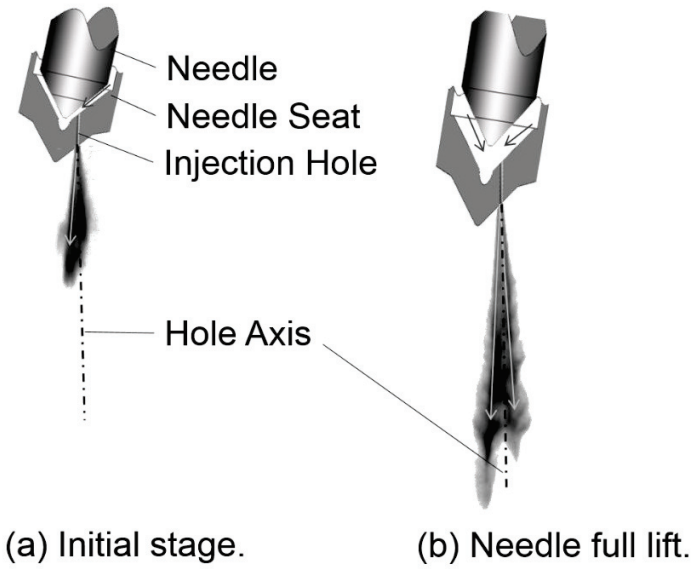

Figure 3.2 Spray feature of VCO nozzle

At the early period of injection, two asymmetric spray tips will be seen because of the geometric structure of the VCO type nozzle [73]. As shown in Figure 3.2-(a), at the initial stage of needle lift, the pressure is larger at the right upstream of the nozzle hole than that in the left part, then the main spray direction would incline to the left side, and the spray tip direction is not vertical. As the needle lifting, the pressure in the left part gradually increases, resulting in another tip in the right part of spray. After the needle is fully lifted, the upstream flow in the nozzle hole becomes symmetric, then the main spray direction coincides with the nozzle hole axis, see Figure 3.2-(b). For the measurements of spray tip penetration, the longest tip is used to make quantitative analysis.

3.2 Temporal Profiles of Impingement Spray

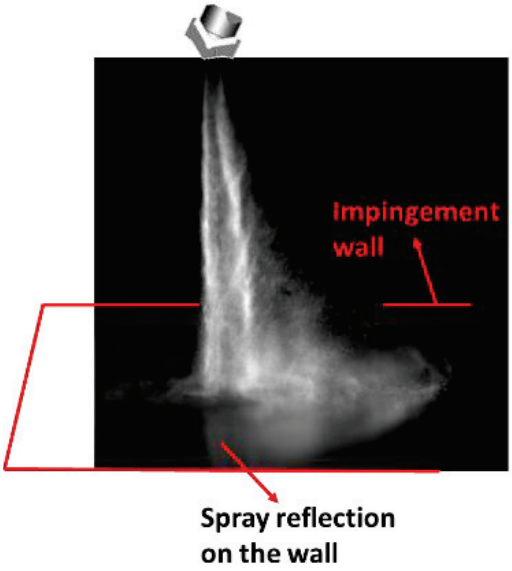

Figure 3.3 Impingement spray image by xenon lamp and high speed video camera.

From Figure 3.3 to Figure 3.9, the results were based on the VCO type nozzle, and a high speed video camera (Photron FASTCAM SAZ) was applied to record the impingement spray images. To observe the impingement spray development on the wall, the high speed video camera recorded the spray images with 14˚ depression angle and the xenon lamp was used as the light source. The experimental system was shown in Figure 2.9. Figure 3.3 gives the three dimensional view of the impingement spray image. And the impingement wall was drew, as shown in this Figure. It is seen that the impingement spray spread around on the wall surface and spray reflection present on the wall surface because the material of impingement wall is transparent acryl.

Figure 3.4 shows the false color images of impingement spray in time series under cross-flow of 5 m/s, ambient pressure of 0.1 MPa and the impingement distance of 50 mm. The colors indicate the light intensity scattered by droplets, qualitatively correspond to the droplets surface area density. The color value is arbitrary unit. It is noted that there were two bunches of spray because of the VCO type nozzle. For the first image of Figure 3.4, the impingement spray tip just touched on the wall at t = 0.8 ms after the start of injection (ASOI). The spray was almost perpendicular to the cross-flow direction, owing to the high axial momentum. From t = 1.3 ms ASOI, the post-impingement spray tip was bent to the cross-flow direction and spray spread in 3D direction on the surface of impingement wall. The spray density at downstream was higher than

that of other directions. Additionally, compared with pre-impingement spray, the density of post-impingement spray is lower due to the spray spreading on the wall surface. Therefore it was beneficial to form a lean mixture for impingement spray. It is seen that during t = 3.8 to 4.3 ms ASOI, lots of tiny droplets were blown away to downstream direction because of their low momentum. At the bottom layer, a cluster of droplets appears caused by secondary breakup of liquid film on the impingement wall surface [62].

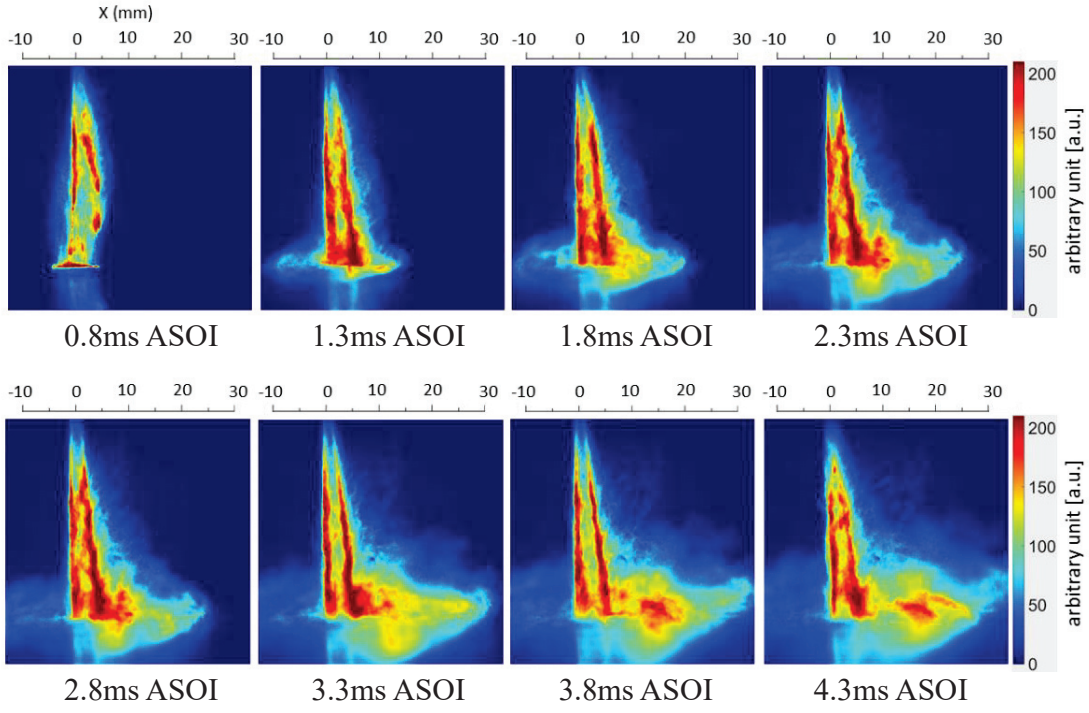

Figure 3.4 Impingement spray profiles in various times (U_x = 5 m/s, P_a = 0.1 MPa and L_w = 50 mm)

From Figure 3.4, it is seen that the impingement spray and the reflection of light were difficult to be distinguished. So it is not good enough to observe impingement spray behavior using xenon lamp as the light source in this experiment. To observe the impingement spray movements in the vertical plane, the laser sheet illuminated the spray from the bottom of the window, as shown in Figure 2.10-(a).

Figure 3.5 shows the image processing method and structure of an impingement spray, which was captured by laser sheet and high speed video camera. The raw image was shown in a false color format based on the image brightness. False color images were used in the study owing to the fact that they are beneficial to observe droplets distribution and the details of the spray

structure. The impingement spray structure mainly includes the main jet region, mixing flow region, wall main jet region, stagnation region, and wall-jet vortex [74]. The main jet region refers to the middle section of the incoming spray. After the spray impinged on the wall, the wall main jet appeared with secondary droplets generated owing to splash and rebound. Some secondary droplets were entrained by the wall-jet vortex formed around the wall. The stagnation region was located on the edge of the impingement region, where the droplets with exceedingly low momentum nearly stagnated. The droplets adhering on the wall surface contributed to the formation of the wall film.

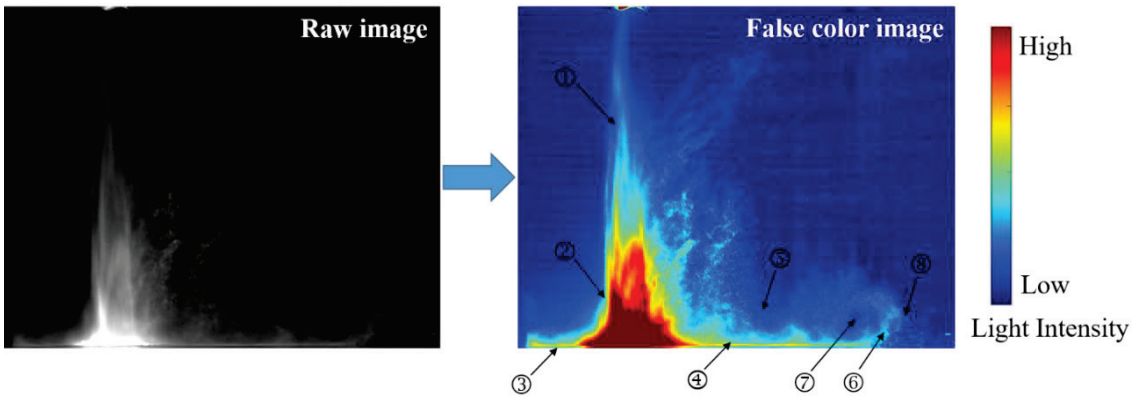

Figure 3.5 Structure of an impingement spray

Figure 3.6 shows the impingement spray profiles versus time under different cross-flow velocities and ambient pressures. For P_a = 0.1 MPa and U_x = 0 m/s case, after spray impingement on the wall, the spray vertical momentum was converted into radial momentum, and a wall-jet vortex developed along the wall surface, resulting in a lower density for the post impingement spray. Thus, a lean mixture was formed in the post impingement spray. Due to the window size of the observation chamber is not large enough the spray upstream structure was not captured, resulting in the spray is not symmetrical in Figure 3.6. For U_x = 5 m/s case, numerous tiny droplets in the middle and bottom of the spray were entrained by cross-flow, flowing to the downstream side. The reason is that small droplets at the edge of the middle and bottom spray lose their initial momentum in a short time and follow the cross-flow, while the droplets and ligaments in the near nozzle region tend to follow their initial trajectory owing to a high vertical momentum. In the windward side, the spray edge is smooth, which is different from the quiescent case that showed

saw-tooth waves for the edge. We believe that the smooth edge occurred under the cross-flow condition owing to the spray breaking up into tiny droplets at the edge and the droplets being blown downstream. The main spray body was shifted downstream, and the spray trajectory had a large distortion in the windward side. The wall-jet vortex in the downstream side also became larger and penetrated further owing to a large stream wise momentum under cross-flow condition. It can be seen that cross-flow promote spray dispersion, and the droplets distributed non-uniformly at the leeward side. Moreover, the spray became dense and the penetration velocity of the spray tip was decreased because increased density of the ambient gas leads to increased air resistance. It was interesting to note that under the cross-flow condition, a considerable amount of tiny droplets were observed in the leeward side at higher ambient pressure, owing to the larger momentum flux of cross-flow.

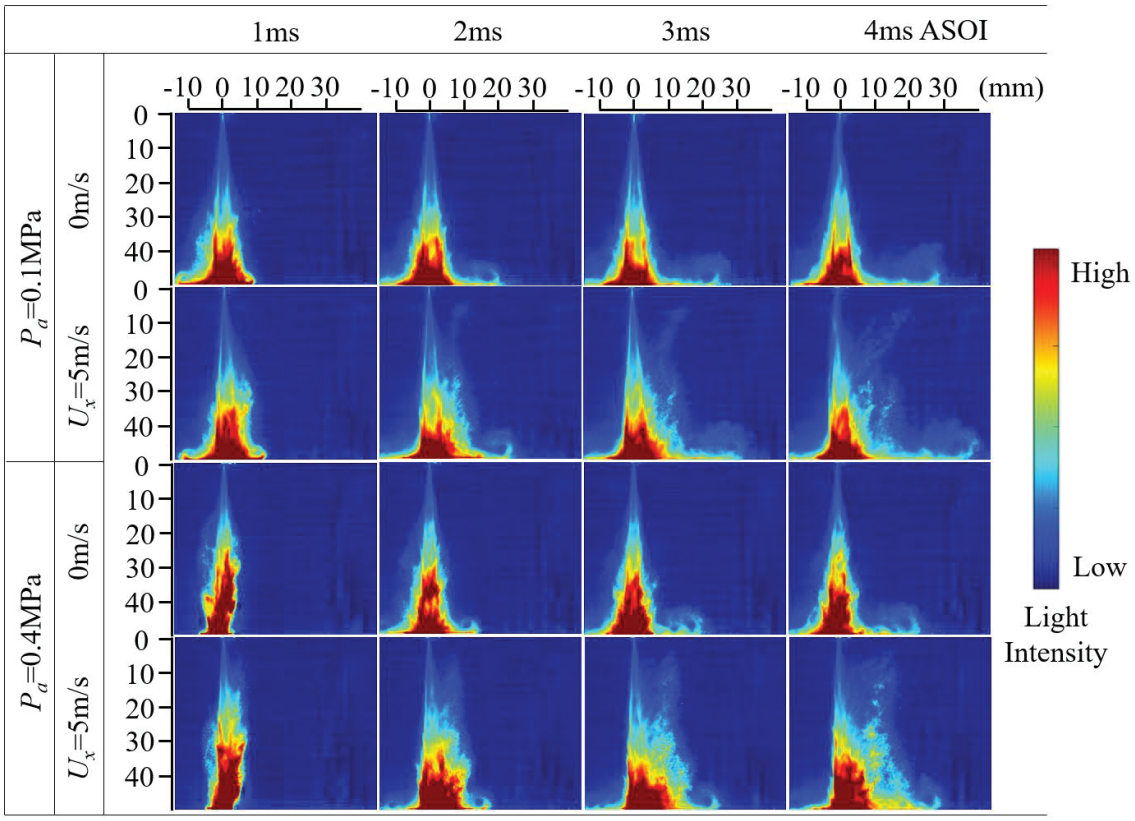

Figure 3.6 Comparisons of the impingement spray evolutions at different cross-flow velocities and ambient pressures

Interestingly, for P_a = 0.1 MPa and U_x = 5 m/s case, at 4 ms ASOI, the droplets chain distributed as an obliquely upward structure in the leeward side. In order to clearly observe the

droplets chain distribution, the spray structure in the red rectangle was magnified, as shown in Figure 3.7. The reason of the droplets chain formation is that the breakup of the bag membrane leads to numerous small droplets in the cross-flow, and the droplet vertical velocity is reduced along the cross-flow direction, as shown in Figure 5.7-(b). Previously, Ng et al. [51] has experimentally investigated the bag breakup process under the cross-flow condition, and they showed that a remarkable feature of spray jet breakup was the surface wave formations along the leeward edge of the spray column. The surface wave grew, and eventually the thin membrane broke into a large number of small droplets. At the 10m/s cross-flow condition, the droplet distributions in the downstream were inhomogeneous and some blank areas shown by the white dashed line can be observed in the tomographic image. This phenomenon may be attributed to the spray fluctuation in the horizontal plane, which leads to the Karman vortex-like structure [75].

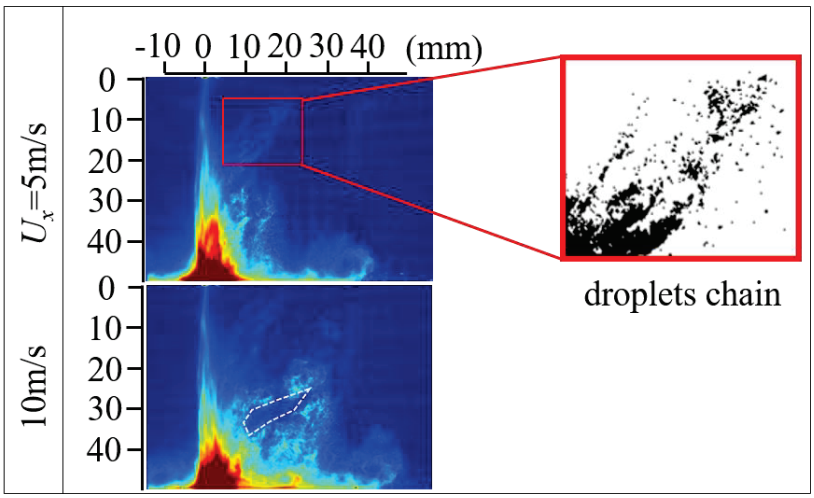

Figure 3.7 Impingement spray structures at cross-flow velocities of 5 m/s and 10 m/s (P_a = 0.1 MPa and t = 4 ms ASOI)

The wall-jet vortex structure is a key feature for the impingement spray that could promote air entrainment and fuel-air mixture formation. Figure 3.8 displays the effects of ambient pressure and cross-flow velocity on the vortex structure at 4 ms ASOI. At atmospheric pressure, the rolled-up spray tip spread along the wall in a circular shape and it spread further downstream with increasing cross-flow velocity. In addition, the tip position of wall-jet vortex is indicated by the red line. The tip becomes much sharper at higher cross-flow velocity. This is because cross-flow increases the radial velocity of the wall-jet vortex, leading to an increased shear force from the ambient air. Moreover, the phenomenon of a larger vortex structure and considerably severe

breakup under cross-flow conditions suggests that the cross-flow is beneficial for spray dispersion and mixture formation. Under 0.4 MPa ambient pressure, the vortex shape was more regular than that under 0.1 MPa ambient pressure. At 5 m/s cross-flow condition, the vortex height at 0.4MPa is about 18% smaller than that of 0.1MPa. This is primarily because of the larger drag at a higher ambient pressure that leads to decreased penetration velocity and consequently a less severe breakup occurrence. It is noteworthy that though increasing the ambient pressure causes a weak air-entrainment motion, this does not mean that the fuel-air mixture formation would become poor under higher ambient pressure because the air-entrainment has higher density.

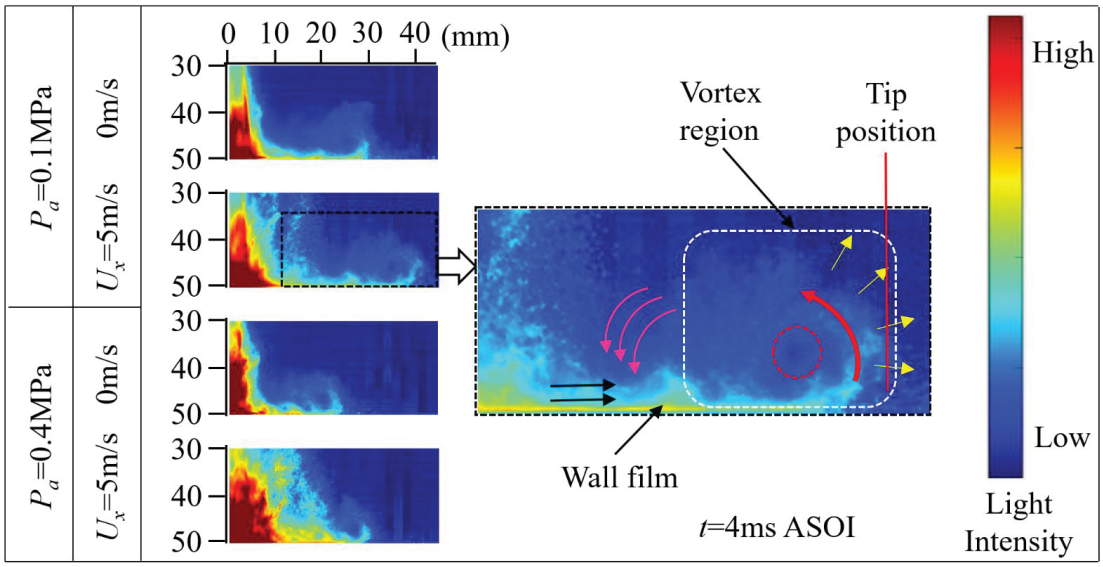

Figure 3.8 Spray wall-jet vortex structures at different cross-flow velocities and ambient pressures.

In order to better analyze the behavior of the wall-jet vortex, the vortex structure was enlarged, as shown in the right image of Figure 3.8. It could be seen that the rolled-up structure is formed near the wall surface caused by the interaction between droplets and gas. Droplets were generated by secondary breakup of liquid film on the wall. The rolled-up motion and momentum exchange between the ambient air and fuel spray occurred near the vortex region. It illustrates that the ambient gas could be entrained into the spray jet when the vortex is growing. In this image, the red arrow indicates the global direction of rolled-up motion of the vortex, and the yellow arrows display the velocity direction of single droplet in the vortex edge; the pink arrow represents the direction of air-entrainment near the wall-jet region, and the black arrow indicates the flow direction of wall-jet. It is interesting to notice that the spray concentration is considerably low in

the vortex core region, which is indicated by a red circle. The tip of the wall-jet vortex penetrated further compared to the fuel film distribution above the wall surface; thus, the fuel film edge is at a position behind the vortex tip.

Figure 3.9 shows the effect of impingement distance on the spray profiles. At smaller impingement distance case, more splashing droplets exited in front of spray vortex. This is because the higher velocity of vortex rotation due to the lower momentum loss causes the droplet velocity larger than centripetal force and separate itself from the spray vortex. In addition, after impingement the fuel-air mixture area increases with increasing impingement distance. The reason is that the air-flow momentum passing through spray sectional area is increased at larger impingement distance resulting in numerous tiny droplets entrained by cross-flow.

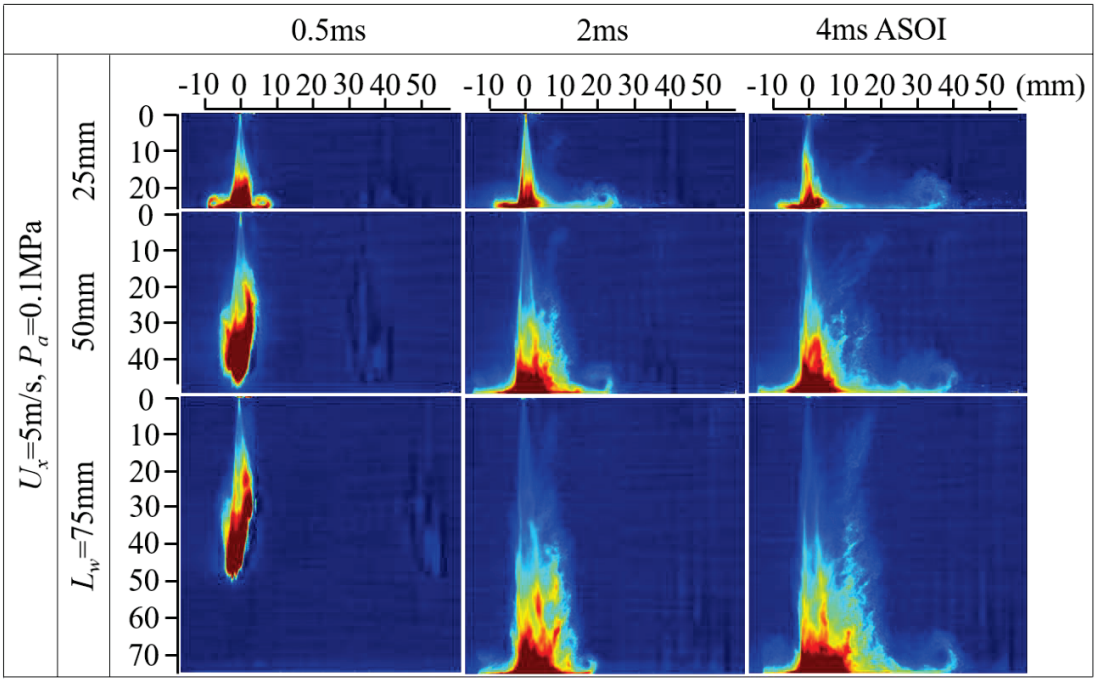

Figure 3.9 The impingement spray profiles at impingement distance of 25, 50 and 75 mm (P_a = 0.1 MPa and U_x = 5 m/s)

To understand the effect of the high cross-flow velocity on the spray structure, the spray profiles injected by Sac hole nozzle at cross-flow velocities of 10 m/s, 30m/s and 50 m/s are listed in Figure 3.10. A high speed video camera (NAC Image Technology Inc., HX-3) was applied to record the tomographic images of the impingement spray.

At the cross-flow velocity of 10 m/s, no significant bend is observed in the windward side and the profiles are enlarged in the leeward side. With the increase of the cross-flow velocity,

the bend phenomenon appears in the windward side. The bended area appears from middle part of the spray and the bended content increases with increasing the cross-flow velocity. At higher cross-flow velocity, the movement distance to downstream region becomes farther at the bottom part of the spray. It is noteworthy that no droplets distributed at the upper part of leeward side spray in 10 m/s cross-flow, however, larger amount of droplets distributed at the upper part of leeward side spray in 30 and 50 m/s cross-flows. This is because higher cross-flow velocity ($U_x \geqslant 30$ m/s) can promote the spray breakup at the upper part. In addition, we found that at 10 m/s cross-flow velocity case, the movement distance of wall-jet vortex is farther than that of the droplets at middle part. However, at 30 and 50 m/s cross-flow velocity cases, the movement distance of wall-jet vortex and the droplets at middle part is almost same. The possible reason is that the spray breakup become more severe at higher cross-flow velocity condition. More tiny droplets were entrained to downstream region and the droplets horizontal momentum acquired from cross-flow were increased.

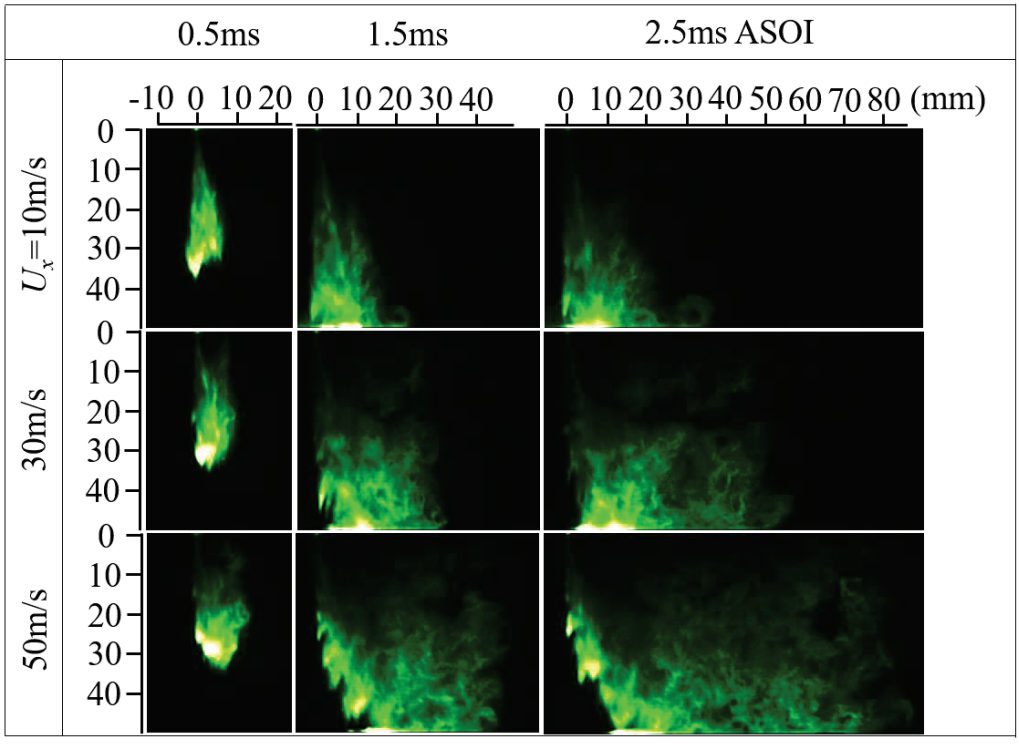

Figure 3.10 Impingement spray structures at cross-flow velocities of 10 m/s, 30m/s and 50 m/s (P_a = 0.1 MPa and L_w = 50 mm)

Figure 3.11 shows the spray profiles at the early stage (0.5 ms ASOI) of spray evolution. At the ambient pressure of 0.1 MPa, the penetration obviously decreased with increasing of the

cross-flow velocity. This might be because the shear force increased at higher cross-flow velocity, causing the breakup of spray tip then the vertical velocity of spray tip decreased.

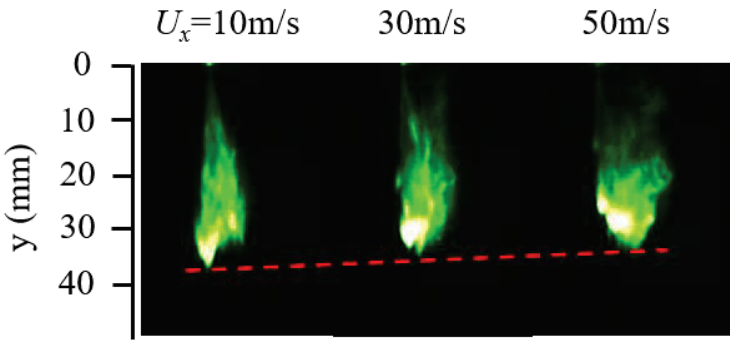

Figure 3.11 Spray variation under different cross-flow velocities at P_a = 0.1 MPa and t = 0.5 ms ASOI.

3.3 Spray Outlines and Spray Distortion

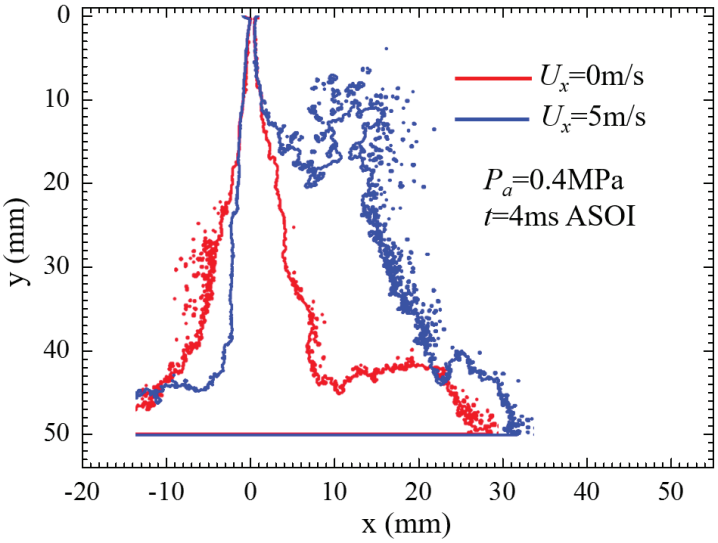

Figure 3.12 Comparison of spray outlines under different cross-flow velocities at P_a = 0.4 MPa and L_w = 50 mm.

In Figure 3.12, the effect of cross-flow velocity on the spray outline is analyzed at the ambient pressure of 0.4 MPa and time of 4 ms ASOI. In order to clearly distinguish the outline of the spray, a threshold level of 20 out of 255 was used. The red and blue curves represent the spray outlines under the cross-flow velocities of 0 and 5 m/s, respectively, and the difference between them is significant. At no cross-flow condition, the spray outline is distributed almost symmetrically, however, under the cross-flow velocity of 5 m/s, the outline shifted downstream. The area of outline at cross-flow condition was evidently larger than that of without cross-flow, and this reveals that the cross-flow could improve spray dispersion. Two interesting phenomena have been illustrated in this figure. First, under the cross-flow condition, numerous tiny droplets were distributed in the upper region of the spray at the leeward side, and the droplets distribution was non-uniform. This illustrates that the movement of the droplets in this part has exceeded the laser sheet plane. We consider that this phenomenon maybe caused by spray fluctuation and it is further explained in detail in Figure 5.8. Secondly, in the windward side, without cross-flow, some droplets were distributed near the outline; however, under cross-flow condition there was no droplet.

The liquid-to-air momentum flux ratio q is an important parameter used to determine the distortion of the spray profile [76]. The definition of q is given by

$$q = \frac{\rho_l U_l^2}{\rho_g U_x^2} \tag{3.1}$$

where ρ_l is the fuel density, U_l is the injection velocity, ρ_g and U_x are the density of ambient air and cross-flow velocity, respectively. In theory, when the values of q are similar, the distortions in the windward side should agree satisfactorily.

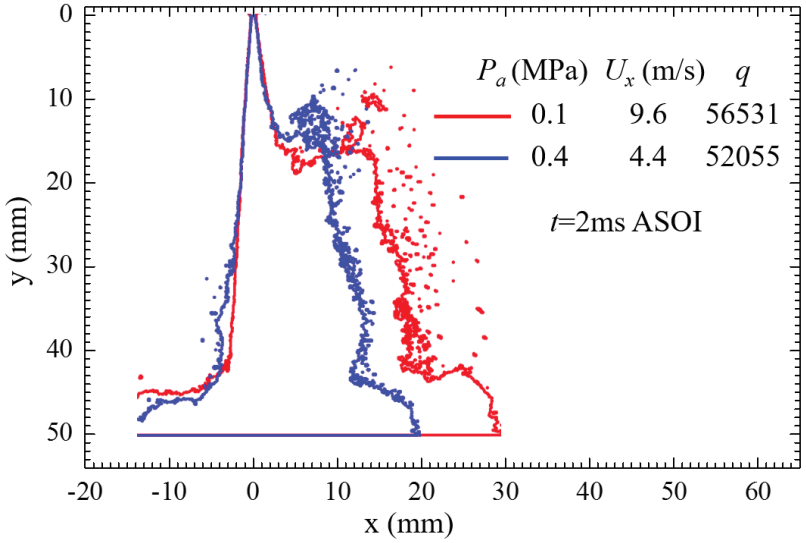

Figure 3.13 Spray distortion under nearly liquid-to-air momentum flux ratio.

Figure 3.13 compares the spray outlines under almost the same momentum ratio. The red line refers to the spray outline under ambient pressure of 0.1 MPa and cross-flow velocity of 9.6 m/s. The velocity is set at 4.4 m/s under 0.4 MPa ambient pressure, as shown in the blue line. According to the PIV results in previous experiment [77], the spray velocity at 0.1 MPa and 0.4 MPa were 93.4 m/s and 82.2 m/s, respectively. Under two cases it can obtain the close value q (56531 and 52055). The outlines in the windward side agree satisfactorily, especially at the upper part. However, in the leeward side the spray outline extended further at lower ambient pressure. The reason is that at lower ambient pressure the cross-flow velocity was higher and air resistance decreased thus it is easier for spray to flow downstream. Based on the definition of q, when the ambient pressure or cross-flow velocity increases, the momentum ratio decreases resulting in the downstream shift of the outline in the windward side. One interesting phenomenon is that in the outline of the windward side, almost no droplets were present, but there were numerous droplets near the outline in the leeward side. This is primarily because the spray or ligament disintegrated

owing to shear force under cross-flow, especially in the windward side. The cross-flow induced secondary breakup of spray and the droplets were shifted downstream.

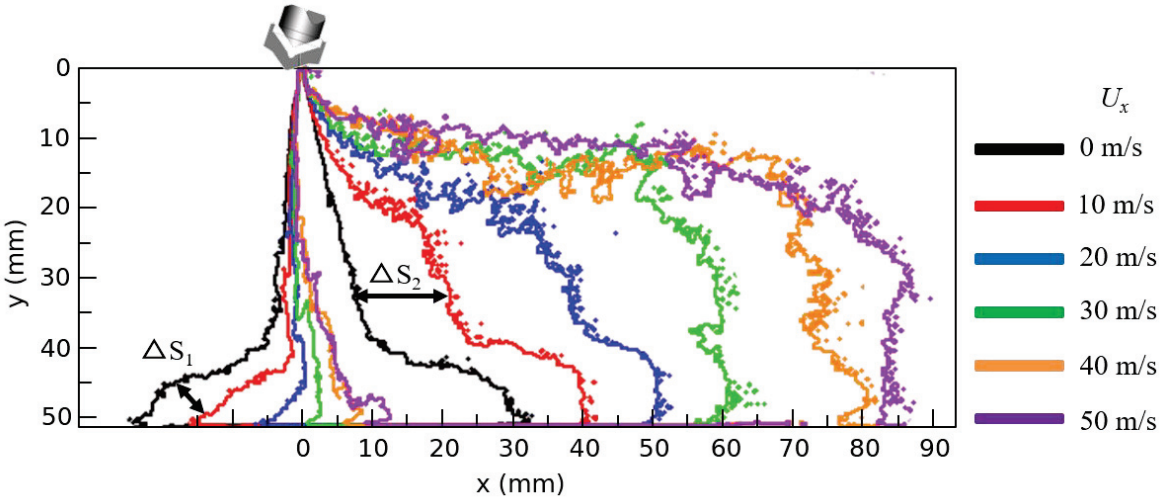

Figure 3.14 Spray outlines under different cross-flow velocities at P_a = 0.1 MPa and L_w = 50 mm (t = 2.7 ms ASOI).

Figure 3.14 gives the outlines of spray under different cross-flow velocities, in which the ambient pressure is 0.1 MPa and the injection time is 2.7 ms ASOI. It is seen that under no cross-flow condition, the outline of the spray is distributed almost symmetric, however, with increasing the cross-flow velocity, the outline is further shifted downstream side along the direction of cross-flow. The distances (ΔS_1) of the outlines at the upstream side of the spray decrease against time, however, the distances (ΔS_2) at the downstream side of the spray seem to be uniform.

3.4 Spray Tip Penetration and Spray Vortex Height

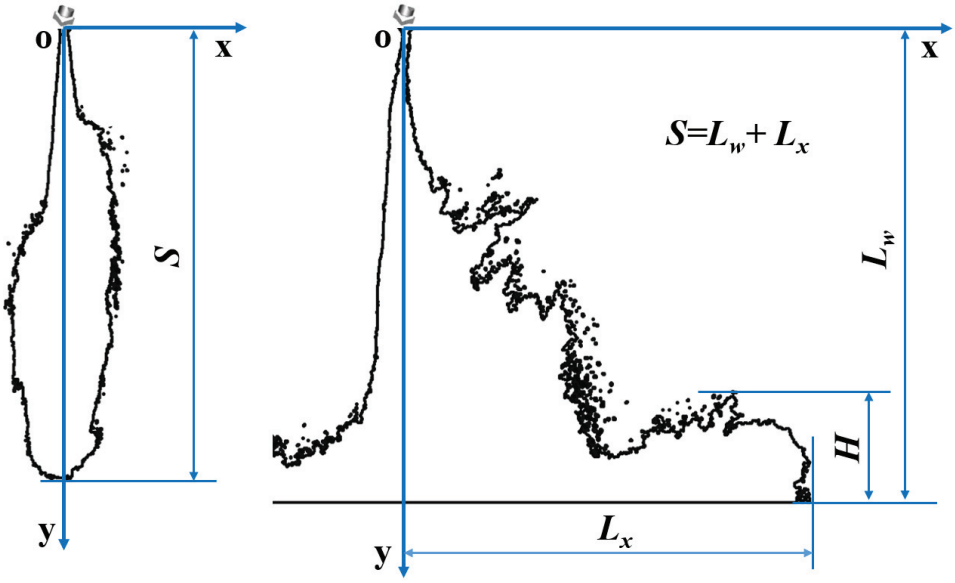

(a) Before impingement (b) After impingement

Figure 3.15 Definitions of spray tip penetration *S* and vortex height *H*.

The spray tip penetration *S* and the vortex height *H* suggest an air entrainment rate and a mixture ratio, which are two important parameters in impinging spray analysis [78–79]. Figure 3.15 provides the definitions of *S* and *H* based on the spray profiles. As shown in Figure 3.15-(a), the vertical distance from nozzle exit to spray tip is used to express the spray tip penetration before impingement. After impingement the spray tip penetration is defined as the sum of the impingement distance L_w and radial length L_x, and the vortex height *H* is the highest position of the vortex from the wall surface in the vertical direction (see Figure 3.15-(b)). The threshold of outline curve is 20 out of 255. The experimental error as shown by the error bars is added in the rest of figure. The error percentages of spray tip penetration and vortex height are below 10% and 28%, respectively.

Figure 3.16 illustrates the spray tip penetration under cross-flow velocities of 0, 2 and 5 m/s at different ambient pressures. Under all conditions, the development of spray tip penetration could be divided into two stages. In the first stage, the penetration increased linearly against time before impingement, and in the second stage, the growth of penetration became slow. This phenomenon may be attributed to the fact that in the second stage, the post impingement spray breakup occurs and results in the formation of a considerable amount of droplets.

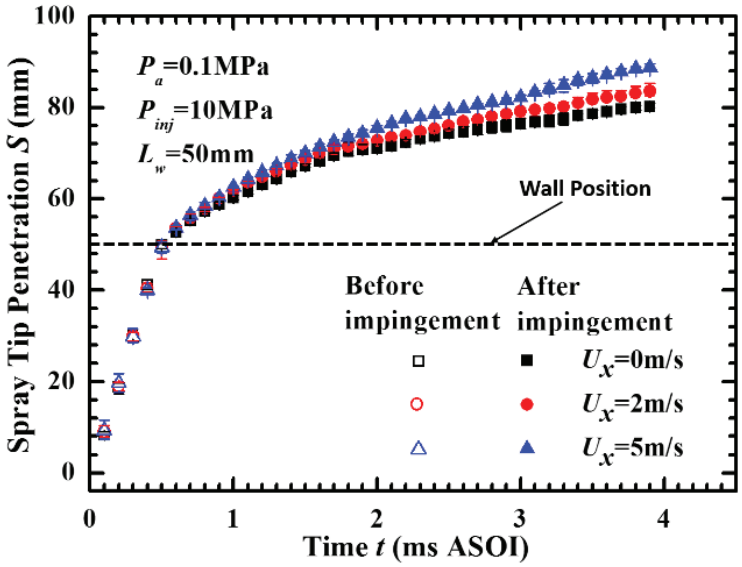

(a) P_a = 0.1 MPa

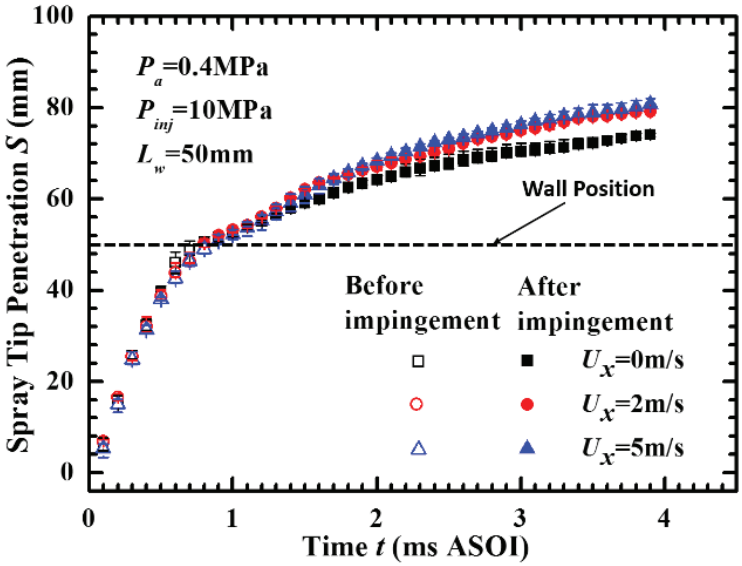

(b) P_a = 0.4 MPa

Figure 3.16 Comparisons of spray tip penetration.

For the deposition-splash criterion, the dimensionless number, *K* number, can be used as the splashing threshold parameter for both the smooth and the rough surfaces [80]. The *K* number is defined as

$$K = Oh \cdot Re^{1.25} = We^{0.5} \cdot Re^{0.25} = \rho^{0.75} v^{1.25} d^{0.75} \sigma^{-0.5} \mu^{-0.25} \tag{3.2}$$

$$We = \frac{\rho v^2 d}{\sigma} \tag{3.3}$$

$$Re = \frac{\rho v d}{\mu} \tag{3.4}$$

where ρ is the fuel density, v is the droplet velocity, d is the droplet diameter, σ is the surface tension and μ is the droplet viscosity. Mundo et al. found that at low K number (K<57.7), the liquid has not enough kinetic energy to overcome surface tension and gravity during the deformation process, leading to complete deposition of the liquid. At high K number (K>57.7), as the droplet touches the surface, a corona around the deforming droplet is formed. High kinetic energy leads to an instability and finally results in a disintegration into secondary droplets. In this study, at 0.1 MPa ambient pressure, 5 m/s cross-flow velocity and 4 ms ASOI, the droplet diameter was 28 μm and velocity was 29 m/s measured by PIA (Particle Image Analyzer) system in the location of x = 2 mm, y = 48 mm, z = 0 mm. In this case (K=725.4>57.7) most droplets splash off the wall after impingement. Moreover, a friction force from the wall could be regarded as another factor that decelerates the spray tip velocity after the spray impinged on the wall. With increase in the cross-flow velocity, the spray tip penetrations markedly increased after impingement, while before impingement the penetrations were nearly constant. At higher ambient pressure, at a given time the spray tip could penetrate shorter distance, and the penetration difference between various cross-flow velocities is smaller than that under low ambient pressure.

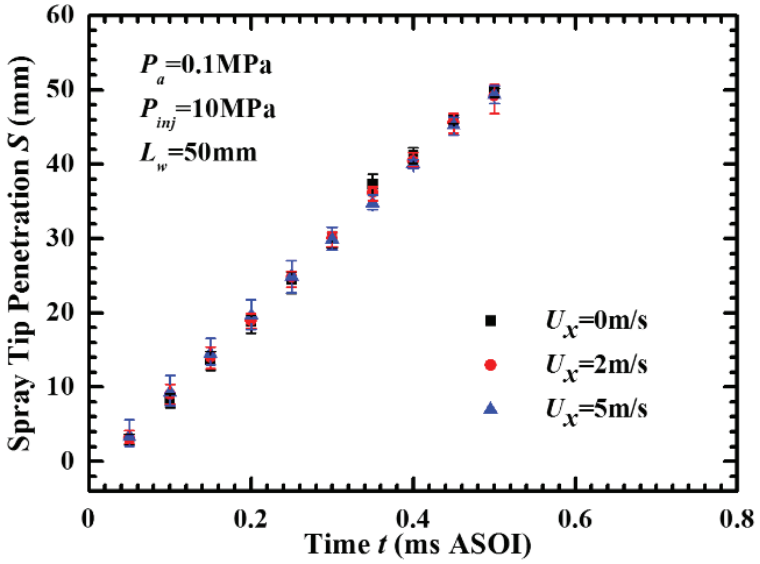

(a) P_a = 0.1 MPa

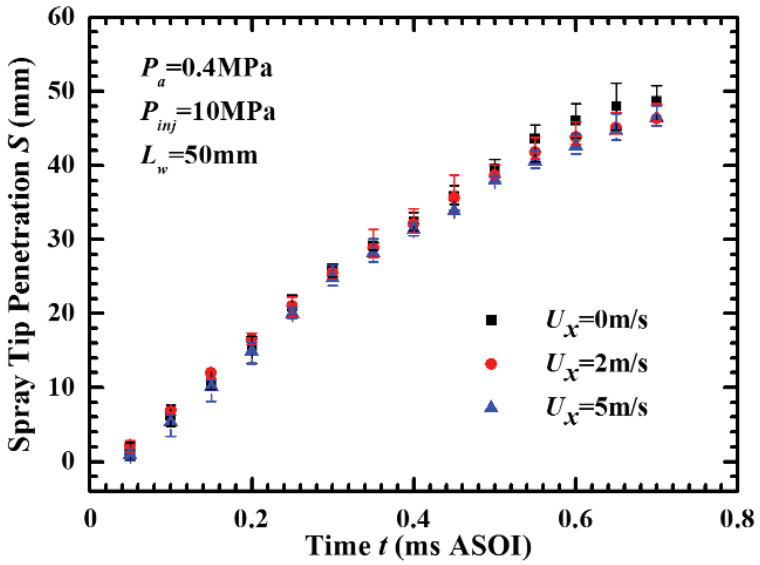

(b) P_a = 0.4 MPa

Figure 3.17 Effect of cross-flow velocities on spray tip penetration of early-stage.

To clarify the effect of cross-flow on the spray tip penetration before impingement, the penetration results of the early stage of spray evolution were shown in Figure 3.17. Under an ambient pressure of 0.1 MPa, the penetrations were almost the same before 0.35 ms ASOI, but after the 0.35 ms ASOI, the penetrations slightly decreased as cross-flow velocity increased. When ambient pressure is 0.4 MPa, increasing the cross-flow velocity evidently decreased the penetrations, especially after 0.5 ms ASOI. This is because the shear force increased with the increase in cross-flow, causing the breakup of spray tip then the vertical velocity of spray tip decreased. At higher ambient pressure, the increased momentum flux of cross-flow led to considerably severe breakup and larger momentum loss of the spray thus this phenomenon became substantially evident. The evidence based on the slip Weber numbers was provided to justify the statement. When ambient pressure is increased, the parameter of air density ρ increases and the spray column d increases due to larger spray angle under higher ambient pressure [81]. The parameter of velocity v and surface tension σ is constant. So the slip Weber number increases with the increase of ambient pressure. Therefore higher ambient pressure led to more severe breakup.

Increases in the cross-flow velocity tended to a larger vortex height in the cases of 0.1 and 0.4 MPa ambient pressures, as shown in Figure 3.18. The reason of this phenomenon maybe is that after cross-flow through the upstream side vortex and main spray body, its flow direction maybe produce fluctuation and become non-uniform in horizontal direction. Then the fluctuating

cross-flow in the downstream side influence the dispersion of vortex, resulting in the formation of a larger vortex shape. When the cross-flow velocity is fixed, the density of ambient air increases with the increase in ambient pressure, leading to an increased penetration resistance that in turn decreased the momentum of the impingement spray and so reduced the vortex height *H*. The splashing resistance also increased, and this inhibited the splashing of secondary droplets and thus further decreased the vortex height.

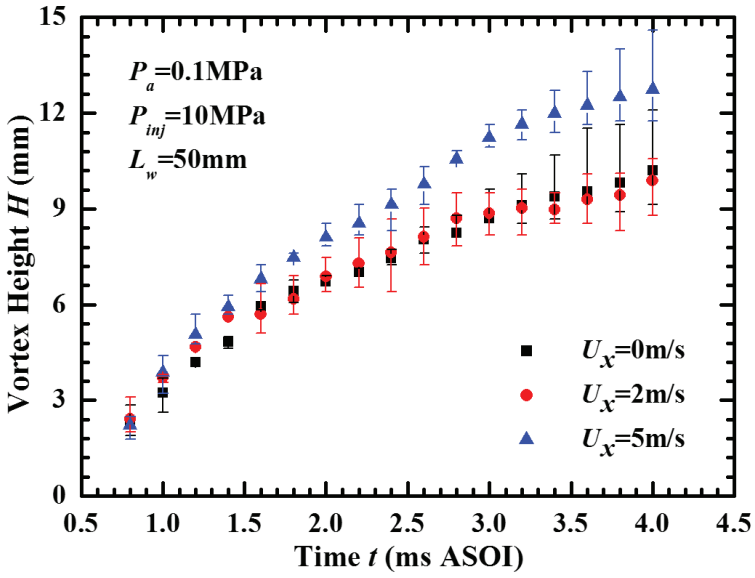

(a) P_a = 0.1 MPa

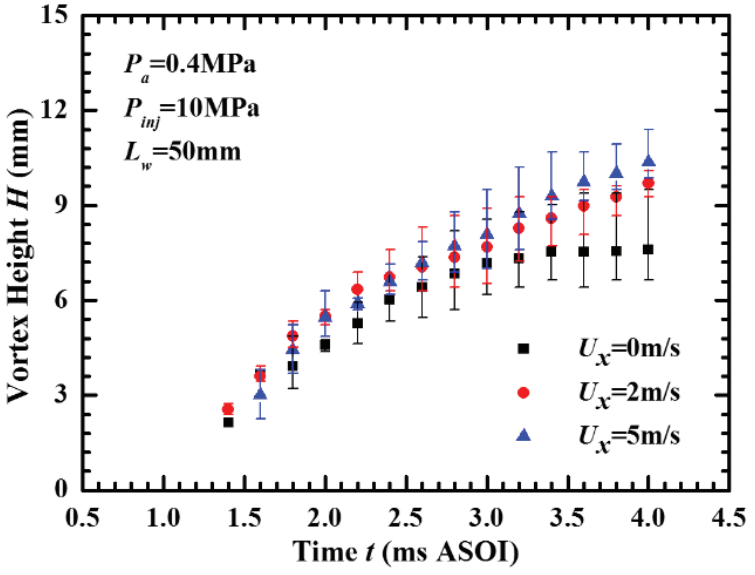

(b) P_a = 0.4 MPa

Figure 3.18 Comparisons of vortex height.

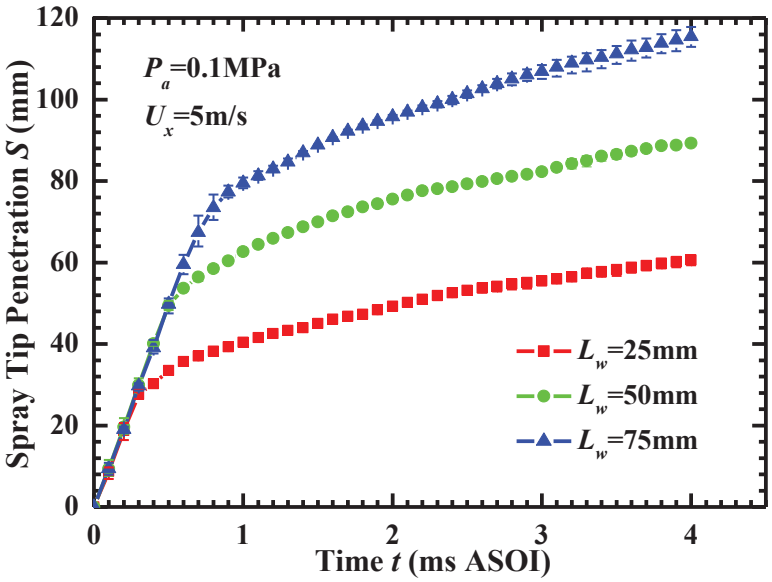

(a) Effect of impingement distance on spray tip penetration

(P_a = 0.1 MPa and U_x = 5 m/s)

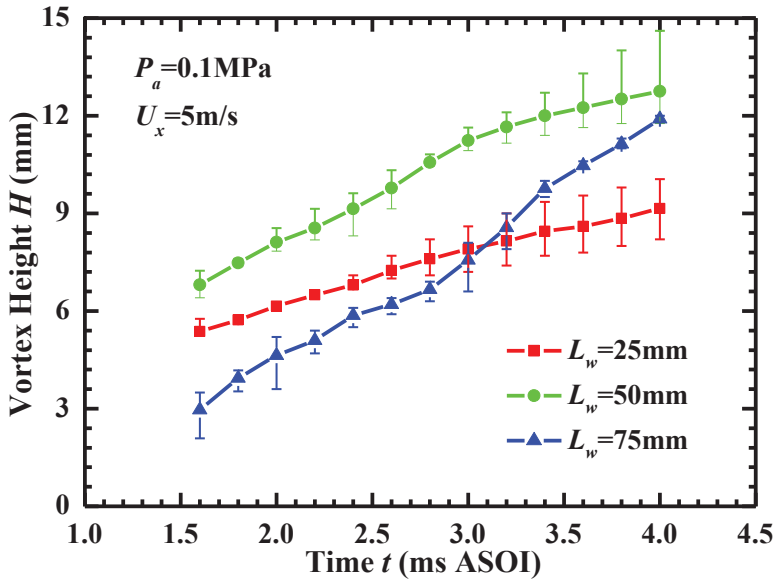

(b) Effect of impingement distance on vortex height

(P_a = 0.1 MPa and U_x = 5 m/s)

Figure 3.19 Effect of impingement distance on spray tip penetration and vortex height.

Figure 3.19 shows the effect of impingement distance on spray tip penetration and vortex height. As Figure 3.19-(a) shown, with increasing the impingement distance, the spray tip penetration was increased. This was attributed to late impingement under larger impingement distance, an effect that reduced the wall friction and thus increased *S*. Figure 3.19-(b) illustrates

the effect of impingement distance on spray vortex height H. It is noteworthy that at 50mm impingement distance the vortex height was maximum. At L_w=75mm case, the time required for the spray to impinge the wall was lengthened, which result in more of the injected spray being evaporated, then decreasing the mass of the impinged spray. However, for L_w=25mm case, larger radial velocity caused droplets separating from vortex, thus lowing the mass of the impinged spray.

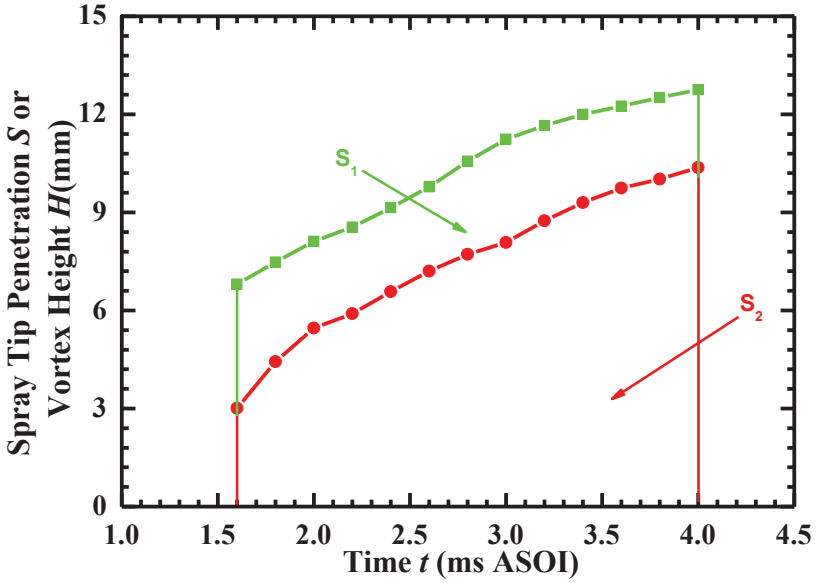

Figure 3.20 Definition of Contribution Index.

A Contribution Index was utilized to evaluate the contribution of each condition to the effects on the impingement spray characteristics (S and H). As shown in Figure 3.20, the area between the S or H curves and the horizontal axis were defined as S_1 and S_2, where S_1 is the area obtained while changing one variable, for example U_x = 5 m/s, while S_2 is the area acquired under the smaller value condition, for example U_x = 0 m/s. In each condition, the Contribution Index can be determined as follows:

$$\text{Contribution Index} = \left(1+\frac{S_1-S_2}{S_2}\right)\times 100\% \tag{3.5}$$

If the value of the Contribution Index is larger than 100%, S or H is increased, while this index smaller than 100% stands for a decrease.

The contribution of each environmental condition to the spray tip penetration variation is provided in Figure 3.21-(a). The Contribution Index values associated with changes in the impingement distance are evidently greater than cross-flow velocity and ambient pressure. The contributions of cross-flow velocity is the smallest but also significant effect. Figure 3.21-(b)

shows the contribution of each case to the vortex height variation. In contrast to the *S* data, the contributions of impingement distance is less obvious, with each variable having a similar level of effect. With the increase of impingement distance the Contribution Index value increase firstly and then decrease.

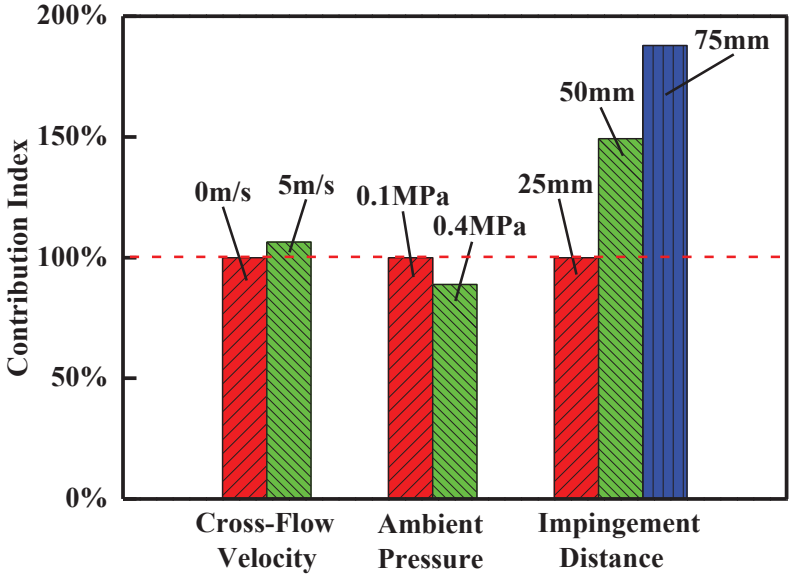

(a) Contribution Index to spray tip penetration *S*

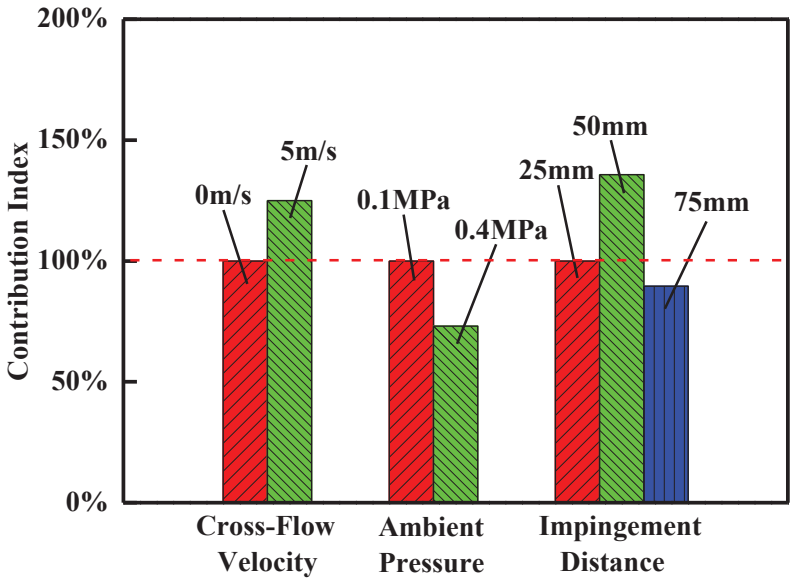

(b) Contribution Index to spray vortex height *H*

Figure 3.21 Contribution Index of each condition to *S* and *H*.

3.5 Summary

At the early period of injection by the VCO nozzle, two asymmetric spray tips will be seen because of the special geometric structure of the VCO type nozzle.

With increasing the velocity of the cross-flow, numerous tiny droplets were entrained and shifted downstream, indicating that the cross-flow favors the spray profile dispersion. The droplets distribution presents inhomogeneous at the downstream region of spray. The quantitative analysis shows that with increasing cross-flow velocity, the spray tip penetration decreases slightly before impingement while the spray tip penetrates further on the wall surface after impingement. The high cross-flow velocity favors the spray breakup and dispersion, leading to a larger wall-jet vortex. High ambient pressure restrains the spray dispersion and leads to smaller spray tip penetration and vortex height. With increasing impingement distance, the spray tip penetration is increased. However, for the spray vortex height, the maximum value presents at 50mm impingement distance.

Under an approximate liquid-to-air momentum flux ratio q, when the ambient pressure and cross-flow velocity were varied, at 2 ms ASOI the outlines of the spray in the windward side agree well, whereas the spray extended further in the leeward side at a lower ambient pressure.

Chapter 4 Impingement Spray Structures in Horizontal Planes

In the current study, to promote the understanding of the three dimensional spray structure, the influences of the ambient pressure and cross-flow velocity on spray structure in horizontal planes have been experimentally investigated. It is not enough to only study the spray structure in vertical plane. With cross-flow, the movement of droplets in the spray presents complex phenomenon. To further study the structure and movement of the impingement spray, spray images in several horizontal planes were captured using a laser-sheet imaging technique.

4.1 Experimental Condition and Cross-sectional Locations

4.1.1 Experimental condition

Table 4.1 Experimental conditions

Injection Conditions	
Injector Type	VCO, Single-hole
Hole Diameter : d (mm)	0.15
Injection Mass : Q_{inj} (mg)	4.36
Injection Duration : T_d (ms)	4
Injection Pressure : P_{inj} (MPa)	10
Ambient Condition	
Ambient Gas	Air
Ambient Pressure : P_a (MPa)	0.1, 0.4
Ambient Temperature : T_a (K)	293
Cross-flow Velocity : U_x (m/s)	5, 10
Cross-sectional Locations : y (mm)	25, 42, 45, 48
Impingement Distance : L_w (mm)	50

The detailed experimental conditions are listed in Table 4.1. Dry-solvent was utilized as a test fuel in this study. The injection duration was 4 ms and the impingement distance L_w was 50 mm under the cross-flow velocities of 5 m/s and 10 m/s. The injection pressure was 10 MPa and the ambient pressure varied between 0.1 and 0.4 MPa. The measurement at every condition was repeated three times.

4.1.2 Cross-sectional locations

Under cross-flow condition, the spray characteristics including the spray profiles, spray tip penetration and spray vortex height have been discussed in Chapter 3. Some phenomena, such as the non-uniform distribution of droplets at the leeward upper region of the spray, are difficult

to comprehend merely by analyzing the impingement spray behavior in the vertical plane due to the asymmetric structure of the impingement spray. To clarify the spray structure in three-dimensional space, spray images in horizontal plane were obtained by the laser sheet and a high speed video camera. The figure of the experimental apparatus as shown in Figure 2.10-(b). Figure 4.1 shows the cross-sectional locations of observation. In the middle part of spray the images were taken in the horizontal plane of y = 25 mm. And near the wall region the images were taken in 3 mm intervals (from y = 42 mm to y = 48 mm).

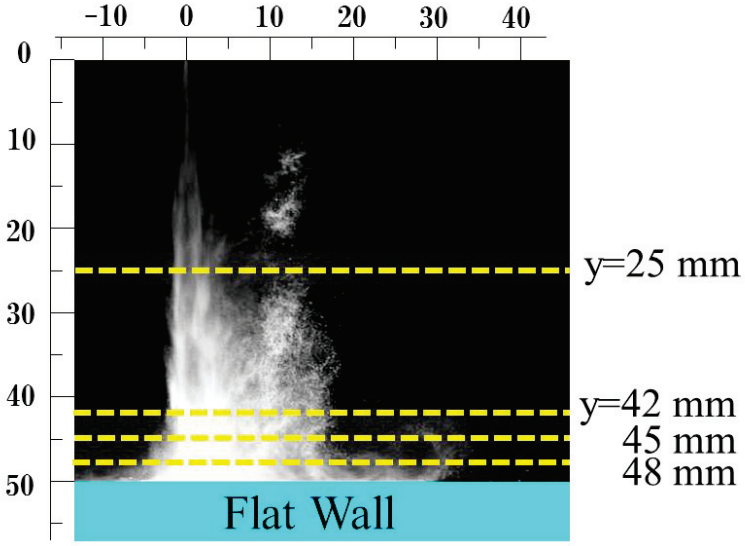

Figure 4.1 Cross-sectional locations of observation

4.2 Spray Details and Vortex Phenomenon

4.2.1 Spray details in horizontal planes

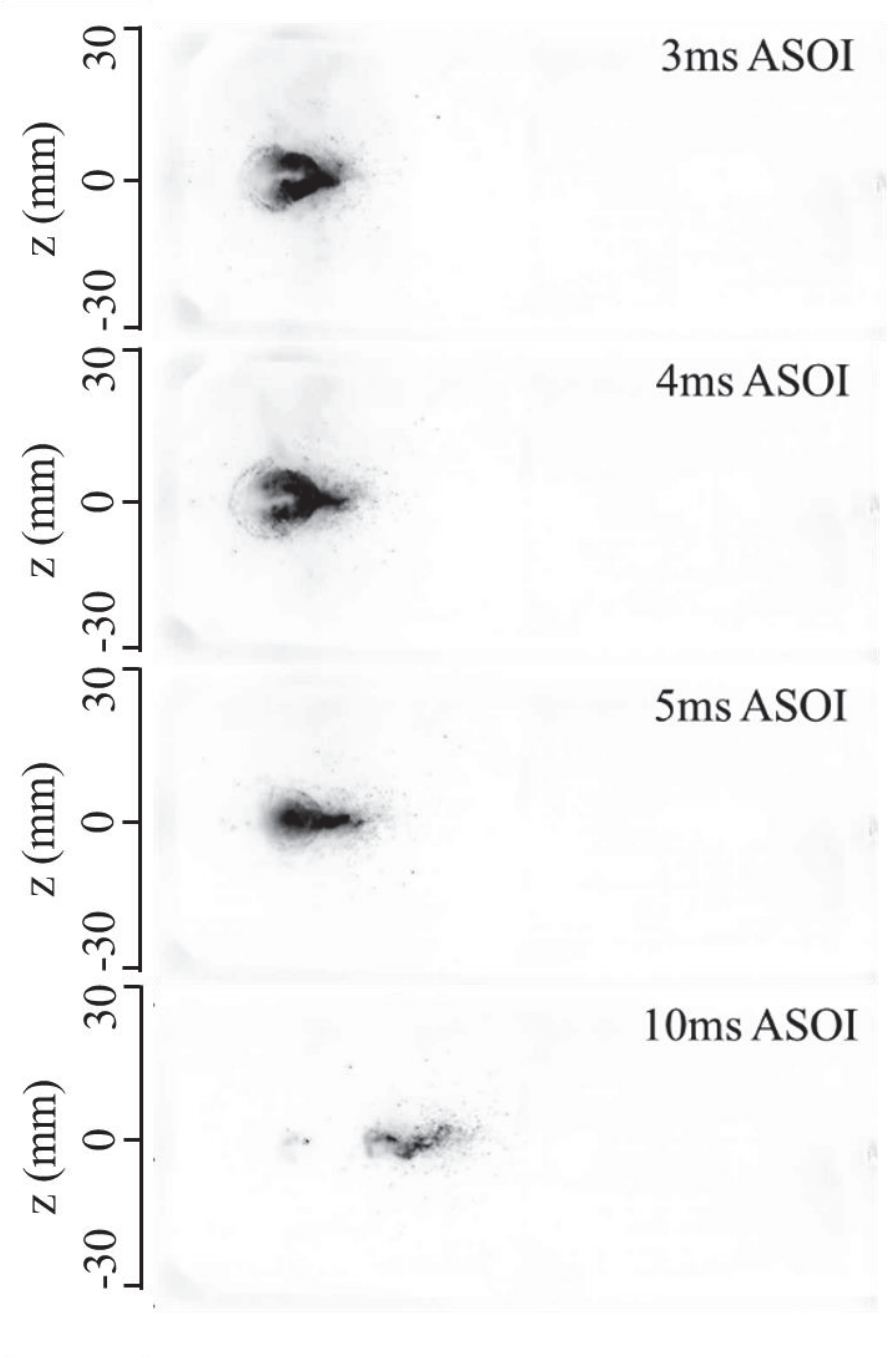

(a) Pa = 0.1 MPa, U_x = 5 m/s

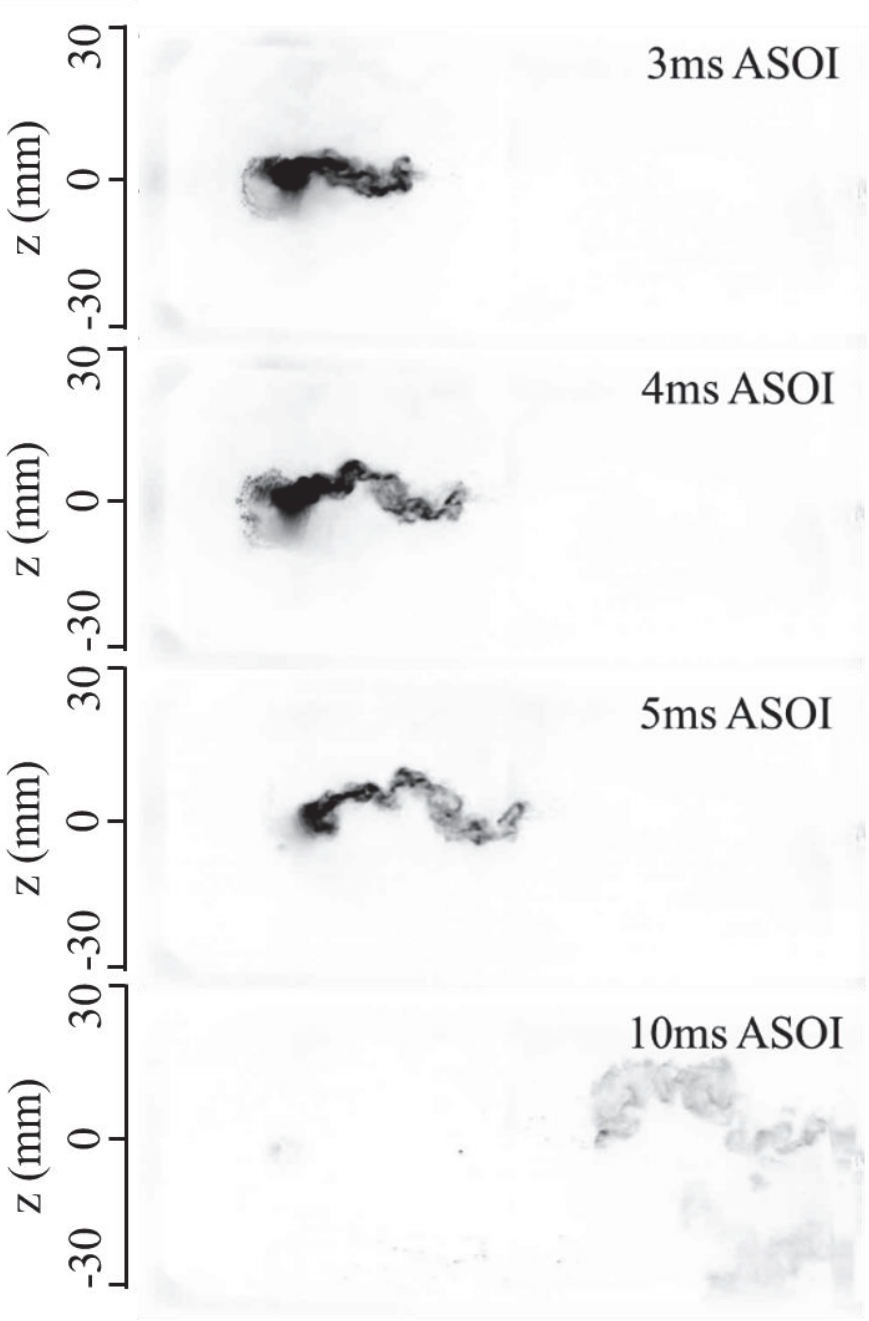

(b) Pa = 0.1 MPa, U_x = 10 m/s

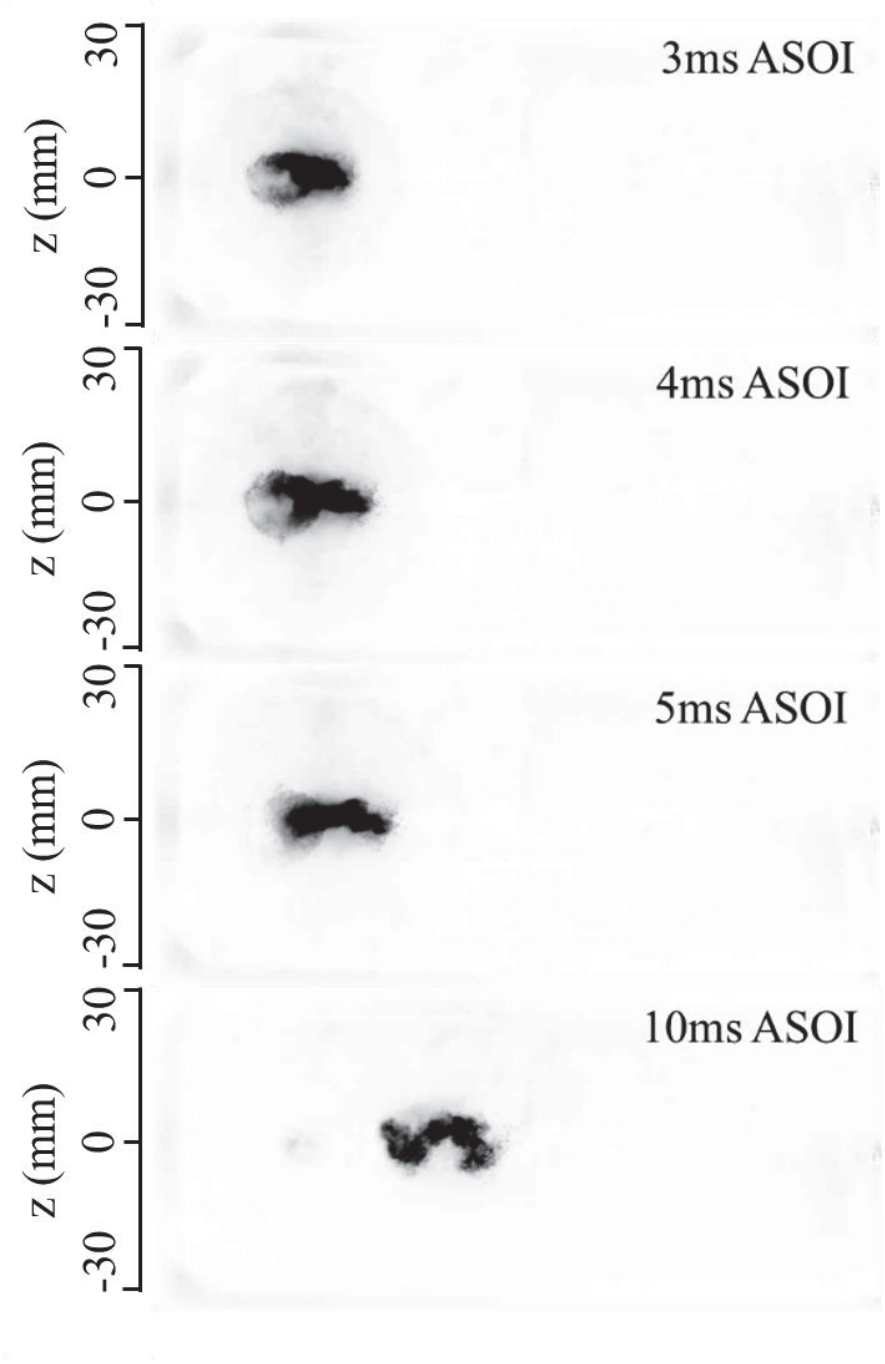

(c) Pa = 0.4 MPa, U_x = 5 m/s

Figure 4.2 Effects of cross-flow velocity and ambient pressure on impingement spray structures in horizontal plane of y = 25 mm

The horizontal images in the plane of y =25 mm are listed from 3 ms ASOI to 10 ms ASOI in Figure 4.2. During the injection period, fuel film can be seen near the nozzle hole position, leading to the upstream spray structure is slightly ambiguous. However, the main spray structures are clearly represented in this Figure. Figure 4.2-(b) shows the spray movement in the horizontal plane under 10 m/s cross-flow condition. At the time of 3 ms ASOI, the spray structures in the windward side present a knot structure according to the intensity of the image; however, the spray structures in the leeward side become unstable. From 3 ms ASOI to 4 ms ASOI, the structures of the spray changed greatly. The profiles became asymmetrical in the downstream region and the main spray structure became thinner. The spray diffusion in the downstream region was promoted with the time going. Some fluctuations in the spray appeared along the cross-flow direction, seeming like a movement of vortex. This wave structure was a little similar to that of the Karman vortex street [82]. The reason of this phenomenon formation will be introduced in the chapter of 4.2.2. With the time going, the spray profiles penetrated further in the horizontal plan. After 4 ms ASOI, the spray profile was out and away from the nozzle hole position.

Compared with the Figure 4.2-(a), the spray penetration in the horizontal plane is longer at the same time in Figure 4.2-(b). It indicates that the effect of cross-flow on spray profiles is promoting the diffusion in the downstream region. In addition, the adverse effect of fuel film on the horizontal spray observation became weakened with the increase of cross-flow velocity. This maybe because that the fuel film flow to downstream region and become more dispersed under higher cross-flow condition. It is worth noting that with increasing the cross-flow velocity, the fluctuation of spray structure became more obvious because the higher momentum of cross-flow is more easily lead to fluctuation of the liquid flow.

Compared Figure 4.2-(a) with Figure 4.2-(c), we found that with the increase of ambient pressure, the spray density is increased in these images and the spray fluctuation becomes more severe. Especially at the time of 10 ms ASOI, the shape of spray structure seemed like the letter S. This is because at higher ambient pressure, the momentum flux of cross-flow is increased, leading to a considerably severe spray fluctuation.

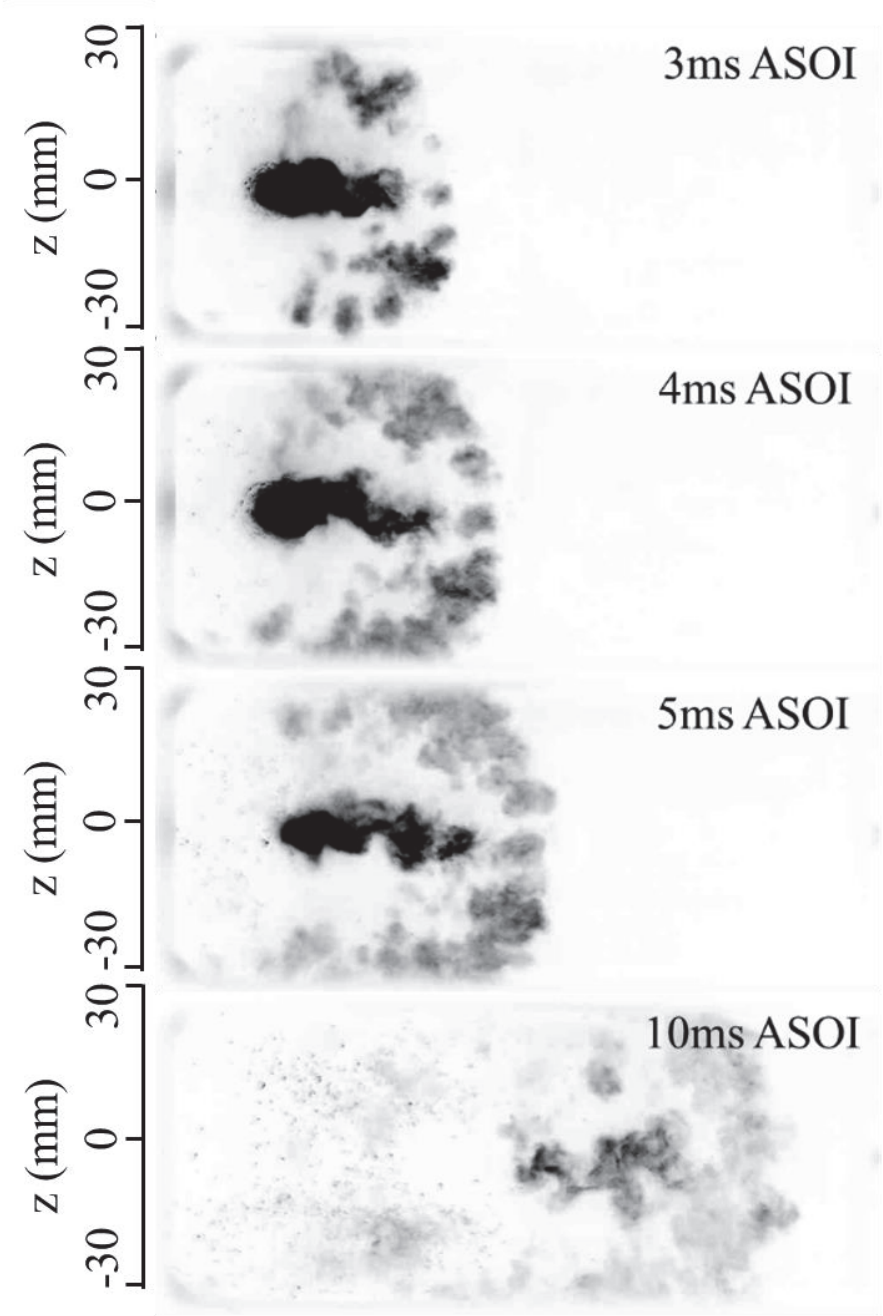

(a) y = 42 mm

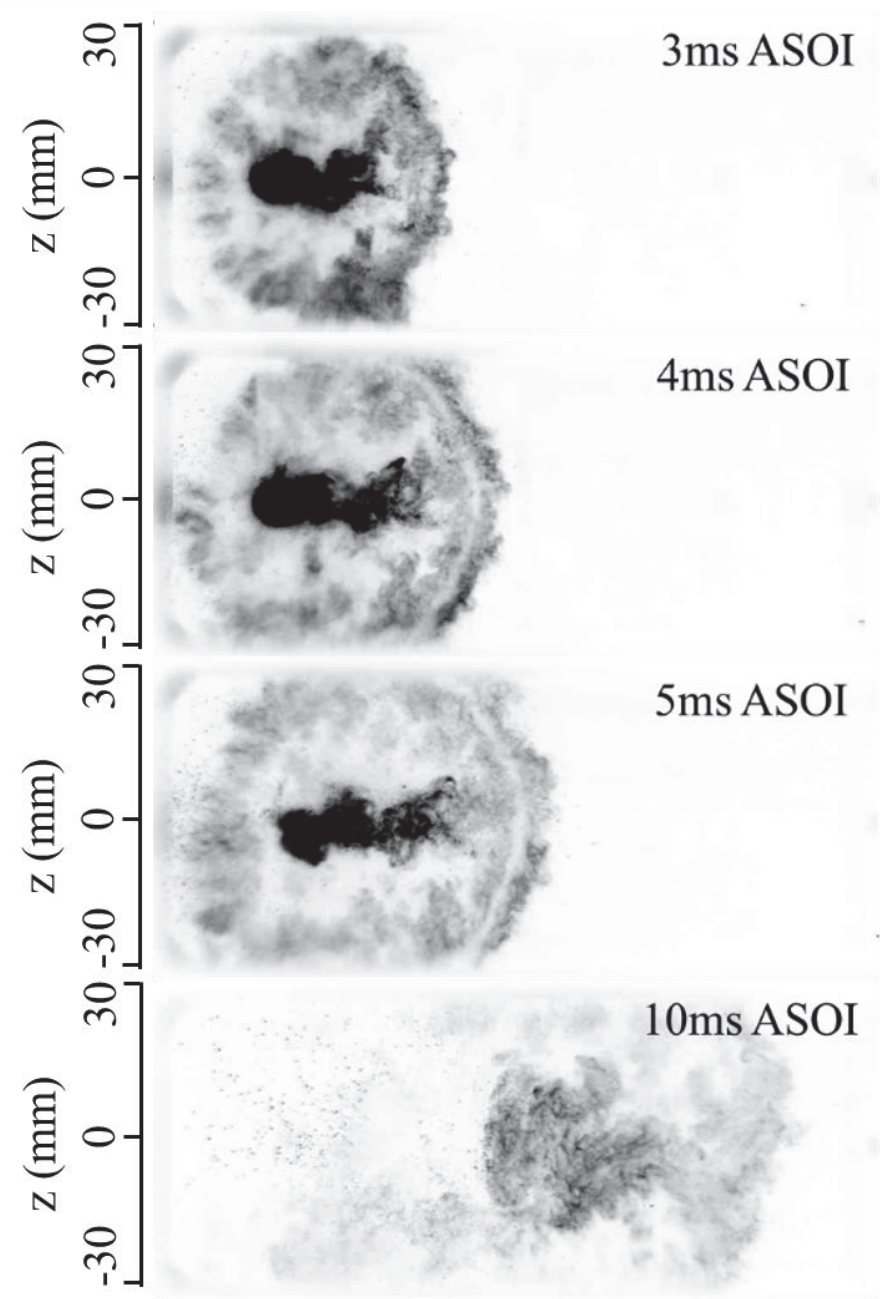

(b) y = 45 mm

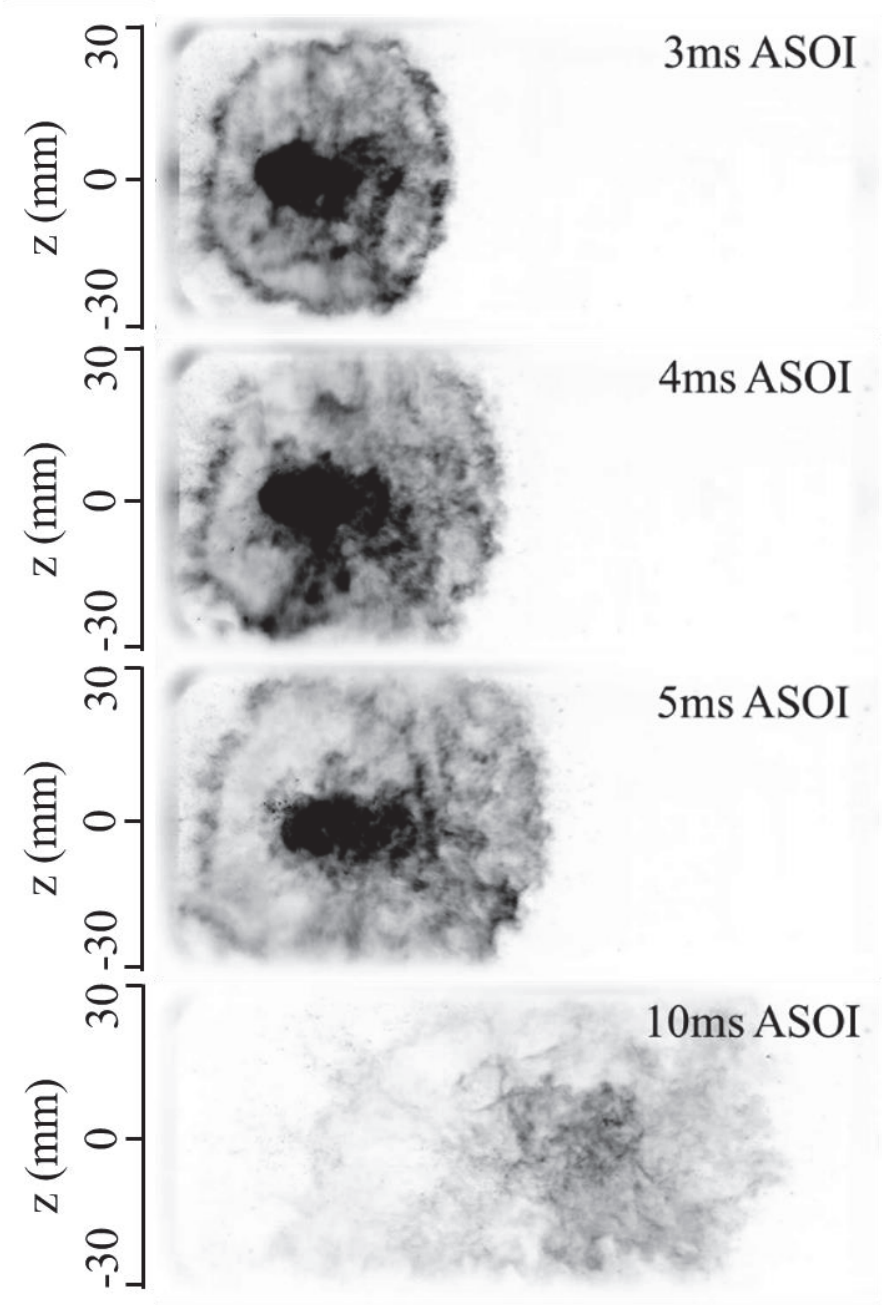

(c) y = 48 mm

Figure 4.3 Near-wall impingement spray structures in horizontal planes (Pa = 0.1 MPa, U_x = 10 m/s)

Near the wall spray movement in the horizontal plane became more complex because of the wall-jet vortex, the detailed images are needed in this region. Figure 4.3 gives the spray profiles in the horizontal planes of y = 42 mm, 45 mm and 48 mm at the ambient pressure of 0.1 MPa and cross-flow velocity of 10 m/s. In each horizontal plane, with the time going the spray structures showed a tendency of diffusing, resulting in the area of spray structures increasing. There is an obvious phenomenon that before 5 ms ASOI, the outlines of main spray structures were very clearly; however, at 10 ms ASOI, the main spray structures disappeared in the horizontal planes. This is because after the end of injection, the droplets are decelerated with the effect of ambient air friction. Then the droplets are more easily entrained by cross-flow, leading to more obviously diffused structures in the downstream region.

For the main spray structures, the spray profiles in the upstream side seemed like ellipses, and the droplets concentrated in this region. However, in the downstream side, some fluctuations liking wave structures in the horizontal plane of y = 25 mm could be observed and the structures fluctuated along the direction of the cross-flow. With decreasing the distance from the wall surface, the fluctuation phenomenon became weak in the downstream region. Especially for the spray structure in the plane of y = 48 mm shown in the Figure 4.3-(c), the fluctuation structure almost disappeared. The reason is that with the increase of the distance from the nozzle hole, the extent of spray breakup increased, forming smaller droplets. When a fluid flows past a diffused spray body, the fluctuation phenomenon is difficult formed around the spray body.

It is worth noting that with decreasing the distance from the wall surface, the vacant region between the main spray body and the wall-jet vortex was decreased. Because the wall-jet is closer with the horizontal observation plane at a decreased distance from the wall surface. In addition, we found that almost no droplets distributed in the vortex core region in the horizontal of y = 45 mm shown in Figure 4.3-(c).

4.2.2 Vortex phenomenon in cross-flow

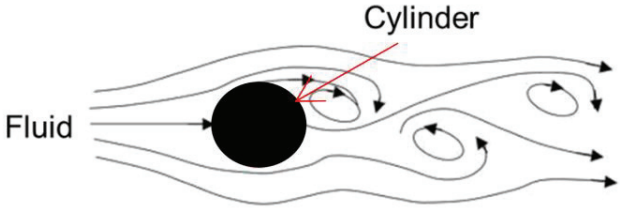

Figure 4.4 Formation of the vortex street.

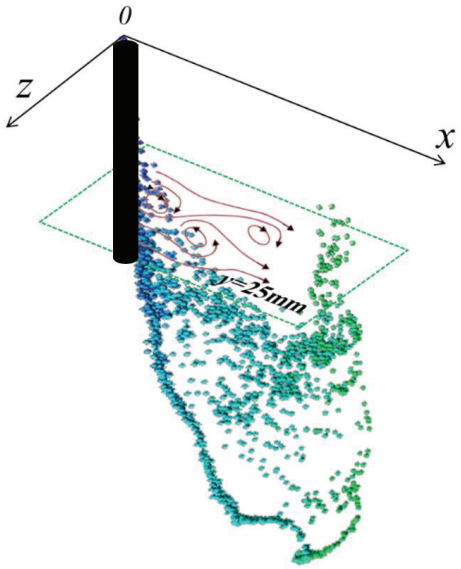

Figure 4.5 Spray movement in the downstream region of cross-flow (y = 25 mm).

Theodore Von Karman proposed the vortex street phenomenon in 1911. When a fluid flows past a blunt body, an unstable boundary layer separation in the fluid will happen. The fluctuation phenomenon is dependent on the body shape, fluid direction and fluid velocity. When a fluid passes through a cylinder with an appropriate Reynolds number, the phenomenon of the vortex street is always formed, as shown in Figure 4.4.

At the impingement distance of 50 mm, in the middle prat of the impingement spray, most droplets with large vertical momentum concentrated around the axis line of the nozzle hole. If the Reynolds number is appropriate, when the cross-flow passes through the spray body, which seems like a solid cylinder in the horizontal plane of y = 25 mm, the vortex street phenomenon could be seen, as shown in Figure 4.5.

At the horizontal plane of y = 25 mm, the spray structure distributed asymmetry and fluctuation phenomenon happened in the downstream region of cross-flow. The spray movement in the horizontal plane is similar to that of Karman vortex. In our previous research, the vortex frequency and wavelength have been investigated.

4.3 Three Dimensional Spray Structure

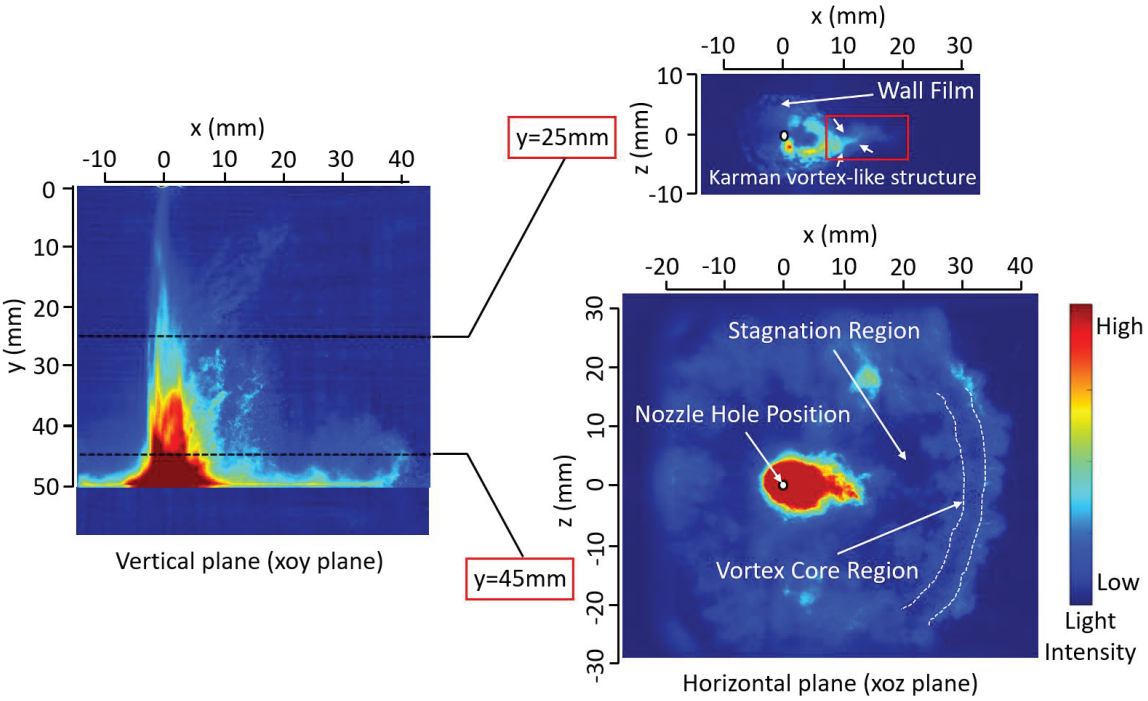

Figure 4.6 Spray profiles in a vertical plane and two horizontal planes at P_a=0.1MPa, U_x=5m/s, t=4ms ASOI.

Under cross-flow condition, some phenomena, such as the non-uniform distribution of droplets at the leeward upper region of the spray, are difficult to comprehend merely by analyzing the impingement spray behavior in the vertical plane due to the asymmetric structure of the impingement spray. To clarify the spray structure in three-dimensional space, spray images in a vertical plane of z = 0 mm and its corresponding images at horizontal planes of y = 25 and 45 mm at P_a=0.1MPa, U_x=5m/s, t=4ms ASOI were shown in Figure 4.6. In the right image, a wave-shaped structure was observed in the horizontal plane of y = 25 mm marked by a red rectangle. The structure resembled a vortex motion, and the wave shape was almost similar to the Karman vortex street [82]. The arrows in the image are employed to indicate the fluctuation of the Karman vortex-like structure. In this region, although the wall film was not on the laser sheet plane, it still influenced the observation of the Karman vortex-like structure, leading hard to distinguish the boundary of Karman vortex-like structure. The structure of the main spray in the plane of y = 45 mm was shaped like a fish. The spray upstream region was dense and wide, but downstream, the spray became thin and narrow. This is because the spray in downstream was formed by tiny

droplets entrained by cross-flow that flowed downstream. It is noted that almost no droplets were present in the stagnation region in this plane and an empty belt was observed near the vortex core region, which indicates that the droplet density in this region was quite low.

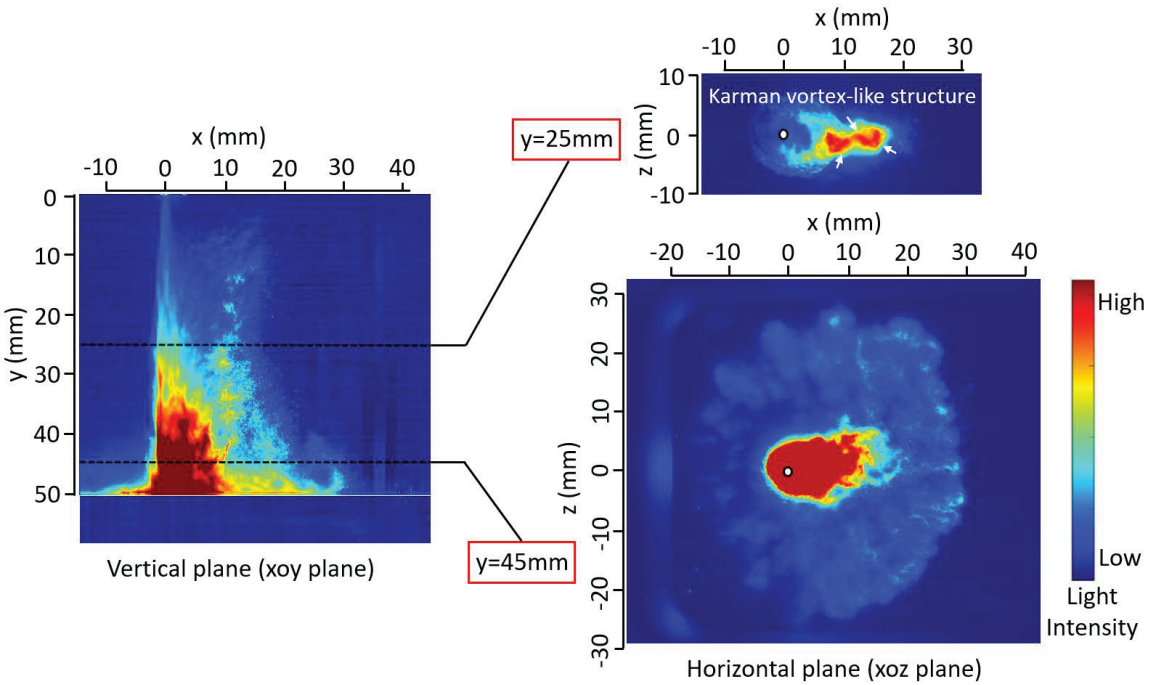

Figure 4.7 Spray profiles in a vertical plane and two horizontal planes at P_a=0.4MPa, U_x=5m/s, t=4ms ASOI.

At a higher ambient pressure, as shown in Figure 4.7, the phenomenon of the Karman vortex-like structure became considerably evident in the plane of y = 25 mm. This is because the cross-flow with larger momentum flux caused a considerably severe spray fluctuation. The stagnation region in the plane of y = 45 mm was smaller than that under atmospheric pressure and the wall-jet vortex was caught up by the droplet cloud entrained by cross-flow. It could be comprehended that the whole vortex structure penetrated more slowly along the wall due to the larger air resistance under high ambient pressure. Moreover, the larger momentum flux induced a considerably severe spray breakup; thus, more droplets were entrained and shifted downstream. In this case, the phenomenon of the empty belt in the vortex core region disappeared. The reason is that the position of the vortex core was below the plane of y = 45 mm.

4.4 Summary

To clarify the spray structure in three-dimensional space, spray images in horizontal planes were obtained by the laser sheet and a high speed video camera. In the middle part of spray the images were taken in the horizontal plane of y = 25mm. And near the wall region the images were taken in 3 mm intervals (from y = 42 mm to y = 48 mm).

The fluctuation of the main spray structure became more obvious with increasing the cross-flow velocity, because the higher momentum of cross-flow is more easily lead to fluctuation of the liquid flow. In addition, with the increase of ambient pressure, the spray density is increased in these images and the spray fluctuation becomes more severe.

Near the wall region, with decreasing the distance from the wall surface, the fluctuation phenomenon became weak in the downstream region. It is worth noting that with decreasing the distance from the wall surface, the vacant region between the main spray body and the wall-jet vortex was decreased.

At the plane of y = 25 mm, a complex vortex movement was observed that resulted in a non-uniform distribution of droplets in the upper part of the spray in the leeward side. In addition, at the plane of y = 45 mm, an empty belt area occurred in the vortex core region revealing that the density of the droplets in this region was quite low.

Chapter 5 Droplet Size and Velocity Distribution of Impingement Spray

The droplet number and SMD distribution represent the quality of spray and atomization. And they affect the subsequent combustion and emissions in engines. Moreover, the droplet velocity distribution affects the spray structure and the breakup process. In this chapter PIA optical diagnostic method was utilized to obtain the droplet images of local spray. The droplet size and velocity distribution of local spray were measured in various locations under cross-flow conditions. The droplets flow field distribution in the vertical plane were measured by PIV optical diagnostic method. The droplet velocity distribution in the wall-jet vortex will be discussed in this part.

5.1 Experimental Condition and Measurement Locations

5.1.1 Experimental condition

Table 5.1 Experimental conditions

Injection Conditions		
Experiment	PIA	PIV
Injector Type	VCO, Single-hole	VCO, Single-hole
Hole Diameter : d (mm)	0.15	0.15
Injection Mass : Q_{inj} (mg)	4.36	4.36
Injection Duration : T_d (ms)	4	4
Injection Pressure : P_{inj} (MPa)	10	10
Ambient Condition		
Ambient Gas	Air	Air
Ambient Pressure : P_a (MPa)	0.1	0.1
Ambient Temperature : T_a (K)	293	293
Cross-flow Velocity : U_x (m/s)	5, 10	0, 5, 10
Impingement Distance : L_w (mm)	50	50
Measurement Time : (ms ASOI)	4	3, 4

The detailed experimental conditions are listed in Table 5.1. Dry-solvent was utilized as a test fuel in this study, and the impingement distance L_w was 50 mm. The ambient pressure was 0.1 MPa and the injection pressure was 10 MPa. The PIA experiment was conducted at the time of 4 ms ASOI under the cross-flow velocities of 5 m/s and 10 m/s. For the PIV experiment, the measurement time were 3 and 4 ms ASOI, and the cross-flow velocities were 0, 5 and 10 m/s. The measurement at every condition was repeated three times.

5.1.2 Measurement locations of PIA experiment

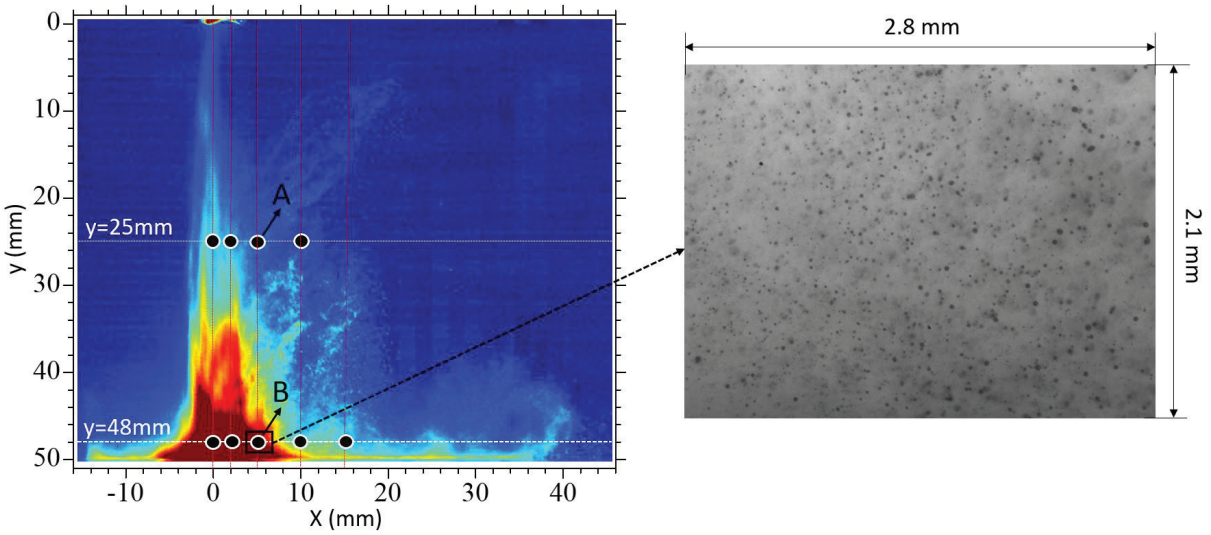

(a) U_x = 5 m/s

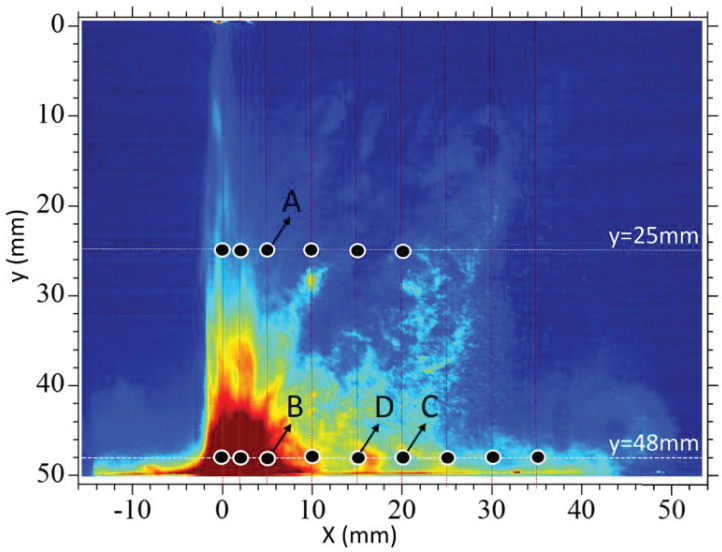

(b) U_x = 10 m/s

Figure 5.1 Measurement locations of PIA experiment at t = 4 ms ASOI (A: x = 5 mm, y = 25 mm; B: x = 5 mm, y = 48 mm; C: x = 20 mm, y = 48 mm; D: x = 10 mm, y = 48 mm)

In the PIA experiment investigation, the quiescence case was not selected because of the smaller spray area, resulting in a smaller measurement region. To study the effect of cross-flow on the droplet diameter and velocity, two cases of 5 m/s and 10m/s cross-flows were selected, and the measurement locations are shown in Figure 5.1. The locations in y = 25 mm and 48 mm lines were selected, which were in the middle and bottom of the impinging spray, respectively. The details of

the droplet diameter and velocity at regions A, B and C were extracted to compare the microscopic characteristics in different locations. The center coordinates of regions A, B and C are (x = 5 mm, y = 25 mm), (x = 5 mm, y = 48 mm) and (x = 20 mm, y = 48 mm), respectively.

The detailed droplet detection procedure has been reported previously [83], and a brief description is given here. Twenty injection events were recorded and no less than 8000 droplets were detected for each condition. Refined criteria were used to detect the droplets correctly. The threshold value of the pixel intensity was set at 20 out of 255 (8% of the maximum pixel intensity), and all pixels in the image whose intensities are above the threshold value can be detected. In this study, the field of view was 2.8 mm × 2.1 mm with a resolution of 1.75 μm/pixel. The droplets with pixel numbers less than 5 were rejected, and the roundness of droplets was set from 80 to 100.

5.2 Droplet Number/size Distribution

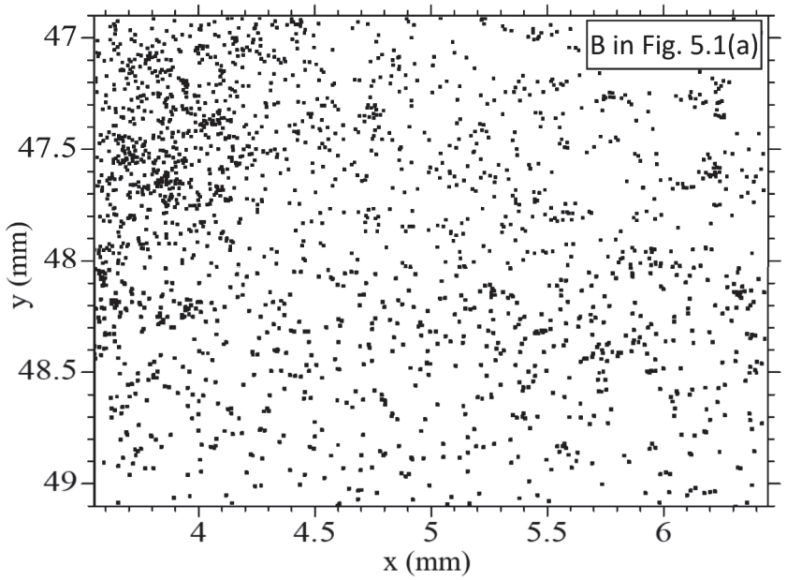

(a) U_x = 5 m/s, x = 5 mm, y = 48 mm

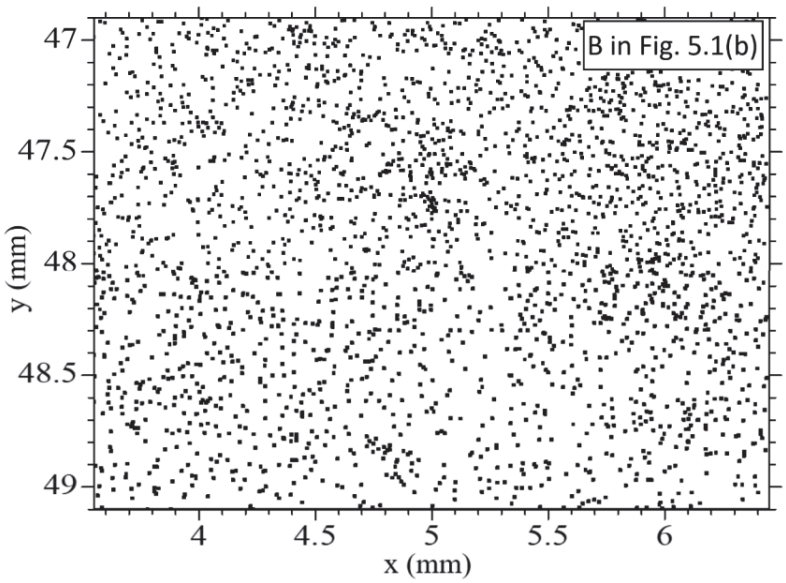

(b) U_x = 10 m/s, x = 5 mm, y = 48 mm

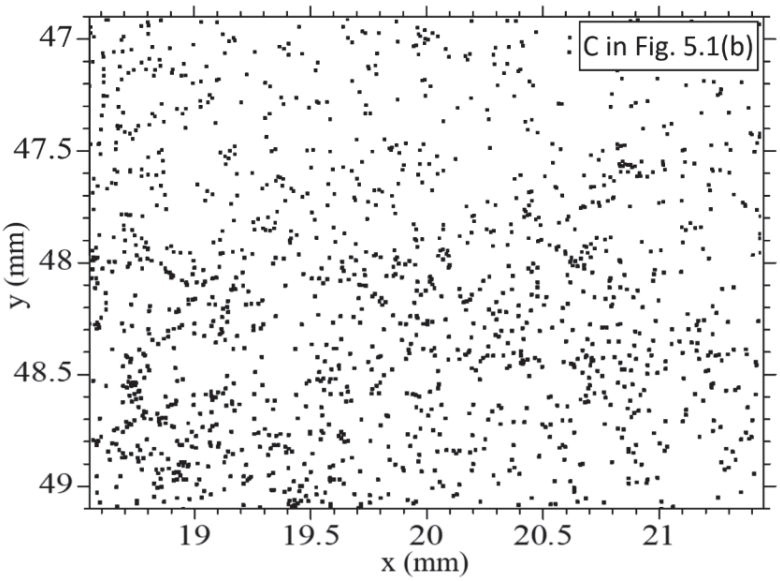

(c) U_x = 10 m/s, x = 20 mm, y = 48 mm

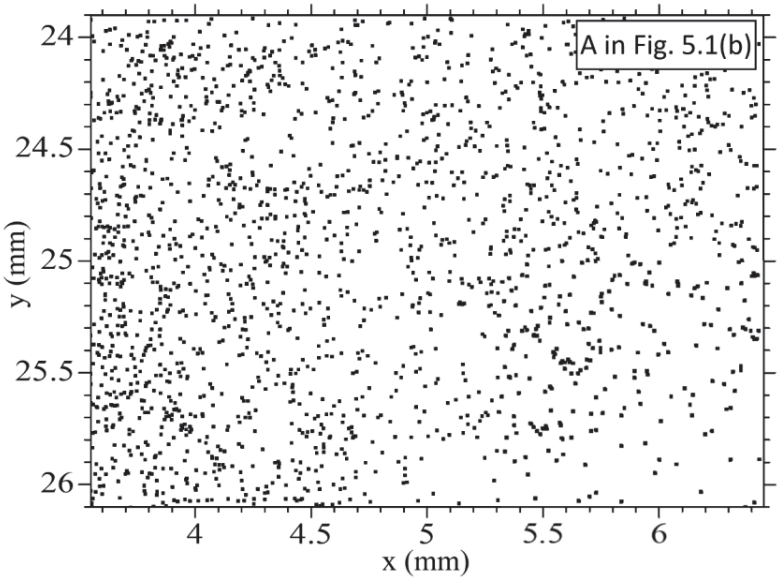

(d) U_x = 10 m/s, x = 5 mm, y = 25 mm

Figure 5.2 Droplets assembly for regions A, B and C

Figure 5.2 shows the detected droplets summation of five injection events in four different regions. The black spots represent the droplets. As shown in Figure 5.2-(a), droplets tend to aggregate on the left half of region B at 5 m/s cross-flow, indicating the decrease in number of droplets from the spray center to the spray periphery, and the left half of region B is closer to the spray center. By comparison with Figure 5.2-(b), it is evident that with increasing the cross-flow

velocity, the spray center shifts to the downstream side. By comparing Figure 5.2-(b) and Figure 5.2-(c), it was found that at the downstream region of x = 20 mm, most droplets were closer to the wall surface than to the upper part, implying that these droplets are mainly derived from the splash and secondary breakup. Additionally, by comparing Figure 5.2-(b) and Figure 5.2-(d), we observed that the number of droplets was larger at the bottom of the impinging spray, indicating that region B is closer to the spray center and in cross-flow when the spray moved from the middle region to the bottom region the spray center shifts to the downstream side.

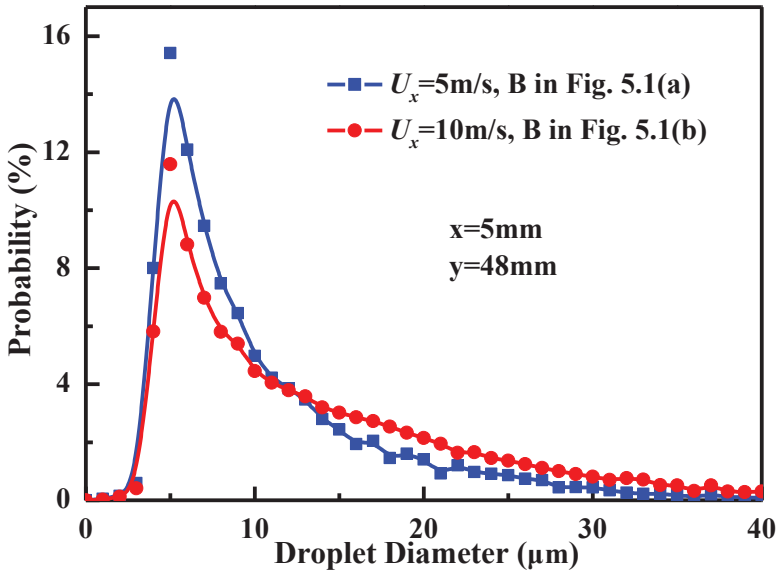

(a) Effect of cross-flow velocity

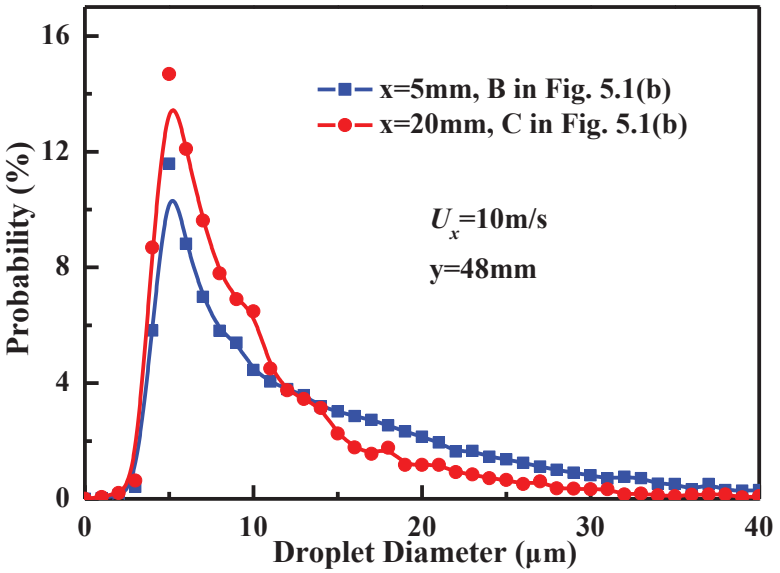

(b) Effect of radial distance

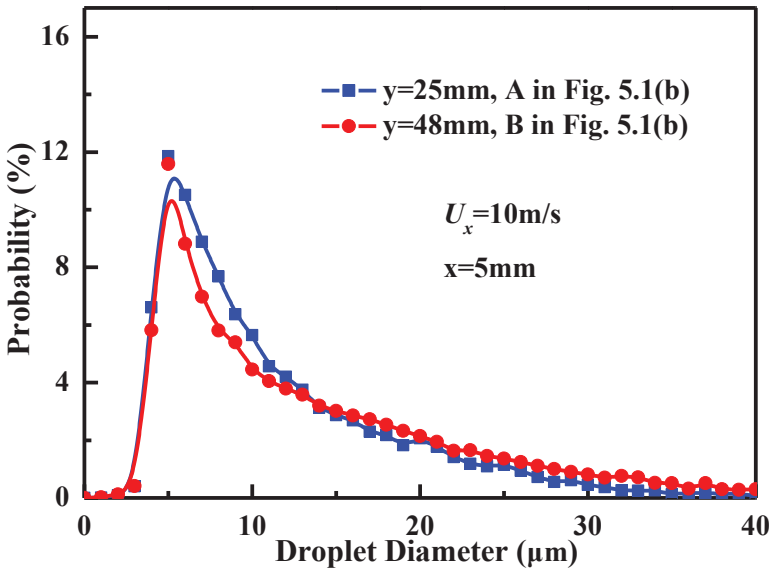

(c) Effect of axial distance

Figure 5.3 Droplet size distribution at (a) Cross-flow velocities of 5 m/s and 10 m/s, (b) Radial distances of 5 mm and 20 mm, (c) Axial distances of 25 mm and 48 mm.

From Figure 5.3 to Figure 5.13, the results were based on the data of twenty injections, except the five injection results of Figure 5.5. Figure 5.3 shows the droplet diameter distribution probability for (a) different cross-flow velocities, (b) different radial locations and (c) different axial locations. For a given location (x = 5 mm, y = 48 mm), with increasing the cross-flow velocity the number fraction of smaller droplet decreases, while the number fraction of larger droplet increases, as shown in Figure 5.3-(a). Additionally, although the droplet diameter corresponding to the peak value under different cross-flow velocities is similar (6 μm), the peak value decreases with the increase in cross-flow velocity. The reason is that in this region the droplets had large vertical momentum, and only small droplets could be entrained by cross-flow. As the cross-flow velocity increases, the number of small droplets entrained by cross-flow increased, which resulted in a smaller peak value in a higher cross-flow velocity. As shown in Figure 5.3-(b), with the increase in the radial distance, the peak value of the number fraction increased. This reveals that the droplet diameter distribution in the region of x = 5 mm is more scattered than that in the region of x = 20 mm. This could be attributed to the splash and coalescence phenomenon appearing in the x = 5 mm region, resulting in smaller and larger droplet formations, respectively. However, the probability of small droplets is significantly higher in the x = 20 mm region owing to the cross-flow entrainment. From the comparison between two axial locations shown in Figure 5.3-(c), we

found that with decreasing the axial distance from the wall, the number fraction of smaller droplets decreases while the number fraction of larger droplets increases slightly. Consequently, in the x = 5 mm line, the total average droplet size increases with the decrease in the axial distance from the wall, as shown in Figure 5.4-(b).

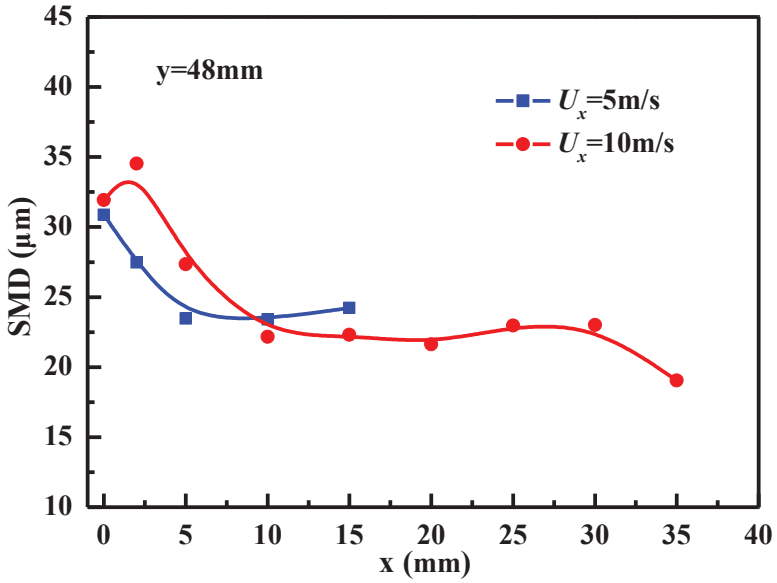

(a) Effect of cross-flow velocity

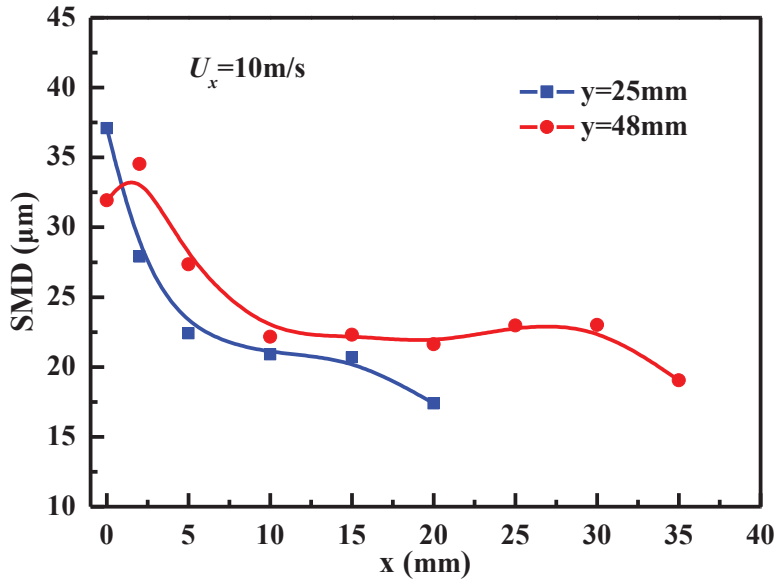

(b) Effect of axial distance

Figure 5.4 SMD distributions along x direction.

Generally, the Sauter mean diameter (SMD) is used to estimate the spray atomization, calculated with the following formula:

$$SMD = \frac{\sum_{i=1}^{k} n_i D_i^3}{\sum_{i=1}^{k} n_i D_i^2} \tag{5.1}$$

where k is the number of diameter clustering, n_i is the droplet number, and D_i is the droplet diameter. Figure 5.4-(a) and Figure 5.4-(b) respectively presents the SMD distribution along the radial direction in various cross-flow velocities and axial locations. The scatters show the results of the experimentally obtained SMD, and the curves represent the B-spline fit of the experimental data. Figure 5.4-(a) shows that the SMD values decreased along the radial direction. The reason is that smaller droplets are prone to be entrained in the cross-flow, which results in a large number of smaller droplets at the downstream side. A similar phenomenon was also reported by Leong et al [84]. In the x < 10 mm region, the SMD was larger in the 10 m/s cross-flow than that in the 5 m/s cross-flow. This illustrated that with increasing cross-flow velocity, the larger droplets concentrated in the windward side of spray. This is because with increasing cross-flow velocity, the proportion of large droplets was increased, as shown in Figure 5.3-(a), which caused a larger SMD in the higher cross-flow velocity. However, in the x > 10 mm region, the SMD decreased with increasing cross-flow velocity. This could be attributed to two reasons. First, the increase in cross-flow velocity enhances the droplet distortion and breakup. Second, the droplet distribution in the 10 m/s cross-flow is more scattered than that in the 5 m/s cross-flow; therefore, the probability of droplet collision and coalescence is smaller in the 10 m/s cross-flow, resulting in a smaller SMD under a higher cross-flow velocity. Figure 5.4-(b) shows that the SMD values in the y = 48 mm line were larger than those in the y = 25 mm line, except for the first point. The reason is that near the wall surface, the probabilities of droplet coalescence and merge increase; therefore the droplet diameter increases.

5.3 Local Droplet Velocity Distribution

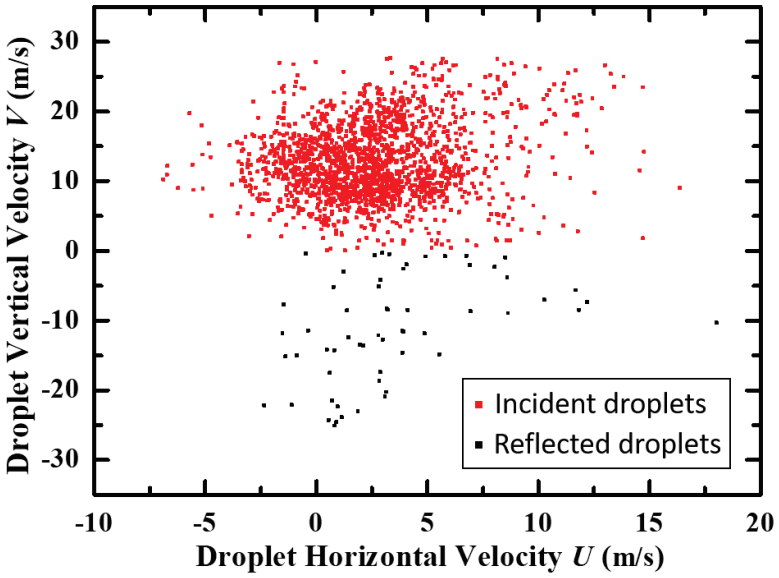

(a) U_x = 5 m/s, x = 5 mm, y = 48 mm

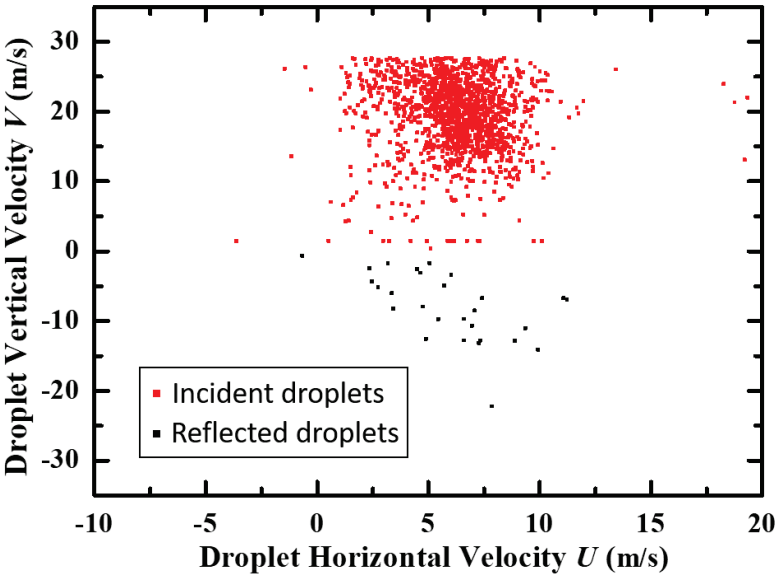

(b) U_x = 10 m/s, x = 5 mm, y = 48 mm

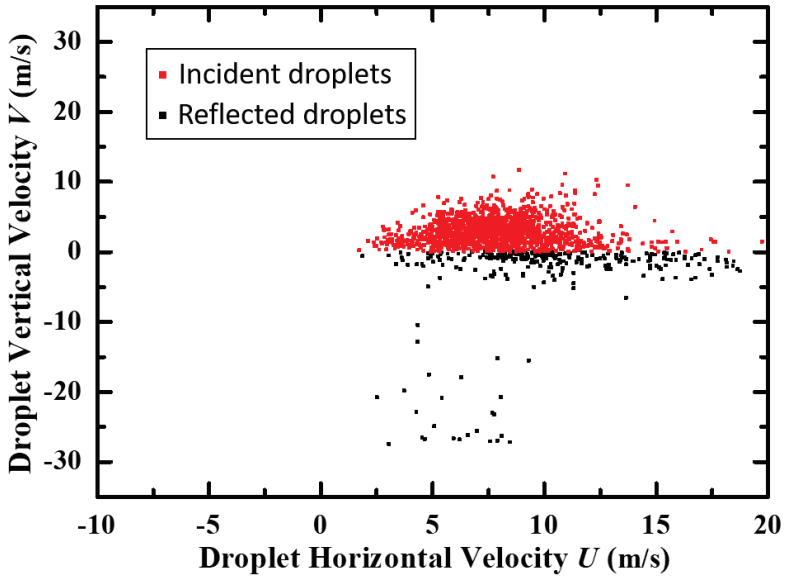

(c) U_x = 10 m/s, x = 20 mm, y = 48 mm

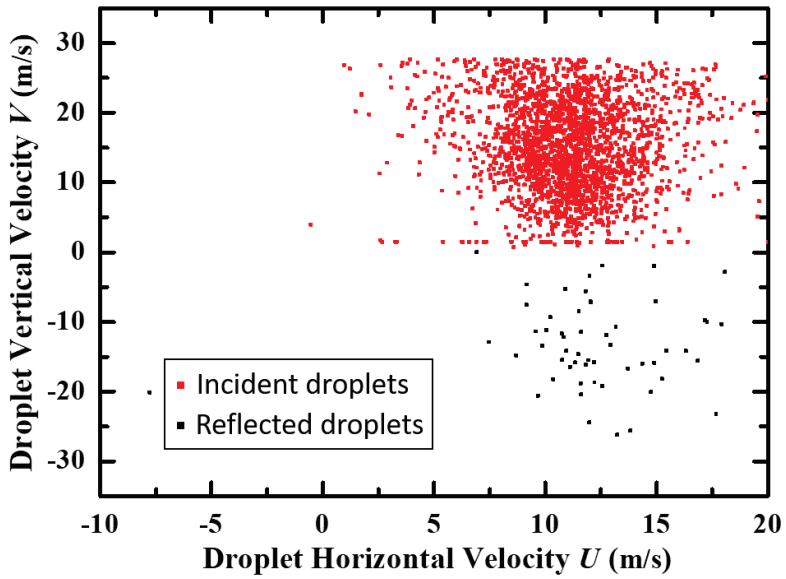

(d) U_x = 10 m/s, x = 5 mm, y = 25 mm

Figure 5.5 Velocities of incident and reflected droplets at regions A, B and C

Based on the mechanism of droplet-wall interaction proposed by Bai-Gosman [85], the formation of fuel film is mainly because of the droplets stick and spread on the wall surface, and the phenomenon of splash and rebound cause the presence of droplets with negative vertical velocity. The droplets measured in PIA experiment with positive vertical velocity were believed as incident droplets and droplets with negative vertical velocity were defined as reflected droplets.

Figure 5.5 shows the droplet horizontal and vertical velocity components at different cross-flow velocities and different locations. The red spots incident the incident droplets and the black spots represent the reflected droplets.

As shown in Figure 5.5-(a), at the region of x = 5 mm and y = 48 mm, some reflected droplets were detected under the cross-flow velocity of 5 m/s. The droplet horizontal velocity mainly distributed between -3 m/s and 10 m/s; however, under 10 m/s cross-flow, the droplet horizontal velocity mainly distributed between 2 m/s and 8 m/s, as shown in Figure 5.5-(b). Obviously, the droplet horizontal velocity distributed was more scattered under 5 m/s cross-flow. This might be because this region is at the spray edge under 5 m/s cross-flow, and this region moves to spray core with the increase of cross-flow velocity. Air entrainment happens at the spray edge, affecting the droplet horizontal velocity distribution. Then the joint effect of air entrainment and cross-flow caused the horizontal velocity distributing more scattered under 5 m/s cross-flow. By comparing Figure 5.5-(b) and Figure 5.5-(c), we found that at the downstream region of x = 20 mm, most droplets moved with almost null vertical velocity. The low positive and negative vertical velocities indicated that large energy loss occurred when the droplets moved to this region. In addition, more droplets with negative vertical velocity were detected, and many droplet horizontal velocity was over the cross-flow velocity of 10 m/s at this region. Which illustrated that wall-jet existed in the region, then the interaction between cross-flow and wall-jet affect the droplet vertical and horizontal velocities distribution. Additionally, by comparing Figure 5.5-(b) and Figure 5.5-(d), it can be seen that the droplets with larger horizontal velocity distributed at the middle spray part of y = 25 mm. This is because the region of x = 5 mm and y = 25 mm located near the spray edge, and the air entrainment caused the droplets traversed outwards. Then many droplets obtained larger horizontal velocity and moved to downstream region.

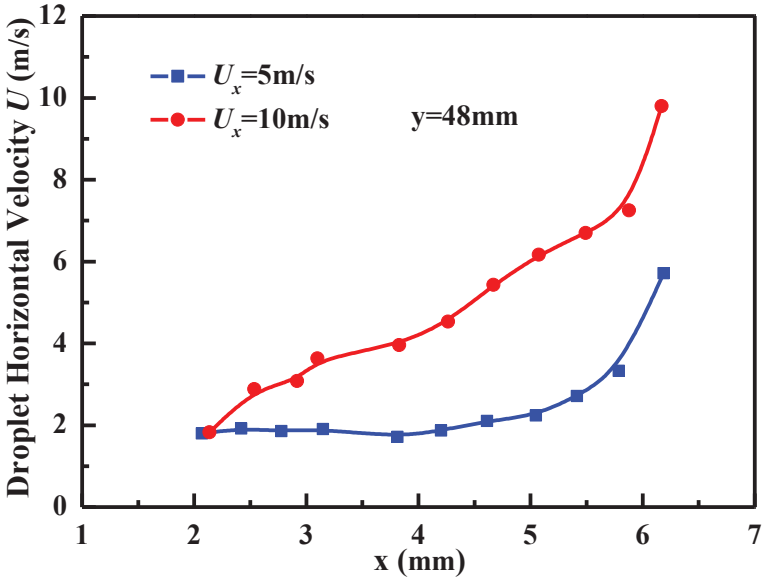

(a) Droplet horizontal velocity distribution

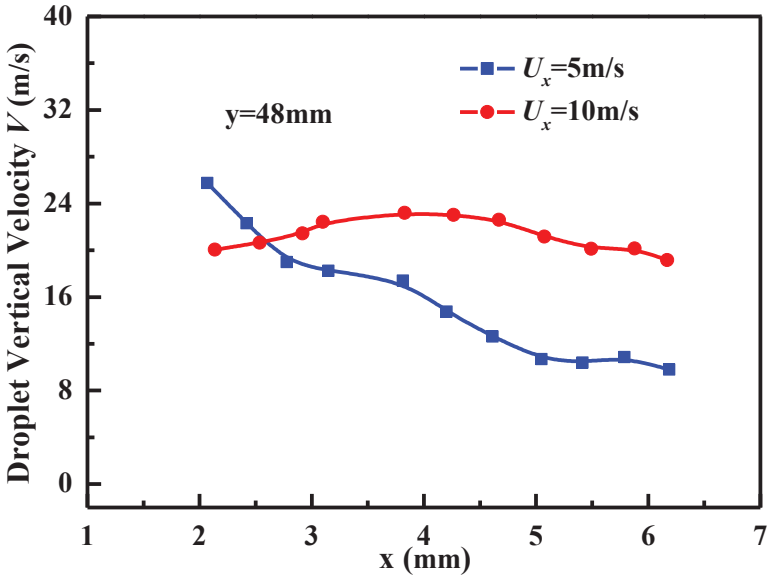

(b) Droplet vertical velocity distribution

Figure 5.6 Effect of cross-flow velocity on droplet horizontal and vertical velocities distributions.

From the Figure 5.6 to Figure 5.8, it can be seen the droplet horizontal and vertical velocities distributions along the cross-flow direction under different cross-flow velocities, radial locations and axial locations. Figure 5.6 shows that the droplet horizontal velocities increased from x = 2 mm to x = 6 mm under the 5 m/s and 10 m/s cross-flow conditions, indicating that in the leeward side of spray the droplets are gradually accelerating and obtain the horizontal momentum

under the cross-flow condition. The droplet horizontal velocity increases with increasing cross-flow velocity. This is because the drag force of the gas phase on the liquid is enhanced in the higher cross-flow velocity, and the drag force increases the droplet horizontal velocity obviously. For the droplet vertical velocity, in the 10 m/s cross-flow, it reaches the maximum value around x = 4 mm, meaning this region is the central portion of the main spray body. However, in the 5 m/s cross-flow, the droplet vertical velocity decreases gradually from x = 2 mm to x = 6 mm.

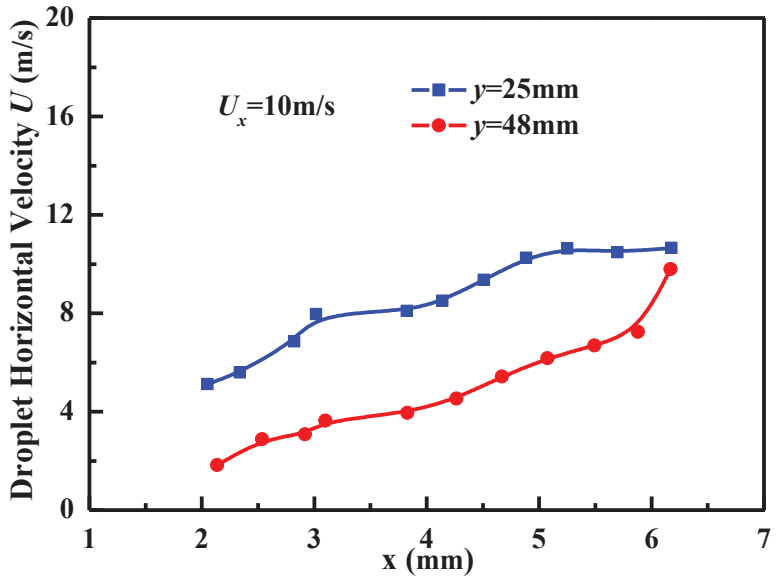

(a) Droplet horizontal velocity distribution

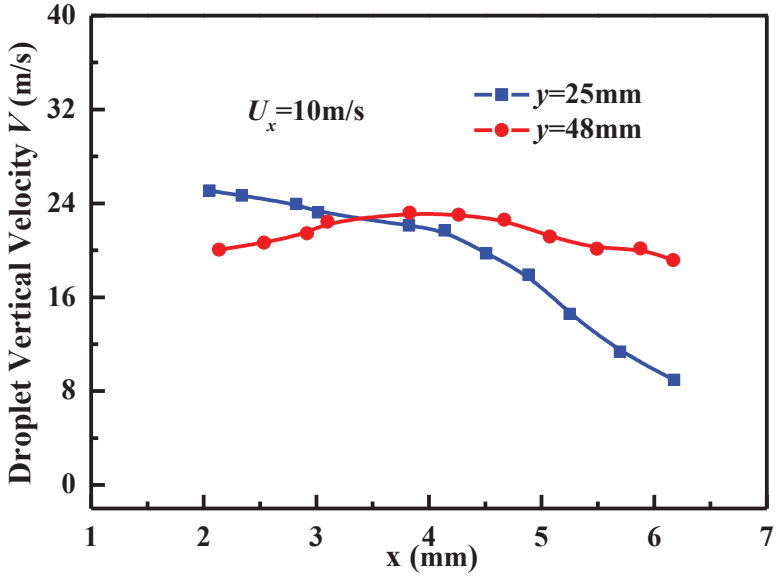

(b) Droplet vertical velocity distribution

Figure 5.7 Effect of axial distance on droplet horizontal and vertical velocities distributions.

Figure 5.7 shows that the droplet horizontal velocity in the middle part of the spray (y = 25 mm) is larger than that near the wall part of the spray (y = 48 mm) in the 10 m/s cross-flow. The reason is that in the line of y = 25 mm, the diameter of the spray liquid column is smaller than that in the line of y = 48 mm, resulting in the droplet in the leeward side of spray to more easily obtain momentum from the cross-flow in the line of y = 25 mm. From the graph of the droplet vertical velocity, in the y = 25 mm line the velocity decreases gradually along the radial direction; however, in the y = 48 mm line the velocity increases to a peak and then decreases. Compared with the velocity in the y = 25 mm line, the maximum value in the y = 48 mm line is smaller, indicating that the droplets decelerate in the axial direction because of drag.

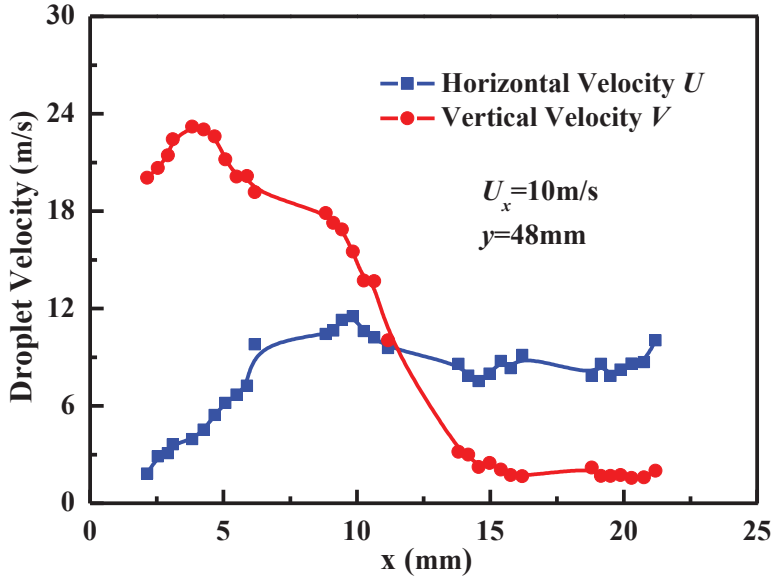

Figure 5.8 Droplet horizontal and vertical velocities distributions along the radial distance.

To observe the velocity variations in a larger region, the droplet horizontal and vertical velocities in the y = 48 mm line under 10 m/s cross-flow were plotted, as shown in Figure 5.8. The droplet horizontal velocity gradually increased along the radial direction, and the maximum value reaches approximately 10 m/s at x = 10 mm. Subsequently, the droplet horizontal velocity showed a large fluctuation from x = 10 mm to x = 22 mm. One possible reason for the fluctuation is the formation of the vortex in the leeward side of spray, similar to the Karman vortex, which was reported in the study of Guo et al. [75]. The droplet vertical velocity reduced drastically from the central portion of the main spray body to the spray periphery (from x = 4 mm to x = 15 mm). The low droplet vertical velocity in the region from x = 15 mm to x = 22 mm indicates that these measuring locations are in the spray stagnation region defined by Lee et al. [86].

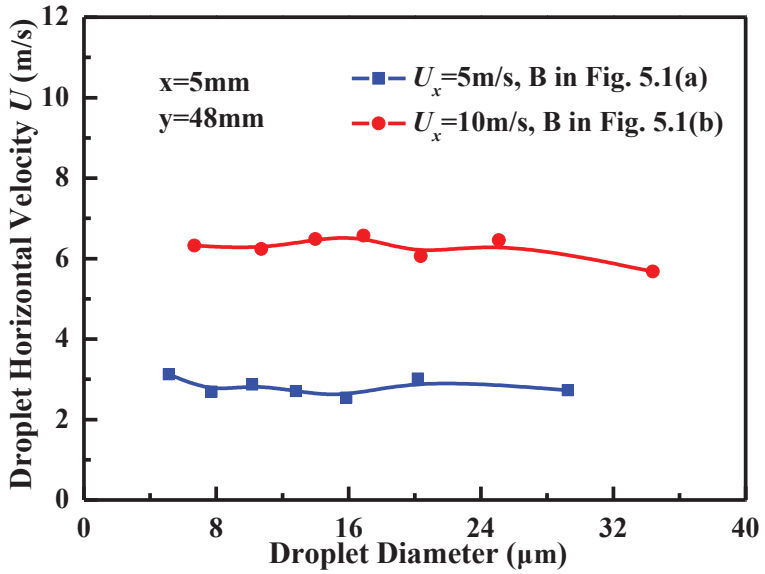

(a) Droplet horizontal velocity as a function of droplet diameter

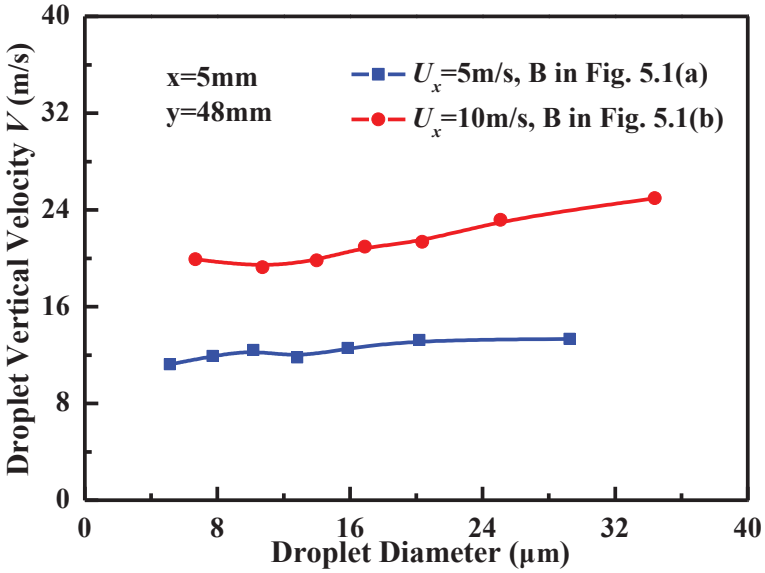

(b) Droplet vertical velocity as a function of droplet diameter

Figure 5.9 Droplet horizontal and vertical velocity as a function of droplet diameter at cross-flow velocities of 5m/s and 10m/s.

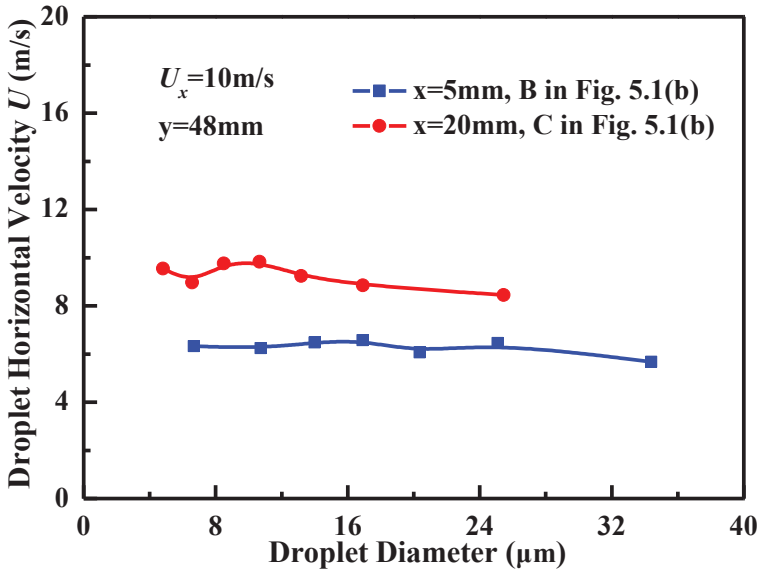

(a) Droplet horizontal velocity as a function of droplet diameter

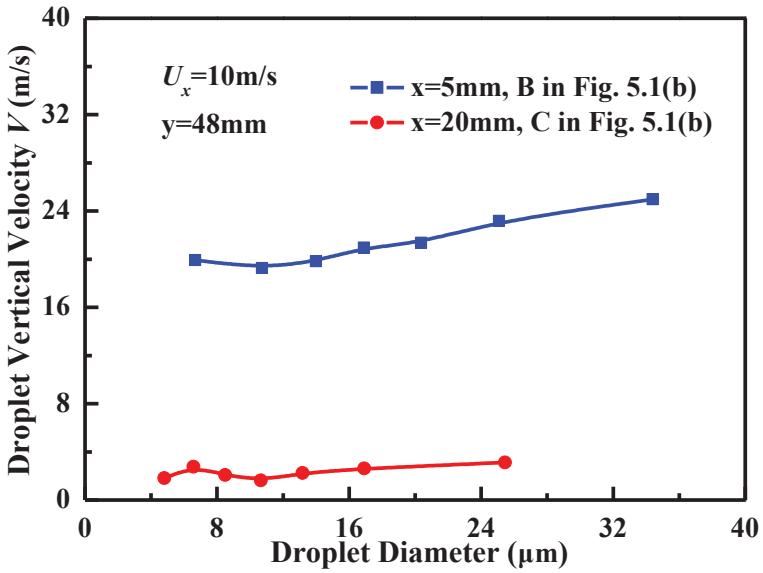

(b) Droplet vertical velocity as a function of droplet diameter

Figure 5.10 Droplet horizontal and vertical velocity as a function of droplet diameter at radial distances of 5 mm and 20 mm.

From the Figure 5.9 to Figure 5.11, the horizontal and vertical velocities of various droplets under different cross-flow velocities, radial locations, and axial locations were shown. Under any given condition, it can be noted that the horizontal velocities are slightly higher for smaller droplets in comparison to larger droplets. This indicates that the smaller droplets are more

easily affected by the cross-flow than the larger droplets. This behavior can be explained by the drag acceleration, which can be represented as

$$a = \frac{F_{Drag}}{m_{drop}} \propto \frac{D^2}{D^3} \propto \frac{1}{D} \tag{5.2}$$

Thus, the acceleration is larger for smaller droplets, and smaller droplets are faster to respond to the drag caused by cross-flow. Moreover, the vertical velocities of larger droplets are higher than that of smaller droplets. One of the reasons is that the larger droplets have higher momentum. Another reason is that the acceleration is smaller for larger droplets; therefore, the larger droplets are less affected by drag.

In order to set up the general expectation for the droplet velocity and droplet diameter, the data in Figure 5.11 were compared. We found that the slope (k) of the droplet horizontal velocity versus droplet diameter correlation was only strongly associated with the radial locations. Then the slope at three radial locations of 5 mm, 10 mm and 20 mm was given in Figure 5.12.

$$k = \frac{U_l - U_s}{d_l - d_s} \tag{5.3}$$

Where U_l is the horizontal velocity of large droplet, U_s is the horizontal velocity of small droplet, d_l is the large droplet diameter and d_s is the small droplet diameter. At all conditions, the horizontal velocity of larger droplet is less than that of smaller droplet by $|k| \times (d_l - d_s)$. The value of k is range from -0.02 to - 0.053 (5 mm≤x≤20 mm). As shown in Fig.16, for the radial location of 20 mm, the horizontal velocity of larger droplet (d_l = 25.5 μm) is 1.3 m/s less than that of smaller droplet (d_s = 8.4 μm).

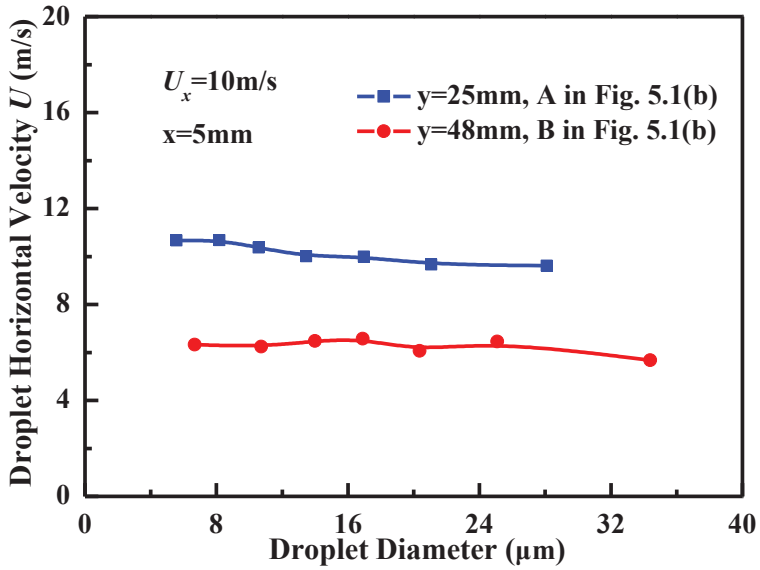

(a) Droplet horizontal velocity as a function of droplet diameter

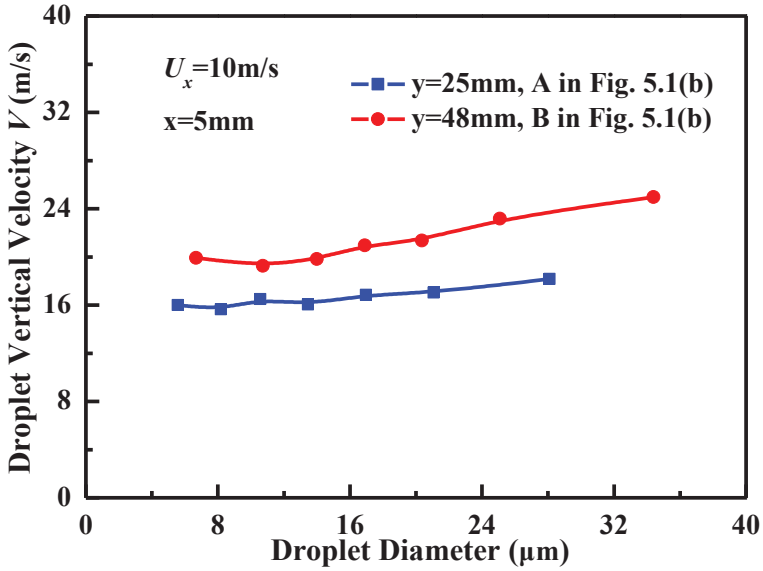

(b) Droplet vertical velocity as a function of droplet diameter

Figure 5.11 Droplet horizontal and vertical velocity as a function of droplet diameter at axial distances of 25mm and 48mm.

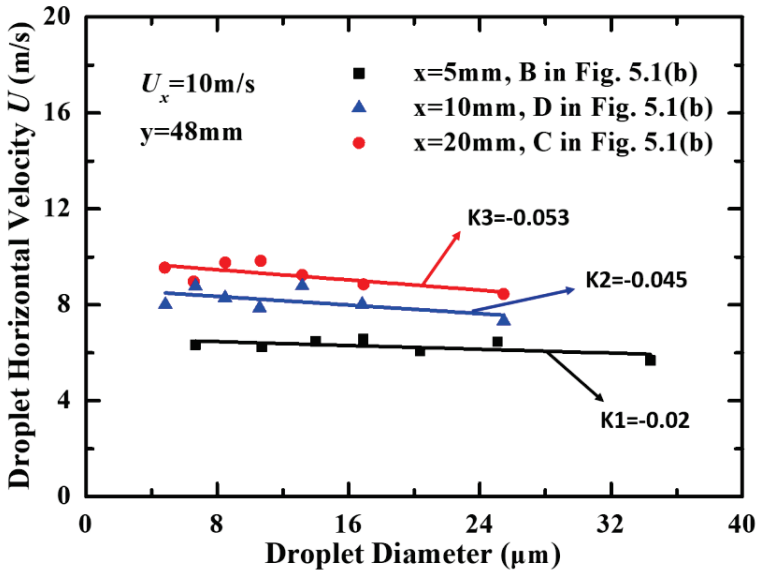

Figure 5.12 Droplet horizontal velocity as a function of droplet diameter at radial distances of 5 mm, 10 mm and 20 mm.

After spray impinging on the wall surface, two main outcomes are expected, i.e., droplet splash and deposition on the wall. The distribution of droplet splash and deposition might reflect the extent of droplet adhesion on the wall, and then influence the combustion and emissions in engines. The average SMD and positive normal velocity component of droplets in twenty injections were used to compute Weber number and Reynolds number when *K* number was plotted in Figure 5.13. According to the empirical correlation presented by Mundo et al. [80], when the *K* value is less than 57.7, most droplets would deposit on the wall surface; otherwise, most droplets would splash off the wall. Figure 5.13 shows that in the line of y = 48 mm, the *K* number decreases along the radial direction in the 5 m/s cross-flow. The *K* number is less than 57.7 for the radial distance beyond 9 mm where a large fraction of incident droplets is deposited on the wall surface. With increasing cross-flow velocity, the droplet splash region shifts to the downstream side. Under the 10 m/s cross-flow condition, the droplet splash region is from x = 1 mm to x = 14 mm, where the spray secondary breakup occurs by impinging, producing a larger number of secondary droplets.

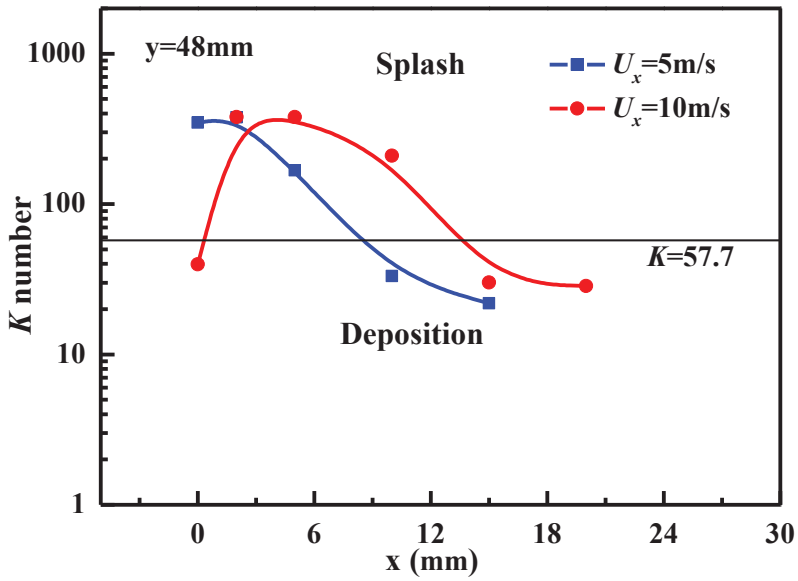

Figure 5.13 *K* number distribution along the radial distance at different cross-flow velocities of 5m/s and 10m/s.

5.4 Spray Droplets Flow Field

For the flow field distribution of spray droplets, it is not enough to just analysis the local droplet velocity of PIA experiment. Especially for the droplet velocity distribution in wall-jet vortex, the droplets movement was significantly complex in this region.

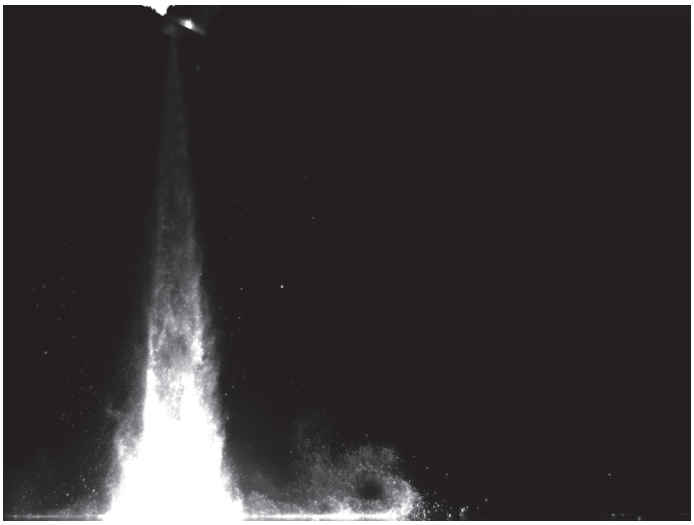

Figure 5.14 Impingement spray image by PIV experiment at 3 ms ASOI (U_x = 0 m/s, P_a = 0.1 MPa)

Figure 5.14 gives the image of the impingement spray of PIV experiment at 3 ms ASOI and without cross-flow. It can be seen that when the laser illuminated from the bottom of cross-flow wind tunnel, the light intensity was extremely strong at the impingement region due to the dense spray and fuel film at the wall surface. Which resulted in that the droplets in the main spray region could not be measured by PIV system. Another reason is that it is difficult to use the same $\triangle t$, which is the interval time between two lasers, at the main spray region and the wall-jet vortex region, because the droplets velocity difference was so large between two regions. Therefore, when the flow field of spray droplets near the wall-jet vortex region was chosen, the measurement of droplet velocity in the main spray part will be error, as shown in Figure 5.15.

Figure 5.15 shows droplet velocity distributions in the wall-jet vortex region in the quiescent surroundings in various time. As shown in Figure 5.15-(a), at 3 ms ASOI, the droplet velocity of wall main jet was largest in the vortex region. However, in the stagnate region, the droplets velocity is almost 0 m/s due to the interaction between incident droplets and re-impingement droplets which were entrained by wall-jet vortex. As time going, at 4 ms ASOI, the

droplet velocities in wall main jet region increased and the droplet velocity directions in the stagnate region became unordered.

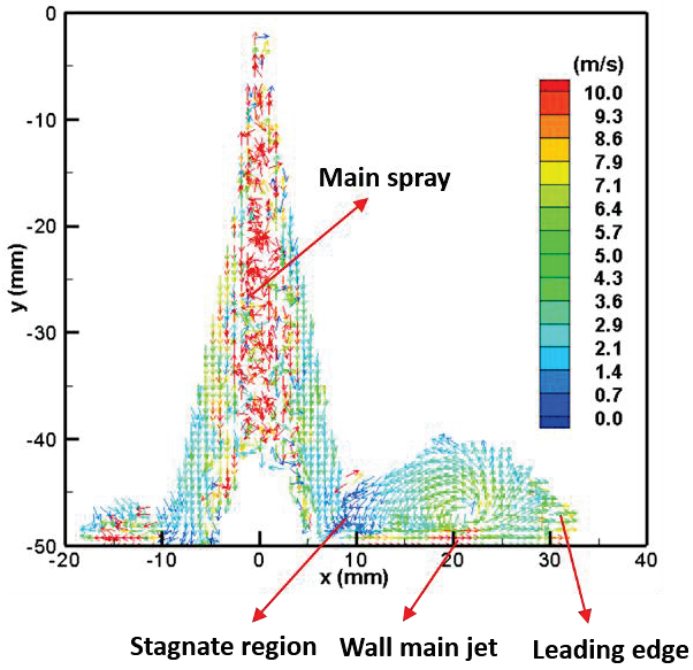

(a) t = 3 ms ASOI

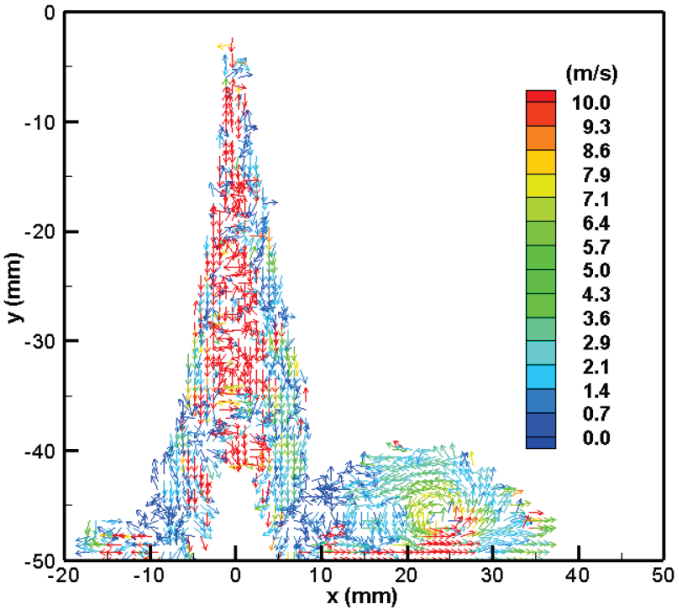

(b) t = 4 ms ASOI

Figure 5.15 Velocity distribution of impingement spray without cross-flow at time of 3 ms ASOI and 4 ms ASOI (U_x = 0 m/s, P_a = 0.1 MPa).

In order to show the vortex velocity distribution more visualized, coordinate system for the wall-jet vortex was defined here. The vortex core is definite as the origin O; the positive x direction indicates the cross-flow direction; and the direction towards the wall surface is the positive y direction, as shown in Figure 5.16-(a).

Figure 5.16-(b) shows at the time of 3 ms ASOI and 4ms ASOI, the velocity distributions along x direction in the horizontal plane of y = 0 mm. We found that the droplet velocity was very low in the vortex core. Moving to negative x direction, the droplet velocities were obviously increased because the droplets cloud entrained by wall-jet vortex concentrated in this region. Continue moving to negative x direction, stagnate region presented in x = -12 mm, the droplet velocities were almost 0 m/s in this region. From the vortex core to positive x direction, the droplet velocity first increased then decreased, until the leading edge the droplet velocity increased again. Near the region of x = 12 mm, the end of spray edge, droplet velocities almost decreased to almost 0 m/s.

Figure 5.16-(c) shows at the time of 3 ms ASOI and 4ms ASOI, the velocity distributions along y direction in the horizontal plane of x = 0 mm. From the vortex core to the wall surface, the droplet velocity increased firstly then decreased. At the wall main jet region, the droplet velocity even could up to 19 m/s. From the vortex core to the upper part of vortex, the droplet velocity increased firstly a little, then at the upper edge of vortex, the droplet velocity decreased, becoming about 2m/s.

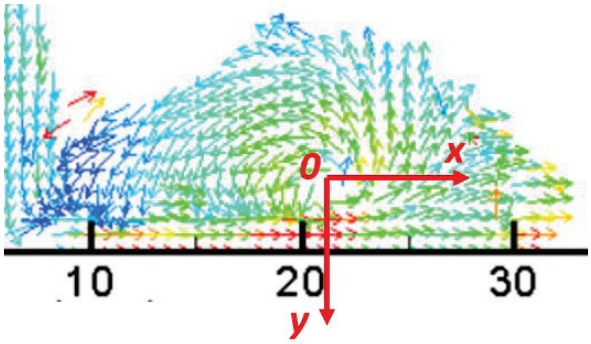

(a) Definition of coordinate system for wall-jet vortex.

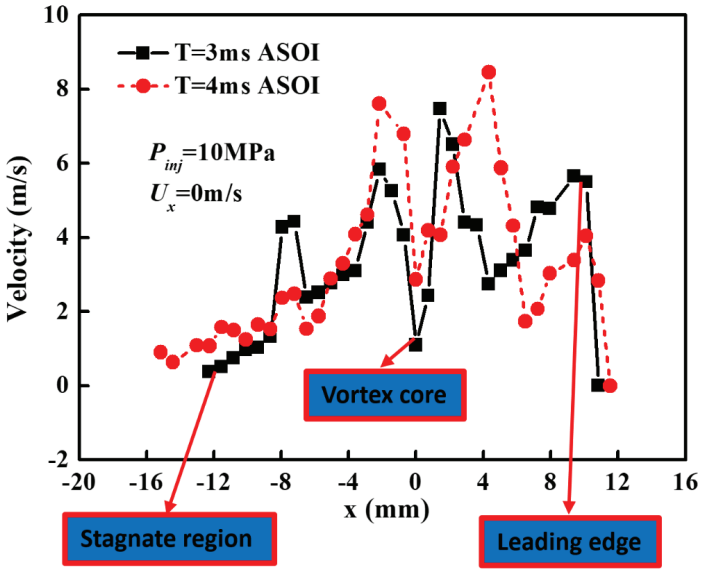

(b) y = 0 mm

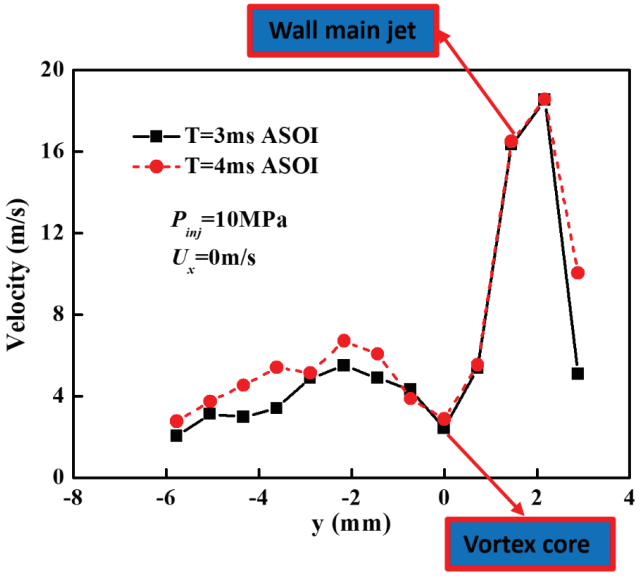

(c) x = 0 mm

Figure 5.16 Velocity distribution of wall-jet vortex (U_x = 0 m/s, P_a = 0.1 MPa, t = 3 ms ASOI).

The velocity distribution of impingement spray in cross-flow of 5 and 10 m/s at 3 ms ASOI are listed in Figure 5.17. In the quiescent cross-flow velocity ambient the velocity distribution in spray tip formed as a vortex structure after impingement, as shown in Figure 5.15-(a). However, the vortex structure of droplet velocity disappeared with the increase of cross-flow velocity. It illustrates that the droplets in wall-jet vortex are entrained by cross-flow after

impingement.

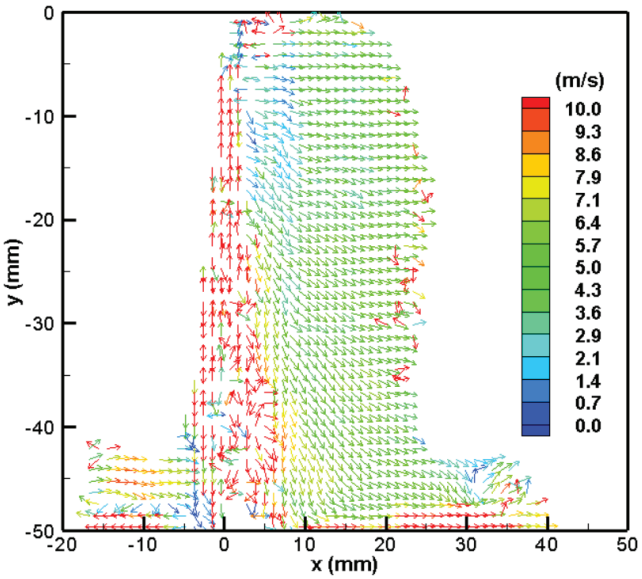

(a) U_x = 5 m/s

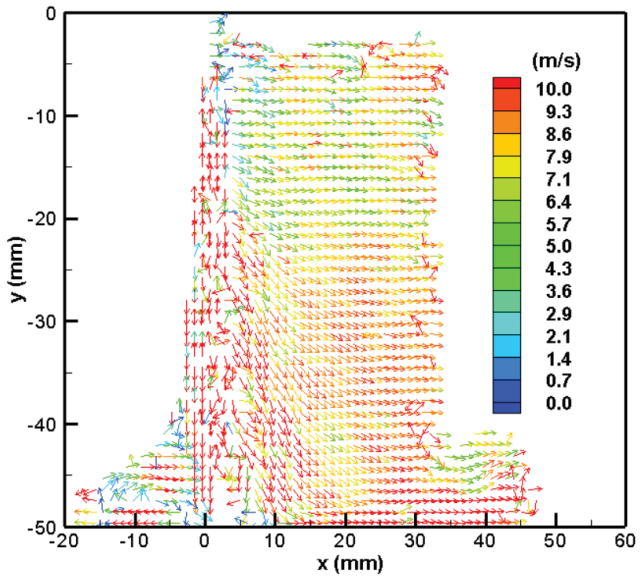

(b) U_x = 10 m/s

Figure 5.17 Velocity distribution of impingement spray under different cross-flow velocities (P_a = 0.1 MPa, t = 3 ms ASOI).

5.5 Major Physical Phenomena of Impingement Spray in Cross-Flow

The above study experimentally investigated the spray structure, droplet diameter, and droplet velocity components in different cross-flow velocities. The major physical phenomena of impingement spray in cross-flow was shown in Figure 5.18.

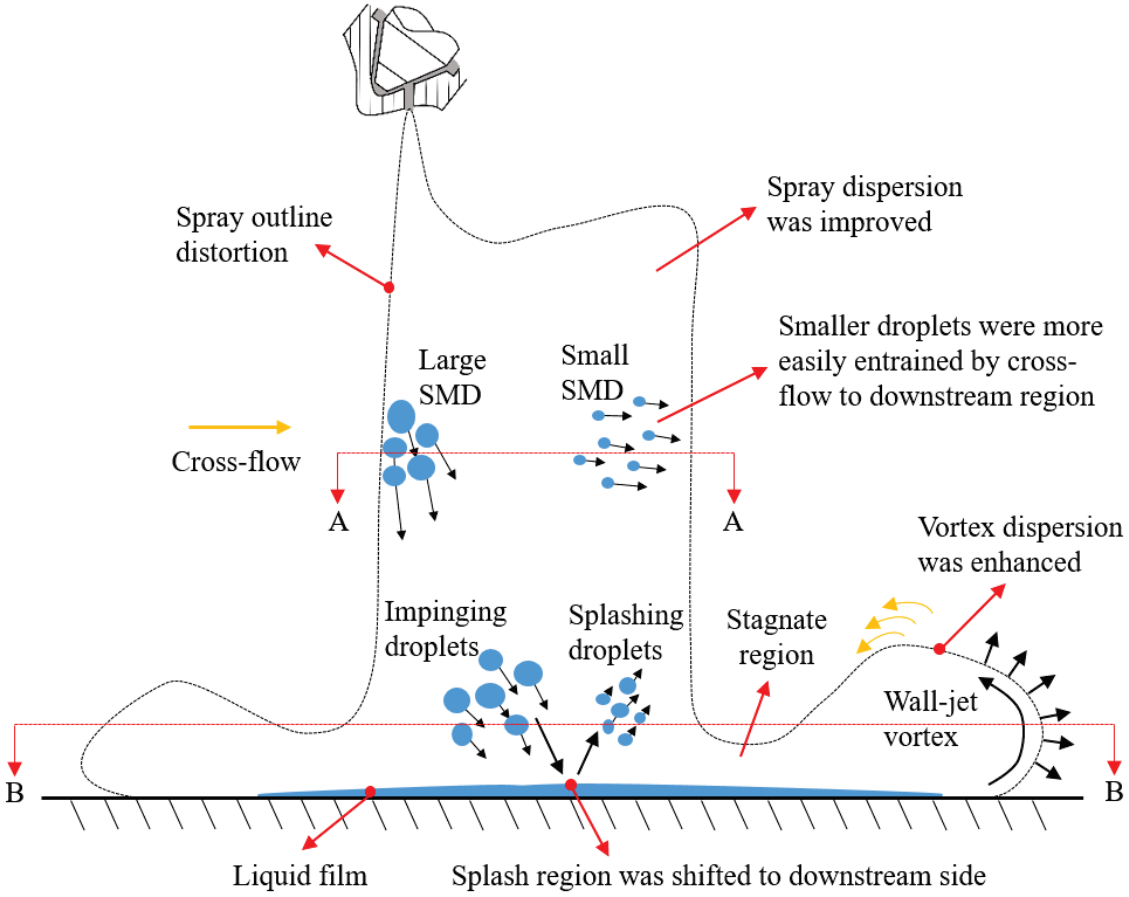

(a) Physical phenomena in vertical plane.

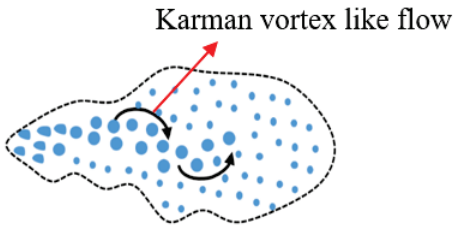

(b) Physical phenomena in the section A-A.

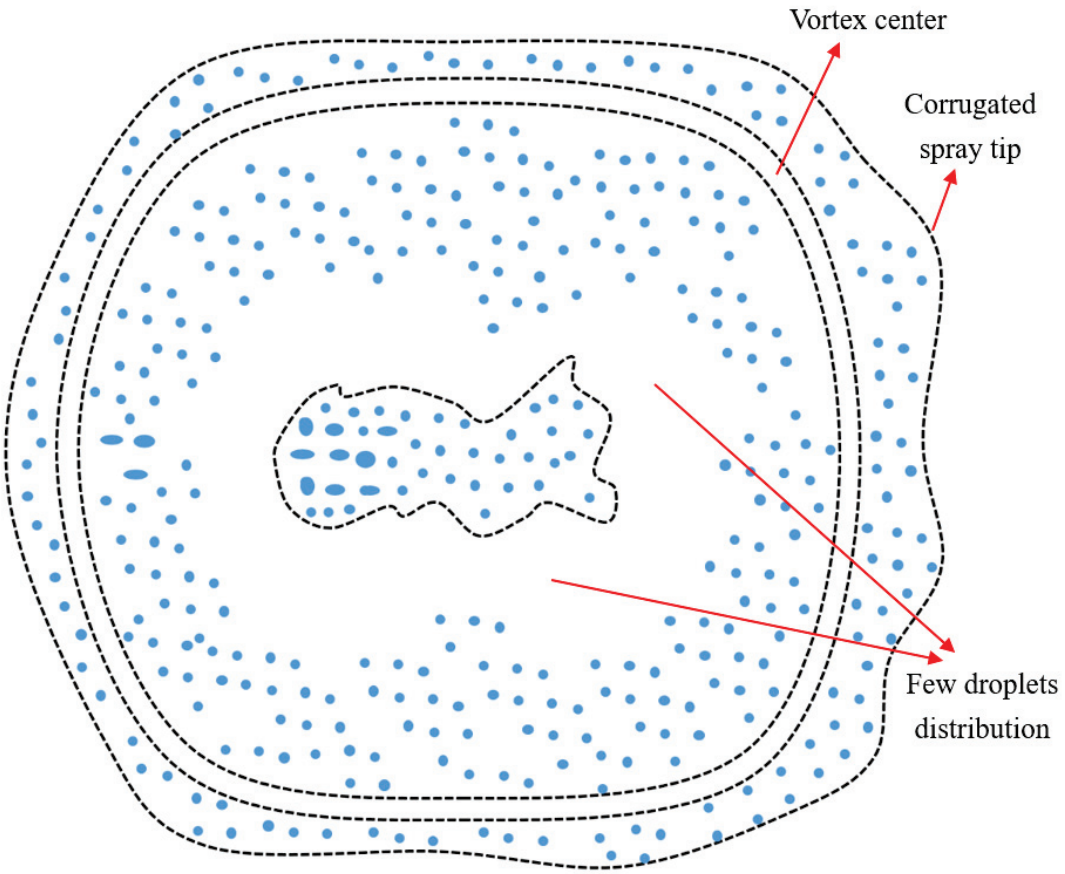

(c) Physical phenomena in the section B-B.

Figure 5.18 Major physical phenomena of impinging spray in cross-flow.

As shown in Figure 5.18-(a), the physical phenomena in vertical plane was presented. Using the high speed photography, we found that with the increase in cross-flow velocity, the spray area increases significantly, i.e., the cross-flow favors spray dispersion. The spray outline distortion caused by cross-flow in the leeward side is larger than that in the windward side. Moreover, the high cross-flow velocity favors the spray breakup and dispersion, leading to a larger wall-jet vortex.

From PIA experimental results, it can be seen that the increased cross-flow velocity leads to larger SMD in the windward side of spray and smaller SMD in the leeward side of spray. Two processes could result in this phenomenon: the increased proportion of large droplets in the windward side of spray, and the enhanced droplet breakup in the higher cross-flow velocity. The two velocity components demonstrate a difference in the behavior of large and small droplets. The smaller droplets are more easily affected by the cross-flow than the larger droplets owing to their

larger drag acceleration. In addition, the increased cross-flow velocity leads to the droplet splash region shifting to the downstream side, where numerous secondary droplets are formed during impinging.

By employing the PIV optical diagnostic method, the flow field of wall-jet vortex was measured. In the quiescent cross-flow velocity ambient the droplet velocity distribution in spray tip formed as a vortex structure after impingement, while the vortex structure of droplet velocity disappeared with the increase of cross-flow velocity. Moreover, a stagnate region exists between the main spray and wall-jet vortex, and the droplets velocity in this region is almost 0 m/s.

Complicated movement in two horizontal planes of y = 25 mm and y = 45 mm were observed by using a high speed video camera and laser sheet. At the plane of y = 25 mm, a complex vortex movement was observed that resulted in a non-uniform distribution of droplets in the upper part of the spray in the leeward side. In addition, at the plane of y = 45 mm, an empty belt area occurred in the vortex core region revealing that the density of the droplets in this region was quite low. A vacant region between the main spray body and the wall-jet vortex appeared, and few droplets distributed in this region. Moreover, the spray tip in the downstream side distributed corrugated.

5.6 Summary

The droplet size and velocity distributions are discussed in the chapter. By employing the particle image analysis (PIA) optical diagnostic method, the Sauter mean diameter (SMD) and the droplet velocity components were investigated. The results show that a higher cross-flow velocity causes an increased proportion of large droplets in the windward side of spray, and the enhanced droplet breakup, resulting in a larger SMD in the windward side of spray and smaller SMD in the leeward side of spray. In the leeward side of spray, the droplet horizontal velocity gradually increases along the cross-flow direction, and after it reaches approximately the cross-flow velocity, the droplet horizontal velocity shows a large fluctuation in the downstream region. Moreover, the droplet vertical velocity decreases sharply from the center line of the main spray body to the spray periphery. At the downstream region of x = 20 mm, many droplets with negative vertical velocity were detected, and many droplet horizontal velocity was over the cross-flow velocity of 10 m/s at this region due to the interaction between cross-flow and wall-jet. By comparing the velocities of droplets, we found that compared with larger droplets, the smaller droplets are more easily affected by a cross-flow owing to the effect of drag acceleration. In addition, the increased cross-flow velocity leads to the droplet splash region shifting to the downstream side, where numerous secondary droplets are formed during impinging.

For the flow field of wall-jet vortex in PIV experiment, in the quiescent ambient the velocity distribution in spray tip formed as a vortex structure after impingement, while the vortex structure of droplet velocity disappeared with the increase of cross-flow velocity. Detailed droplet velocity distribution of wall-jet vortex was analyzed in quiescent cross-flow velocity ambient at 3 ms ASOI. The droplet velocity of wall main jet was largest in the vortex region. However, in the stagnate region, the droplets velocity is almost 0 m/s.

Chapter 6 Near-Field Spray in Cross-Flow

Because of the high turbulence behavior of spray flow at the exit of the nozzle, observing the spray behavior at near-nozzle region, where spray breakup occurs, is beneficial to understanding the mixing and breakup processes of spray. Moreover, in the above analysis, the effects of cross-flow and ambient pressure on the macroscopic structure of the impingement spray are evidently, however, the effects on the near-field spray is unknown. Thus, we will investigate the effects of cross-flow and ambient pressure on the near-field spray structure and droplet distribution in this chapter.

6.1 Experimental Condition

Table 6.1 Experimental conditions

Injection Conditions	
Injector Type	VCO, Single-hole
Hole Diameter : d (mm)	0.15
Injection Mass : Q_{inj} (mg)	4.36
Injection Duration : T_d (ms)	4
Injection Pressure : P_{inj} (MPa)	10
Ambient Condition	
Ambient Gas	Air
Ambient Pressure : P_a (MPa)	0.1, 0.4
Ambient Temperature : T_a (K)	293
Cross-flow Velocity : U_x (m/s)	0, 2, 5

The detailed experimental conditions are listed in Table 6.1. Dry-solvent was utilized as a test fuel in this study. The injector type is VCO type with a single hole, and the hole diameter is 0.15 mm. The injection pressure was 10 MPa and the injection duration was 4 ms ASOI with the injection mass of 4.36 mg. The ambient pressure were 0.1 and 0.4 MPa. The observation of near-field spray was conducted under the cross-flow velocities of 0, 2 and 5 m/s. The measurement at every condition was repeated three times.

6.2 Development of Near-Field Spray Structure

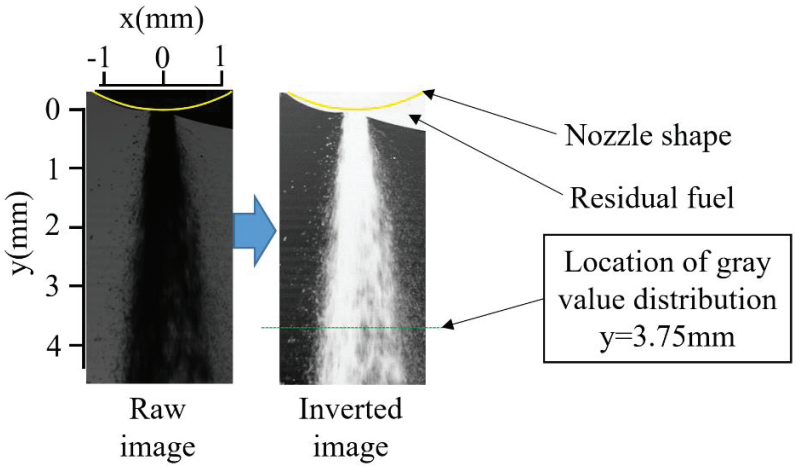

Figure 6.1 Image processing of near-field spray

Figure 6.1 shows how we process the raw image of near-field spray and the image description. The raw image was inverted thus the gray value of black has a count of 255 and the white of 0 and consequently the gray valve is larger at dense spray region. It is not easy to identify the nozzle shape in this image owing to the residual fuel, thus the nozzle shape is indicated by a yellow arc here. To observe the droplets distribution in a substantially intuitive manner, the gray values were extracted in a line of y = 3.75 mm which is located at 25 times of nozzle hole diameter downstream from the nozzle exit, as shown by the line marked with green dots.

Figure 6.2 shows the effect of cross-flow velocity on the spray profiles at the immediate nozzle downstream (y < 5 mm) with ambient pressures of 0.1 and 0.4 MPa. In this figure, two typical images at 0.05 ms and 2 ms were shown, corresponding to the initial stage and the steady stage of spray evolution respectively. The effect of cross-flow on the initial spray seemed weak; however, cross-flow caused droplets distribution in both sides of the spray quite differently at 2 ms ASOI. There are almost no droplets in the windward side but numerous tiny droplets are distributed in the leeward side, as shown in the red rectangle. The droplets in the windward side were entrained by cross-flow and shifted downstream. For initial spray, only a few ligaments and droplets were generated at the spray edge under high ambient pressure of 0.4 MPa, and this is evidently different from that of lower ambient pressure (Pa = 0.1 MPa) that show numerous ligaments and droplets formation because of the residual fuel breakup. This phenomenon could be explained based on the fact that at a higher ambient pressure, the residual fuel of the last injection was compressed to 0.4 MPa before the injection occurred. Thus, the denser spray tip is less easy

to breakup into ligaments and droplets compared with that at lower ambient pressure.

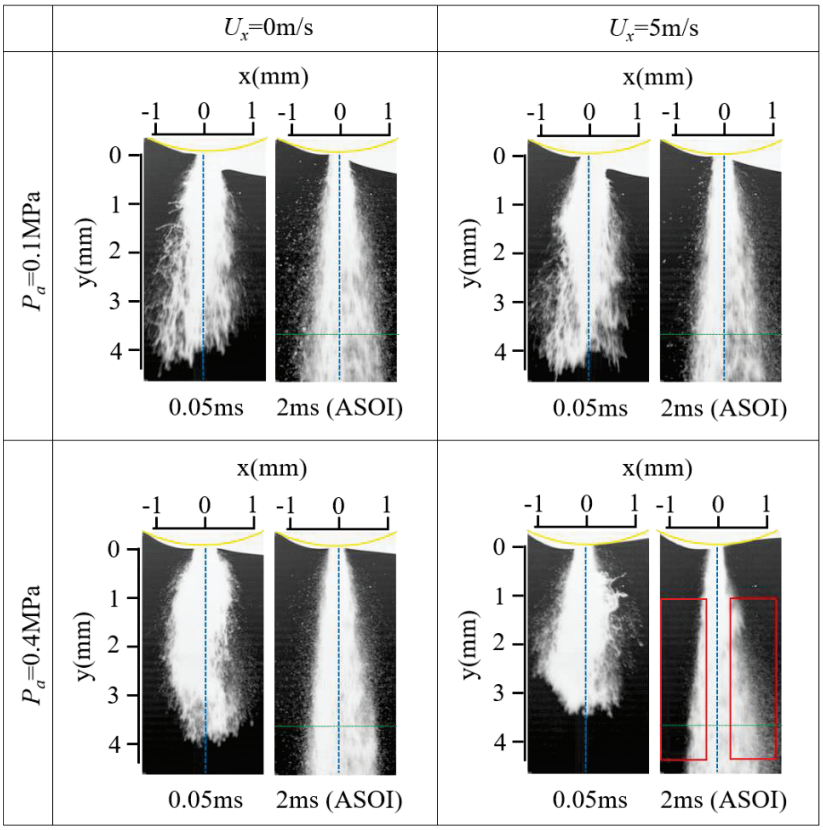

Figure 6.2 Comparisons of near field spray profiles under different cross-flow velocities and ambient pressures.

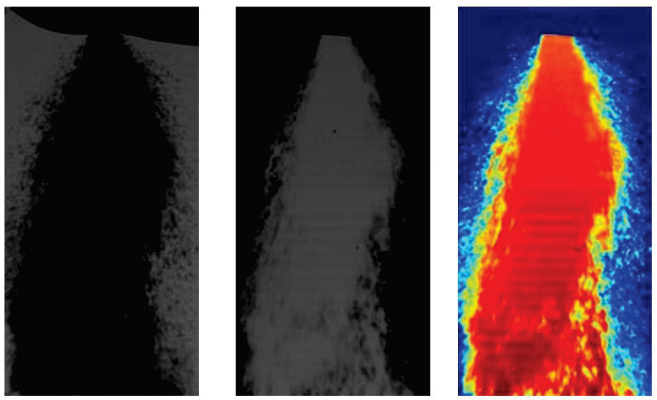

Original image (I_a)　　I_0-I_a　　False color image

Figure 6.3 Image processing of near-filed spray (I_0 indicates background image).

False color images of near-flied spray were shown in the following figures due to the fact that they are beneficial to observe droplets distribution and the details of liquid breakup. Figure

6.3 gives the image processing method of near-filed spray. First, the original image brightness values were reduced by those of background image. The processed image can subsequently be shown in false color format based on the image brightness.

From the Figure 6.4 to Figure 6.7, the near-field spray structures varying with time are shown at the ambient pressure of 0.1 MPa. It can be seen that the effect of cross-flow on the near-field spray structures was minimal at the start of injection (SOI), middle of injection (MOI) and end of injection (EOI), respectively. However, the effect of cross-flow on the near-field spray at significant at 0.4 MPa ambient pressure due to the larger momentum flux of cross-flow.

Figure 6.7 shows the effect of cross-flow on the near-flied spray with the ambient pressure of 0.4 MPa, at the start of injection (SOI). 5m/s cross-flow moved from upstream to downstream, means that high drag caused by cross-flow forced on the spray. It is therefore not surprising to see that large droplets cloud striped from the main body of spray under cross-flow condition. Figure 6.8 were obtained at the middle of injection (MOI) under an injection pressure of 10 MPa and an ambient pressure of 0.4 MPa. It can be observed that the main body of pray slightly shifted downstream and droplets distributions in the windward side and leeside were uneven under 5m/s cross-flow condition. More droplets concentrated in the leeward side of spray. However, the main body of spray was al- most vertical and droplets distributions in both sides were even without cross-flow. In addition, under cross-flow field, the main body of spray is thinner compared to that of without cross-flow. It is possible that lots of droplets are striped from the main body of spray, meanwhile the cross-flow compresses the spray to downstream.

The droplets are key parameters to determine the atomization and mixing processes. When the cross-flow velocity goes up, the breakup is significantly more intense at the end of injection (EOI), as shown in Figure 6.9. The structures at the end of injection appear diffuse and blurry. It is noted that without cross-flow, the droplets distribution was almost axisymmetric. However, under cross-flow condition, the large droplets mainly distributed on the windward side and small droplets mainly distributed on the leeside. Compared with the condition of without cross-flow, the droplets are tinier under cross-flow. This reveals that the cross-flow make spray structures difficult to hold together by liquid surface tension forces, and thus cross-flow is favor of forming smaller size droplets.

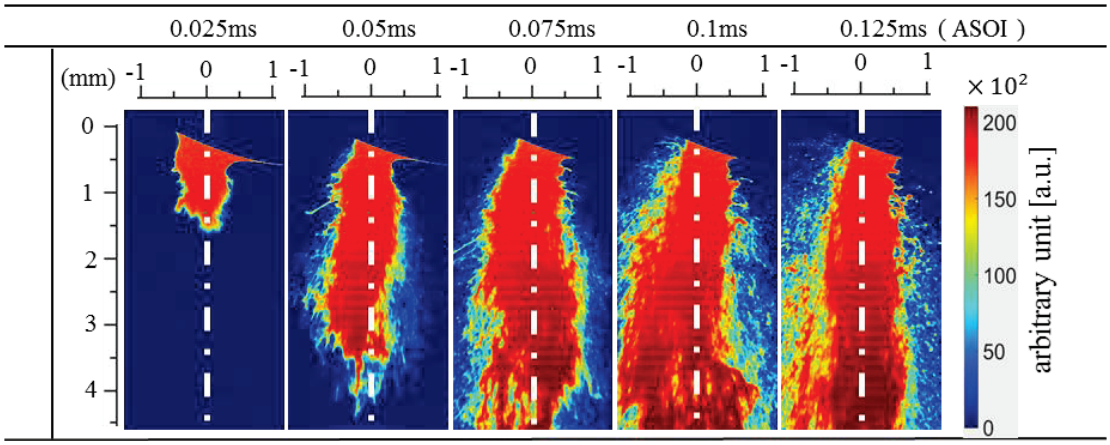

(a) U_x=0m/s

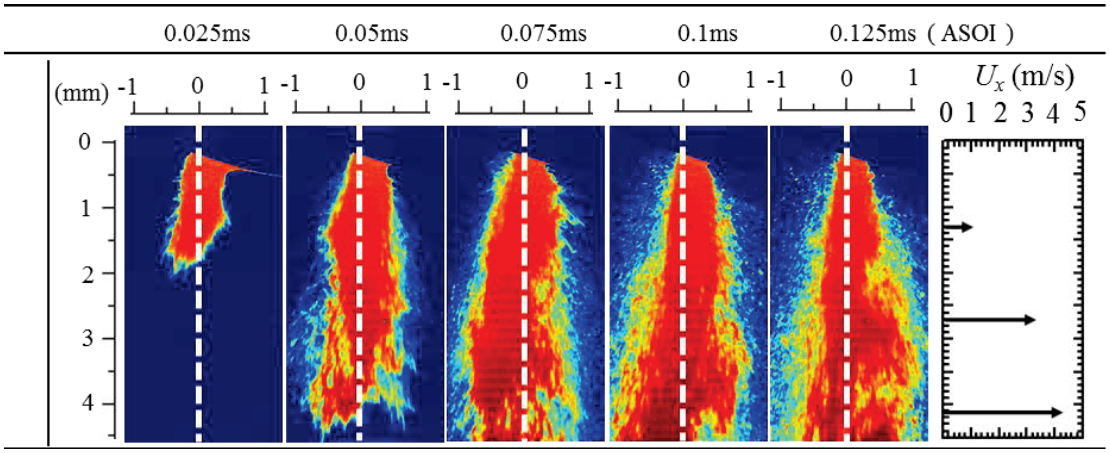

(b) U_x=5m/s

Figure 6.4 Time sequences of near-field spray around SOI (P_a= 0.1MPa).

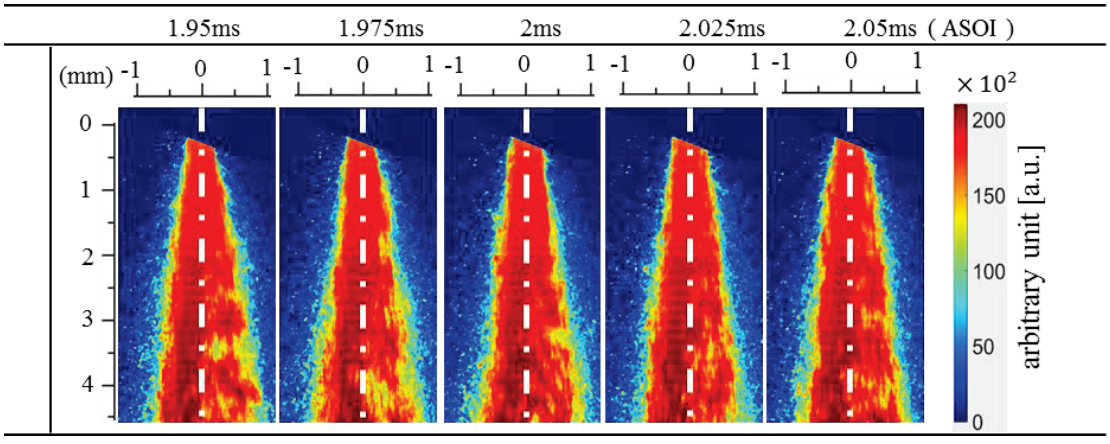

(a) U_x=0m/s

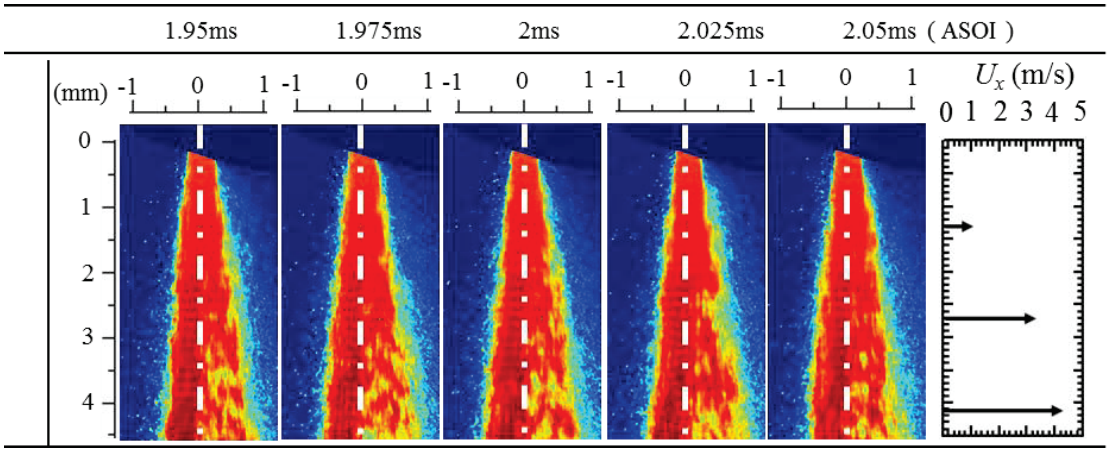

(b) U_x=5m/s

Figure 6.5 Time sequences of near-field spray around MOI (P_a= 0.1MPa).

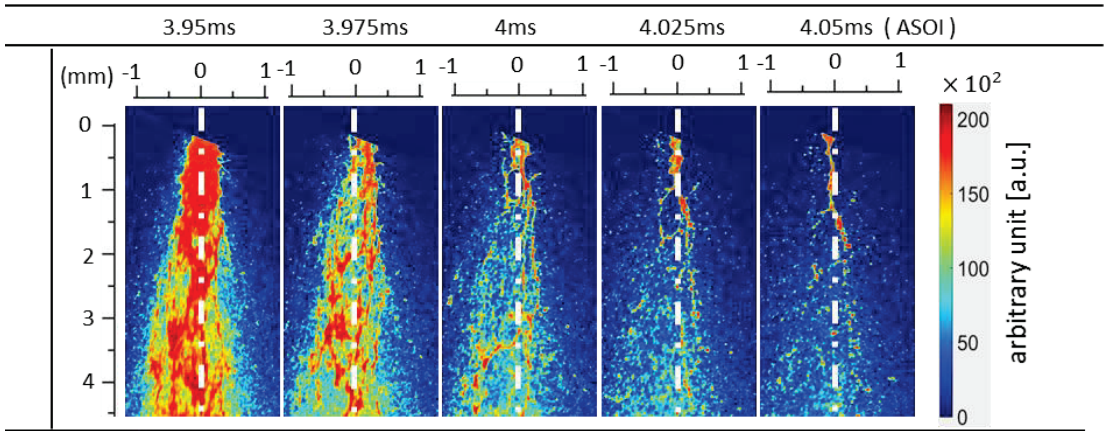

(a) U_x=0m/s

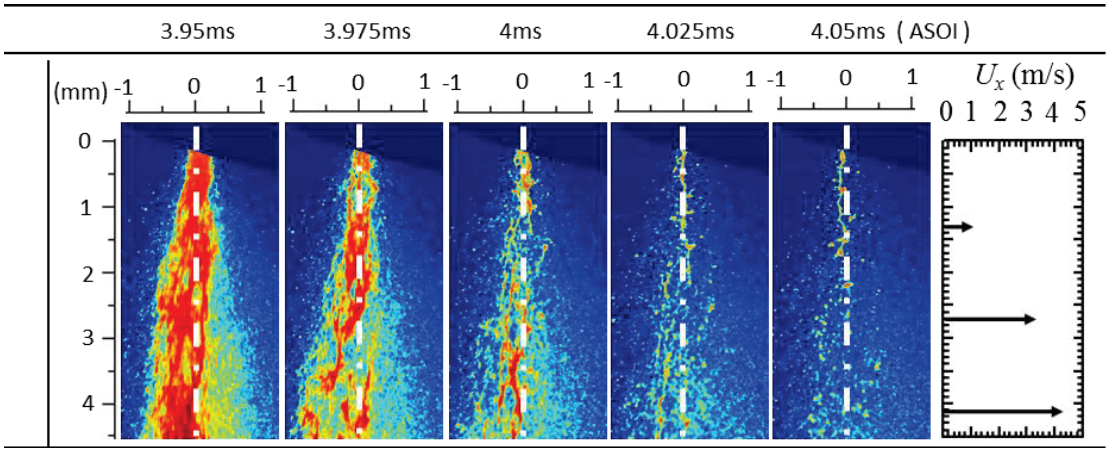

(b) U_x=5m/s

Figure 6.6 Time sequences of near-field spray around EOI (P_a= 0.1MPa).

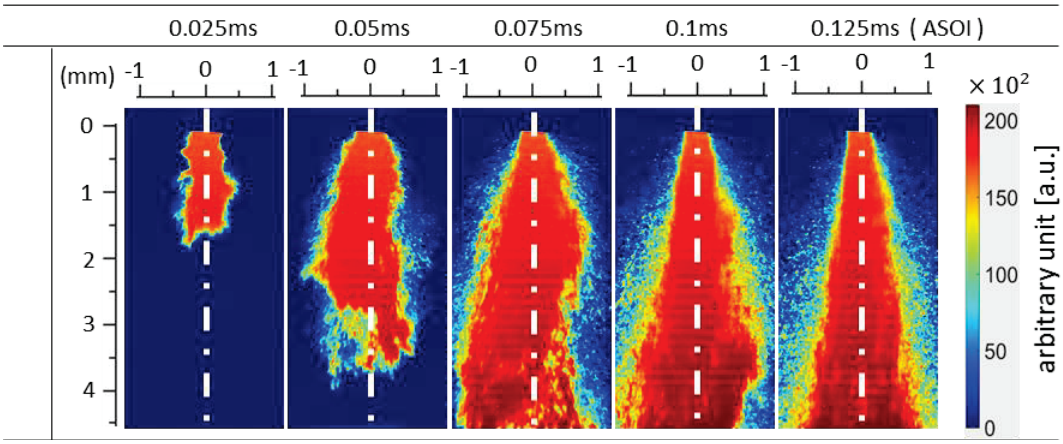

(a) U_x=0m/s

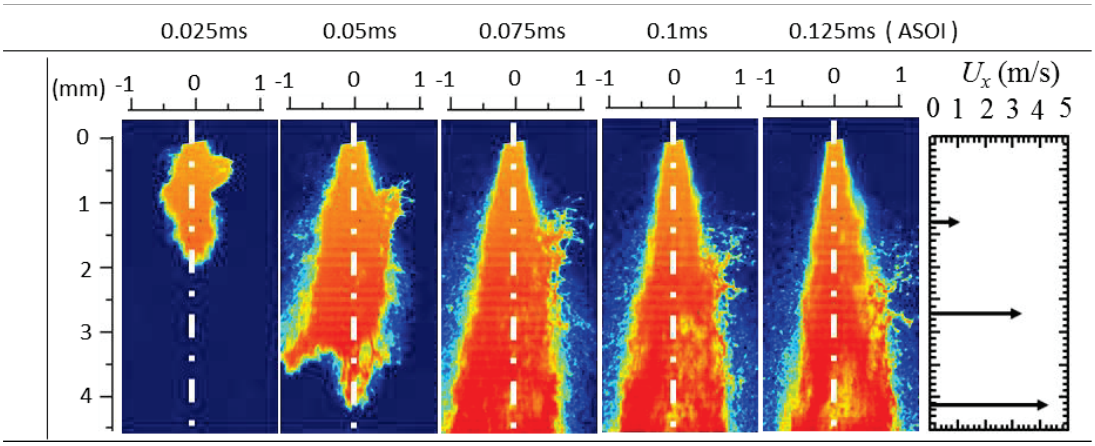

(b) U_x=5m/s

Figure 6.7 Time sequences of near-field spray around SOI (P_a= 0.4MPa).

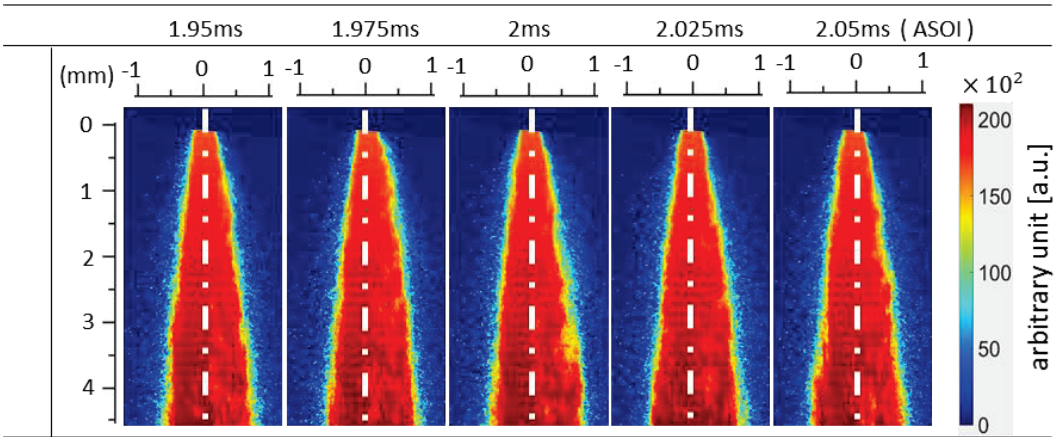

(a) U_x=0m/s

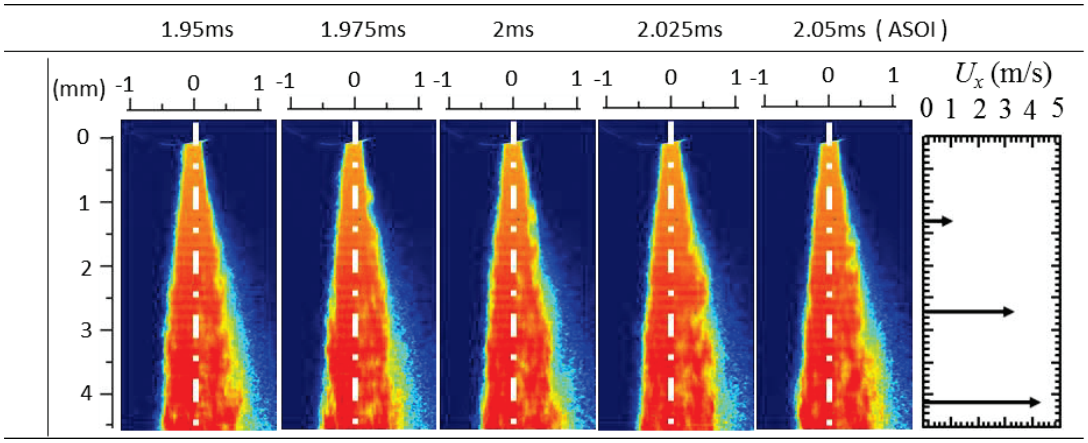

(b) U_x=5m/s

Figure 6.8 Time sequences of near-field spray around MOI (P_a= 0.4MPa).

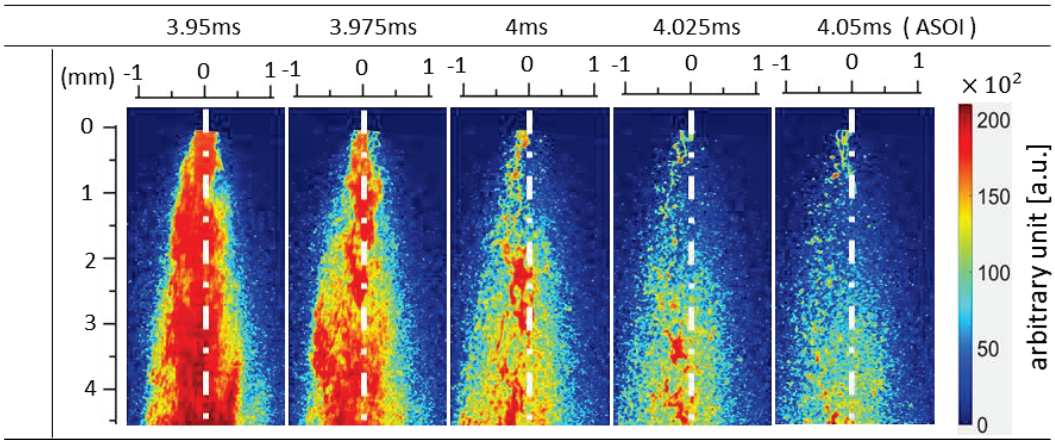

(a) U_x=0m/s

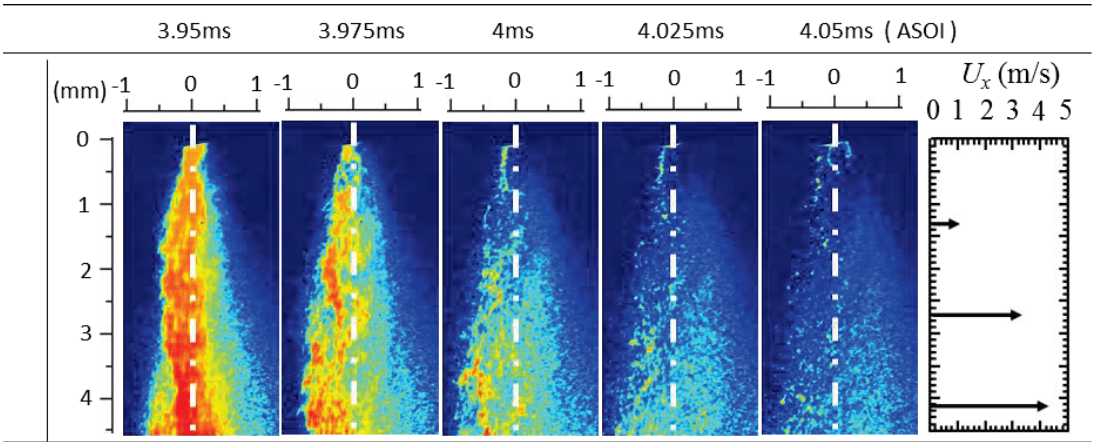

(b) U_x=5m/s

Figure 6.9 Time sequences of near-field spray around EOI (P_a= 0.4MPa).

6.3 Spray Droplets Distribution

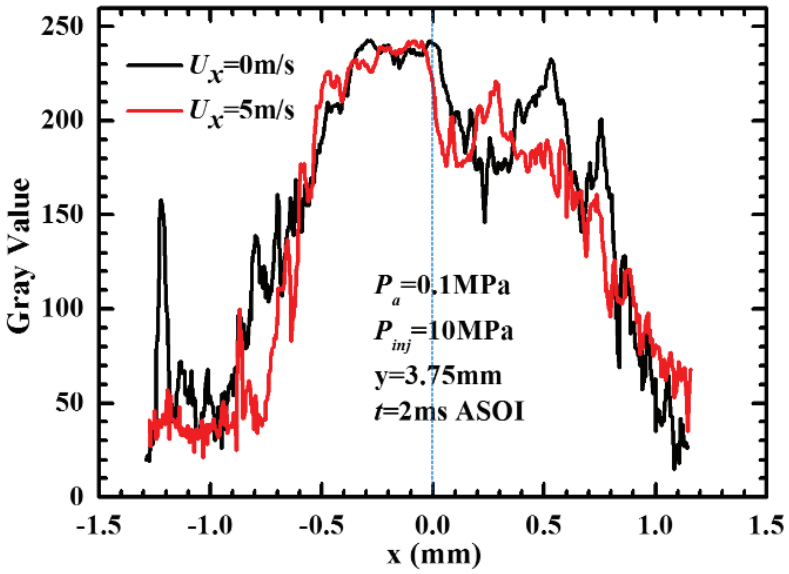

(a) P_a = 0.1 MPa

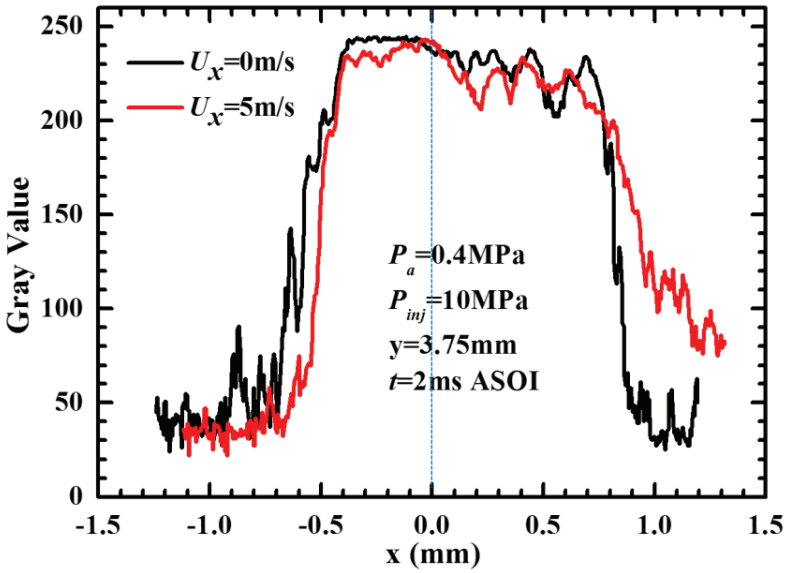

(b) P_a = 0.4 MPa

Figure 6.10 Gray value distributions in the line of y = 3.75 mm under different cross-flow velocities and ambient pressures.

Figure 6.10 compares the gray value distributions in a line of y = 3.75 mm. At low cross-flow velocity, the gray value in windward side is larger than that in the case of high cross-flow velocity, which suggests that a considerable amount of droplets were shifted downstream under

cross-flow condition. Particularly at a 0.4 MPa ambient pressure, the whole spray evidently shifted downstream because of cross-flow. This phenomenon was considerably evident at higher ambient pressure due to its lager momentum flux at the same cross-flow velocity. Near the axis of the nozzle hole, the gray value distributed unevenly at lower ambient pressure compared with that at higher ambient pressure. This is because the spray at higher ambient pressure was compressed thereby the spray became dense and uniform.

6.4 Spray Outline

The outlines of near-field spray in various cross-flow velocities plotted by colored curves are listed in Figure 6.11. The threshold of outline curve is 20 out of 255, and the curve was selected based on the condition whose penetration is almost same with the average penetration. At the time of 0.05 ms ASOI, for a given cross-flow velocity, the spray tip penetration decreased as the ambient pressure increased. This is primarily attributed to the larger aerodynamic drag force under higher environmental gas density. In the case of 0.4 MPa ambient pressure and 0.05 ms ASOI, the spray tip penetration evidently decreased with increasing cross-flow velocity, and this phenomenon is consistent with the quantitative analysis in Figure 3.17. From the images at 2 ms ASOI, we could visualize that the whole spray curve shifted downstream with the increase in cross-flow velocity, and this is particularly evident at higher ambient pressure. In addition, it is noted that the spray outline was wider at initial stage of spray evolution than that at steady stage of spray evolution. This is due to the low axial velocity and the sudden high-level fluctuations of radial velocity during the needle opening [87].

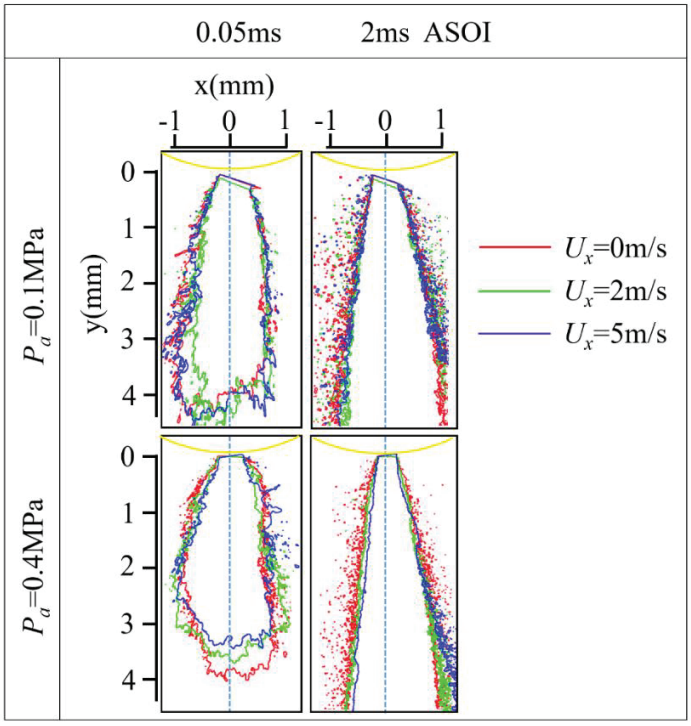

Figure 6.11 I Comparisons of near-field spray outlines under different cross-flow velocities and ambient pressures (P_{inj} = 10 MPa)

6.5 Summary

The effects of the cross-flow and ambient pressure on the near-field spray have been discussed in this part. The spray profiles at SOI, MOI and EOI under quiescent ambient and 5 m/s cross-flow with different ambient pressures have been listed. Gray value distributions in the line of y = 3.75 mm under various cross-flow velocities and ambient pressures have been discussed. The near-field spray outlines under different cross-flow velocities and ambient pressures were compared.

For near-field spray, the spray image at higher ambient pressure shows fewer ligaments. With increasing cross-flow velocity, the whole spray shifted downstream. The spray outline was wider at the initial stage (0.05ms ASOI) than that at steady stage (2ms ASOI) of spray evolution.

Under cross-flow condition, it can be observed that a large droplets cloud strips from the main body of spray at the time around SOI. The droplets distributions in the windward side and leeside are uneven at MOI. The spray structures at EOI appear diffuse and blurry. Increasing cross-flow velocity tend to form tinier droplets. Thus the cross-flow is beneficial to the fuel spray breakup.

Chapter 7 Numerical Simulation

7.1 Basic Equations and Models Selection

7.1.1 Basic equations

The impingement fuel spray was analyzed using Lagrangian spray module which involves the conservation equations of liquid phase and vapor phase simultaneously. The liquid phase simulation is conducted with a statistical discrete droplet method [88-89], and in which a group of droplets with the identical properties are represented by a parcel. In Eulerian formulation, a source term of an additional transport equation for the vapor void fraction was employed to illustrate the vapor of spray.

The conservation equations of mass, momentum and energy for the multiphase flows are shown as the following.

$$\frac{D\rho}{Dt} + \rho \frac{\partial u_i}{\partial x_i} = 0 \quad , \tag{7.1}$$

$$\rho \frac{Du_j}{Dt} = \rho \left(\frac{\partial u_j}{\partial t} + u_i \frac{\partial u_j}{\partial x_i} \right) = -\frac{\partial P}{\partial x_j} + u_i \frac{\partial \tau_{ij}}{\partial x_i} + f_j \quad , \tag{7.2}$$

$$\rho \frac{De}{Dt} = \nabla \cdot (\lambda_h \nabla T) - P(\nabla \cdot \vec{u}) + \mu\varphi + \frac{\dot{Q}_s}{dx_1 dx_2 dx_3} \quad , \tag{7.3}$$

where, x_i and x_j indicate the coordinates in the different directions (m); u_i and u_j represent the velocity components in the different axis (m/s); τ_{ij}indicates stress tensor (N); $f_j$is the body force (N); e represent internal energy (J); λ_h is heat transfer coefficient (w/(m · K)); T indicates temperature (K); μ is dynamic viscosity (Pa·s); φ represents dissipation function; and $\dot{Q}_s$is heat flux (J). Equation 7.1 describes the continuity equation, Equation 7.2 is the conservation of momentum, and Equation 7.3 shows the conservation of energy.

In this study, the basic Reynolds averaged Navier-Stokes (RANS) governing equations were applied for simplifying the processing and shortening the calculation time. The standard $k - \varepsilon$ model proposed by Launder and Spalding [90] was applied to provide the description of the turbulent kinetic energy and its dissipation rate.

7.1.2 Models selection

The numerical simulation of the impingement spray in the cross-flow was carried out using CONVERGE software. In this part, the sub-models of the spray breakup, droplets interaction and wall interaction will be described. In addition, the selection of models parameters will be presented.

The instable surface wave theory is considered as an important method in investigating the droplet break up. It indicates that the increasing of the Kelvin-Helmholtz (KH) instable waves results in the droplets stripping from liquid column, this model is suited for conditions of high relative velocity and high ambient gas density. In this simulation, KH and RT (Rayleigh-Taylor) models were used for the spray breakup process. The model is usually called as the KH-RT model [91], which is an improvement of the WAVE model, the disturbance is included in this model.

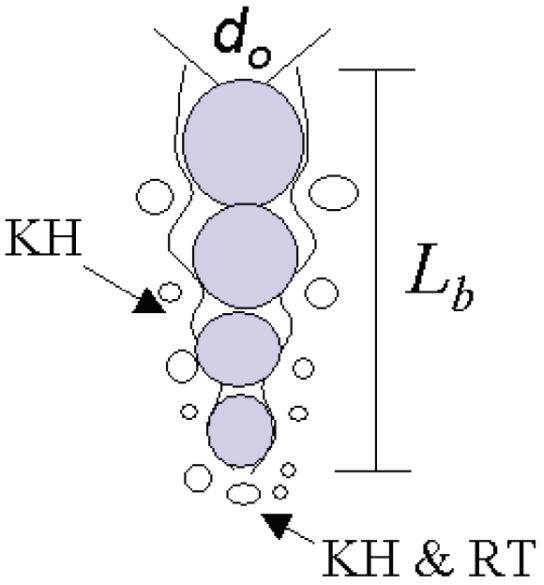

Figure 7.1 Schematic of the KH-RT spray breakup model.

In KH-RT breakup model, an intact core or breakup length L_b (see Figure. 7.1) can be given by the following formula:

$$L_b = C_{bl}\sqrt{\frac{\rho_l}{\rho_g}}d_0 \tag{7.4}$$

As given in Figure. 7.1, liquid blobs are injected with a diameter equal to that of the injector nozzle. This model assumes that only KH instabilities are responsible for drop breakup

inside of the characteristic breakup distance, L_b, while both KH and RT mechanisms are activated beyond the breakup length.

CONVERGE provides a particle-based wall film for modeling the interaction of liquid droplets with wall surface. The model uses a hybrid approach to film modeling: some calculations assume individual particle-based quantities, while other calculations assume film-based quantities.

Table 7.1 lists the parameters selection of main models used in this simulation.

Table 7.1 Parameters selection of the main models

Process	Model	Description of coefficients	Typical value	Selected value
Spray break-up	KH	Model size, B_o	0.61	0.61
		Model breakup time, B_1	5.0-100.0	7.0
	RT	Model breakup time, C_τ	0.1-1.0	1.0
		Model breakup length, C_{bl}	0.0-50.0	1.0
Wall interaction	Wall-film	Critical value for splashing, E^2_{crit}	3330.0	3330.0
		Fraction splashed, f_{flash}	0.5-1.0	1.0
		Rebound Weber number, We_r	0.0-100.0	5.0

In the simulation, a computational domain with the impingement distance of 50 mm was used as shown in Figure. 7.2. The mesh distributed uniformly with the size of 2 mm × 2 mm. The inlet and outlet were set as the cross-flow inlet and outlet. The injection duration was 4 ms, and the injection mass was 4.36 mg. No VCO type nozzle can be selected in CONVERGE, so it caused the spray profile was difficult to meet the experimental results completely. Dry-solvent was used as a test fuel in the experiment, which is a mixture. Its chemical formula is C9-C11, and molecular weight is about 140g. So in this simulation we used Iso-Octane as the test fuel, whose chemical formula is C8H18, and molecular weight is about 114g. The detailed simulation conditions were listed in Table 7.2.

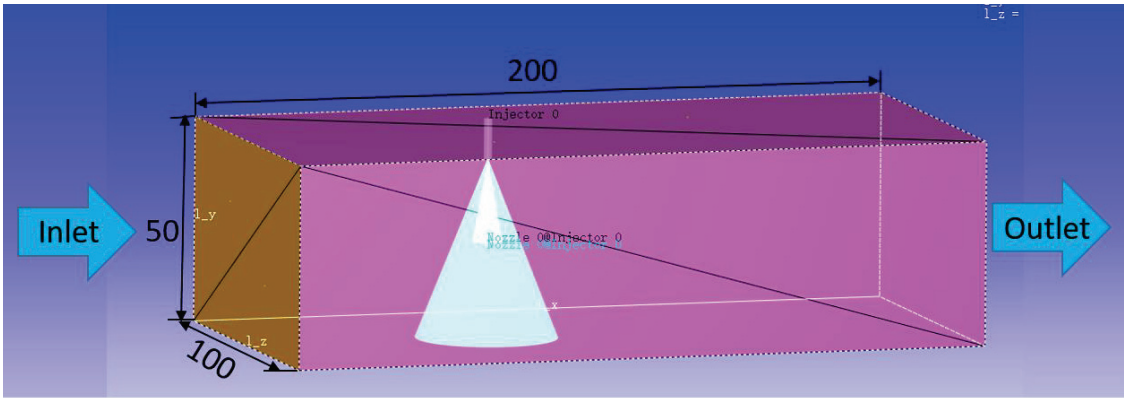

Figure 7.2 Computational mesh for impingement spray simulation (Unit: mm).

Table 7.2 Simulation conditions

	Experiment	Converge
Nozzle	VCO, Single-hole	-
Hole Diameter : d (mm)	0.15	0.15
Fuel	Dry-solvent	Iso-Octane
Injection Pressure : P_{inj} (MPa)	10	-
Injection Duration : T_d (ms)	4	4
Injection Mass : Q_{inj} (mg)	4.36	4.36
Ambient Pressure : P_a (MPa)	0.1, 0.4	0.1, 0.4
Ambient Temperature : T_a (K)	293	293
Cross-flow Velocity : Ux (m/s)	0, 5	0, 5
Impingement Distance : L_w (mm)	50	50

7.2 Spray Structure

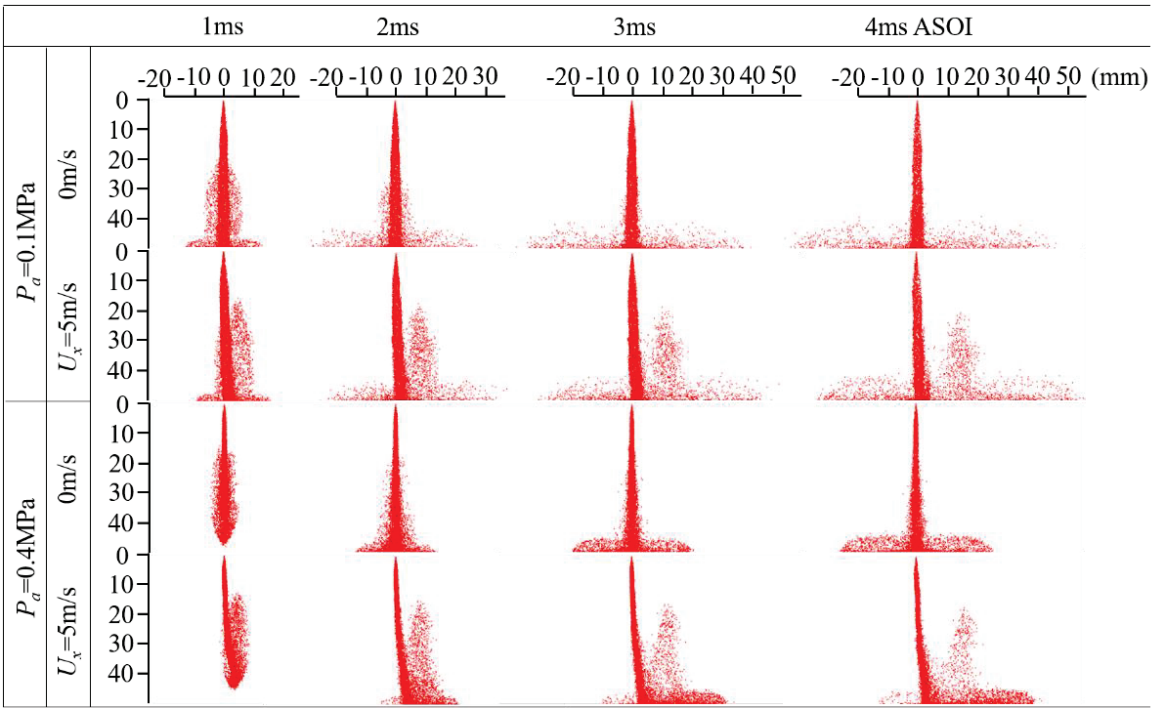

Figure 7.3 Computational Comparisons of the impingement spray evolutions at different cross-flow velocities and ambient pressures.

Figure 7.3 shows the computational comparisons of the impingement spray evolutions at different cross-flow velocities and ambient pressures. Comparing with the experimental results, the tendency of spray development is almost same. The sprays are bended under cross-flow, which is similar to the experimental results. However, the main spray body is thinner and in the upper part of the spray downstream there is no droplet in CFD result. At 4ms ASOI, under cross-flow condition the spray tip in upstream side penetrated shorter than that in quiescent case, which indicated that the cross-flow inhibited upstream spray penetration.

Figure 7.4 shows numerical simulation results of spray structure in three-dimensional space. The measuring time is 4ms ASOI (end of injection). In the simulation results, numerous droplets appear in the downstream side of spray in y = 25 mm horizontal plane, and they are formed by mushroom head breakup, then blew to downstream side. In y = 45 mm horizontal plane, between main spray body and the spray vortex few droplets distributed in this region. This distribution is similar to the experimental results. This indicates the spray height in the region is lower than that of spray vortex region. In addition, compared with experimental results few

droplets appear in the leeward side of main spray body, indicating stripping breakup in simulation was weaker.

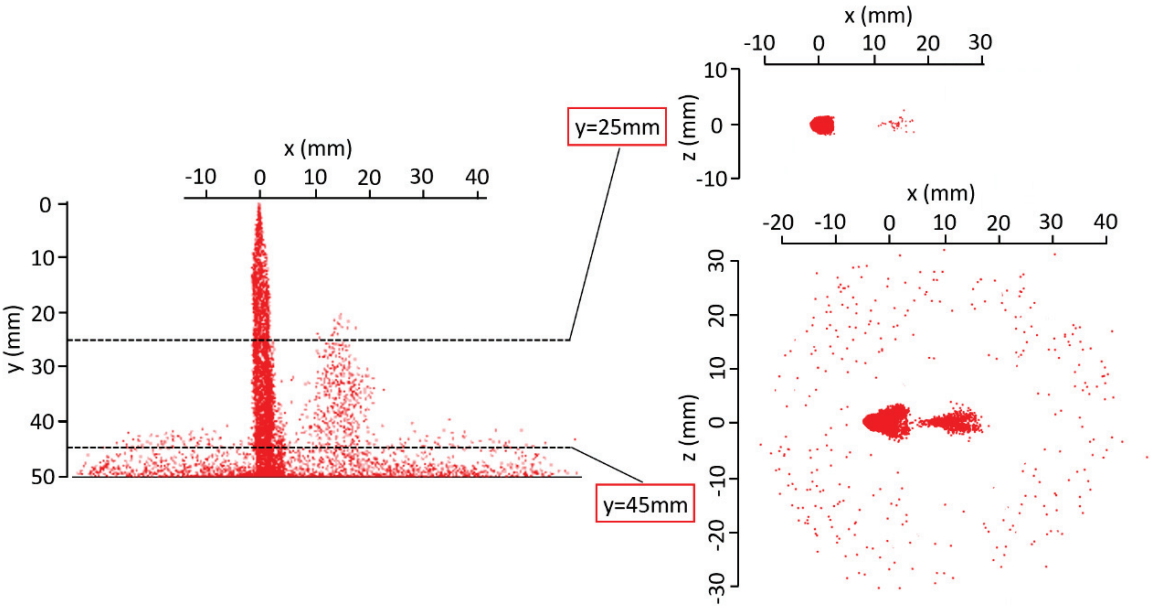

Figure 7.4 Computational spray structure in three-dimensional space at P_a = 0.1 MPa, U_x = 5 m/s, t = 4 ms ASOI.

7.3 Spray Tip Penetration and Vortex Height

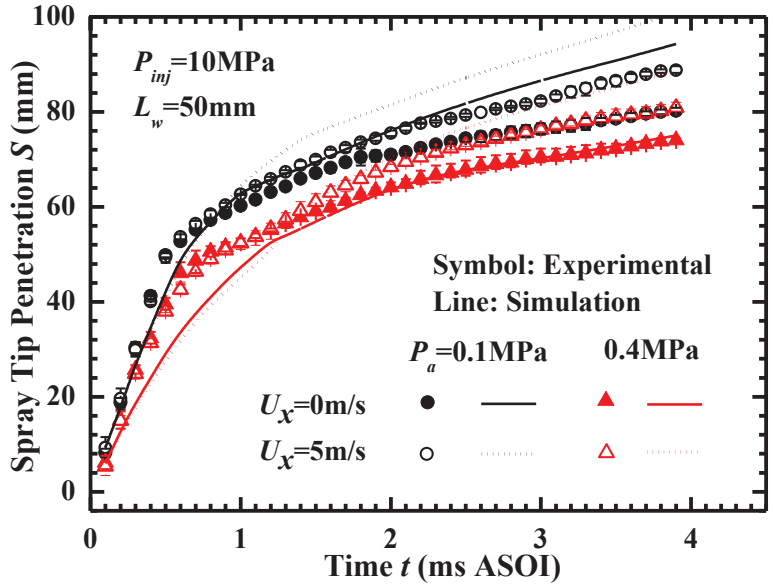

Figure 7.5 Comparisons of spray tip penetration at various cross-flow velocities and ambient pressures.

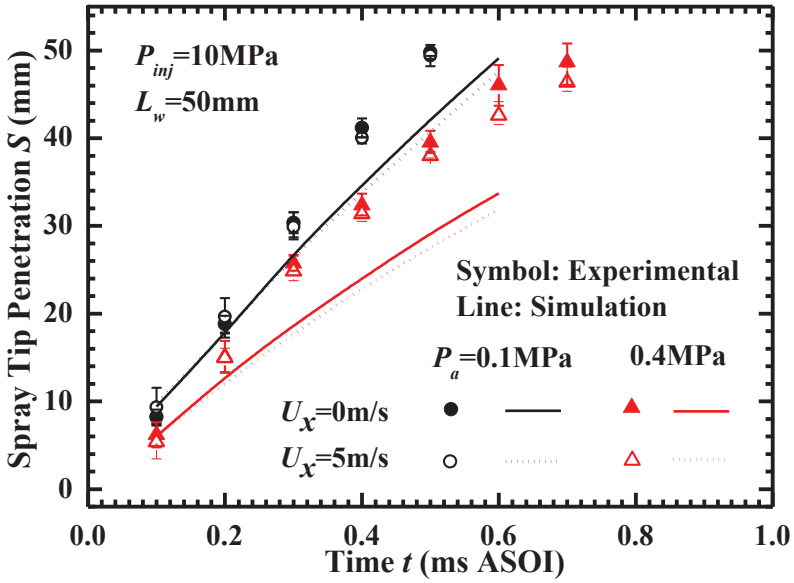

Figure 7.6 Effect of cross-flow velocity and ambient pressure on spray tip penetration of early-stage.

The spray tip penetration under cross-flow velocities of 0 and 5 m/s at different ambient pressures (see Figure 7.5). The comparisons between experimental and CFD results are also shown in here. There are some differences between them. The experimental penetration is smaller than

CFD penetration after impingement. The difference may be caused by the insufficient calculation model of nozzle and break-up models. The two stages of penetration development in the CFD data can be observed clearly.

To clarify the effect of cross-flow on the spray tip penetration before impingement, the penetration results of the early stage of spray evolution were shown in Figure 7.6. When ambient pressure is 0.4 MPa, increasing the cross-flow velocity evidently decreased the penetrations, especially after 0.5 ms ASOI. At early-stage the CFD penetration is smaller than experimental penetration. However, the effect tendency of cross-flow on spray tip penetration showed good agreement with the experimental results.

Increases in the cross-flow velocity tended to a larger vortex height in the cases of 0.1 and 0.4 MPa ambient pressures, as shown in Figure 7.7. When the cross-flow velocity is fixed, the density of ambient air increases at higher ambient pressure, leading to an increased penetration resistance that in turn decreased the momentum of the impingement spray and so reduced the vortex height. The CFD results show a lower vortex height at later injection stage indicating droplets splash and wall-jet vortex movement were weak in wall-film model.

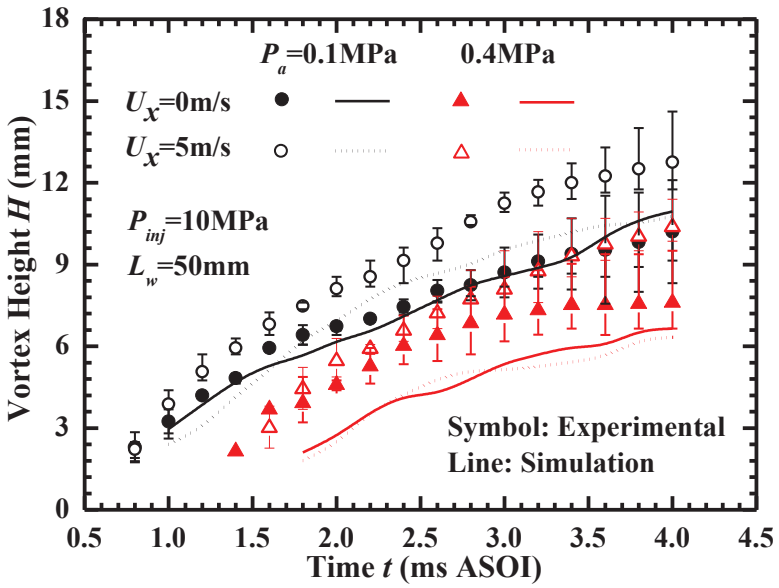

Figure 7.7 Effect of cross-flow velocity and ambient pressures on spray vortex height.

7.4 Droplet Size and Velocity Distributions

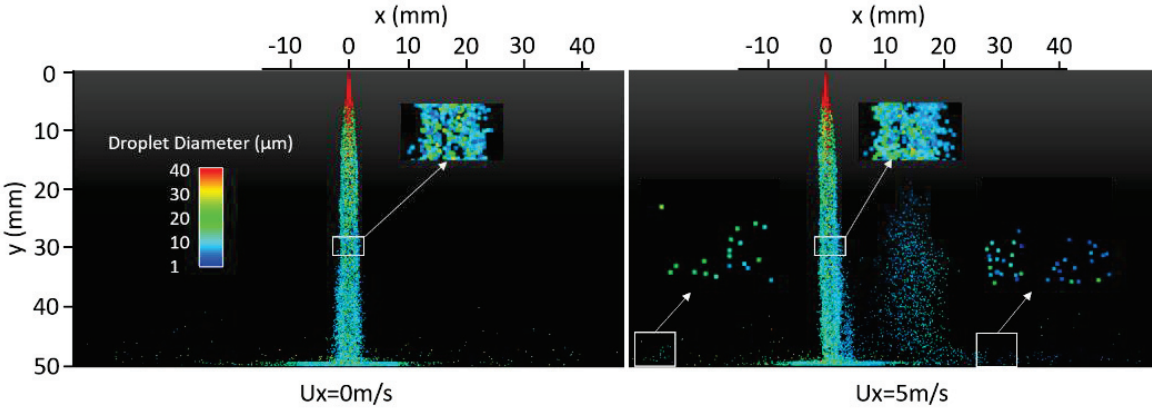

(a) P_a= 0.1MPa

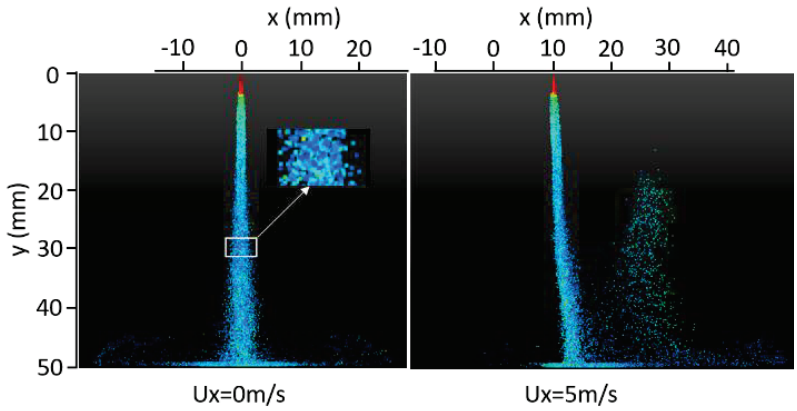

(b) P_a= 0.4MPa

Figure 7.8 Spray droplet size distributions of CFD results.

The droplet size is an important parameter in the fuel atomization, and it influences the air-fuel mixture significantly. Figure7.8 illustrates the effect of cross-flow on the droplet diameter at ambient pressures of 0.1 and 0.4 MPa. Under no-cross-flow condition (see Figure7.8-(a)), the droplet diameter are larger in the upper of the spray than that in the low part. In addition, the atomization in the surface of the spray is better than that of the inner spray and some large droplets exist on the spray center line. For cross-flow velocity of 5 m/s case, large droplets exist on the windward side of spray and small droplets exist on the leeward side of spray. The possible reason is that the tiny droplets can be easy blown to downstream, and then the inner larger droplets with high velocity are exposed in the ambient gas. Moreover, the droplets in downstream shows a smaller diameter compared with that of upstream droplets. It indicates that cross-flow reduces the

droplet coalescence possibility for downstream spray compared with upstream spray. There was a significant decrease of droplet diameter as the ambient pressure increased from 0.1 MPa to 0.4 MPa as shown in Figure7.8-(b). This can be explained by the fact that aerodynamic force increases with increasing ambient gas density, which improves the atomization.

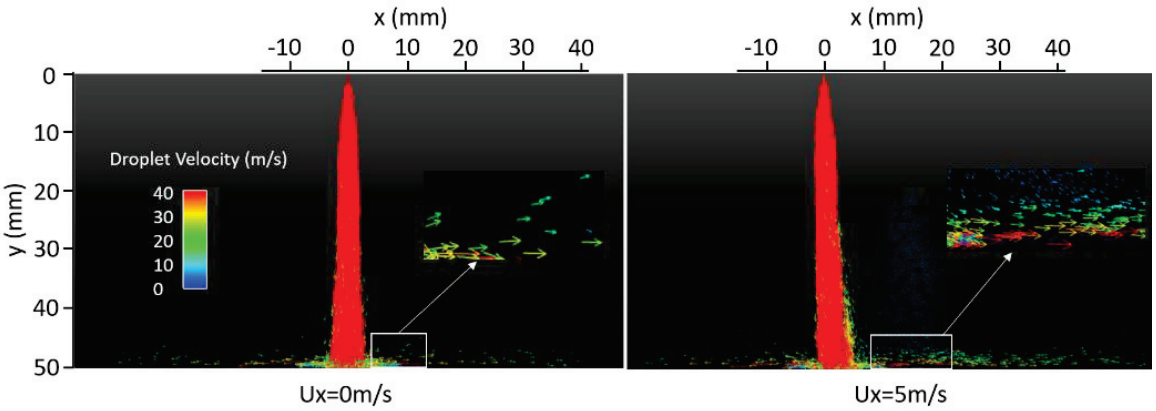

(a) P_a= 0.1MPa

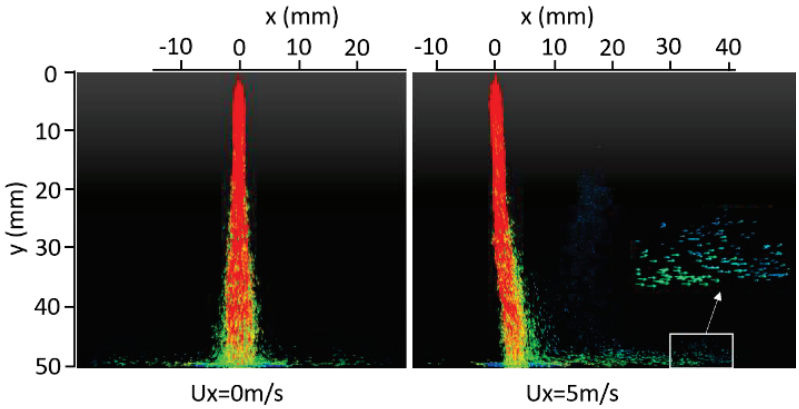

(b) P_a= 0.4MPa

Figure 7.9 Droplets velocity distribution of CFD results.

The droplets velocity distributions under different ambient pressures and cross-flow velocities are shown in Figure 7.9. For Figure7.9-(a), without cross-flow velocity in the radial region (5 mm < x < 15 mm), there were some upward vectors near the impingement region. Andreassi et al. [78] found rebound behavior of droplets in the region. Based on this study, the spray might rebound after impinging on the wall. At cross-flow velocity of 5 m/s case, it is noted that a large number of tiny droplets with low velocity appeared in the leeward side of spray. In the radial region apart from the impingement point (8 mm < x < 22 mm), the post-impingement spray

near the wall moved fast along the wall and the droplet velocity was around 40 m/s. However, the upper part of the post-impingement spray (H > 4 mm) hardly moved. As shown in Figure7.9-(b), with increasing the ambient pressure, the high velocity only exist in the upper part dense region and the velocity is about 30 m/s in the impingement point significantly lower than that in low ambient pressure.

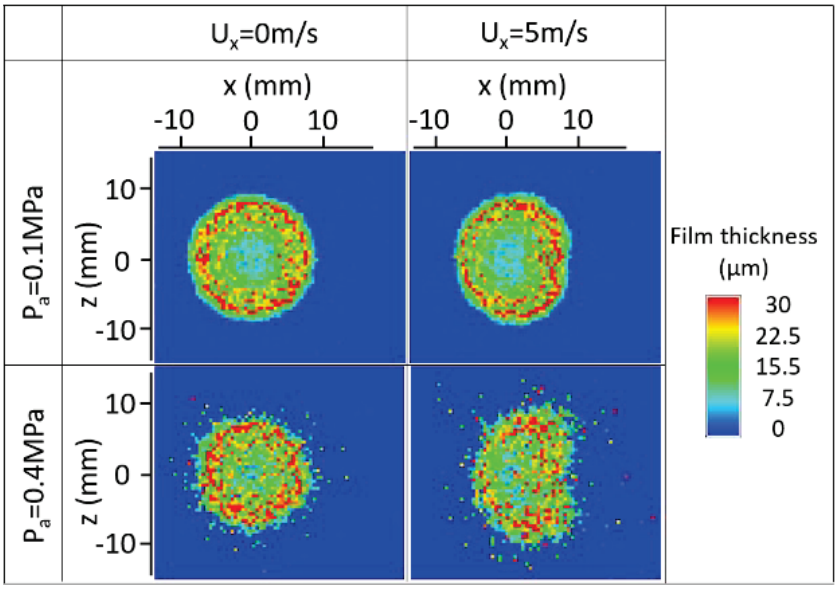

Figure 7.10 Film thickness distribution of CFD results.

Figure 7.10 demonstrates the influence of cross-flow and ambient pressure on fuel film thickness distribution. The time is 4 ms ASOI. It is seen that without cross-flow, the shape of the film is distributed almost circle, however, with cross-flow of 5 m/s, the film width became smaller in cross-flow direction and larger in z direction. Lots of droplets dispersed around the main film area as the ambient pressure rises. This is because the increased ambient pressure leads to the aerodynamic shear stress increased and improves the break-up of spray. In order to get more information for fuel film thickness, the fuel film thickness is depicted in Figure 7.11. There are two peak values at all conditions. Moreover, the thickness range is from 0 to 25 μm. It is observed that at 0.1 MPa condition, without cross-flow the film thickness was almost axisymmetric. However, in the cross-flow of 5 m/s, the film thickness in downstream side was larger than that in upstream side. For U_x = 5 m/s case, with increasing the ambient pressure, film thickness in upstream was decreased. It could be comprehended that the film was shifted to downstream side more due to the larger air momentum flux under high ambient pressure.

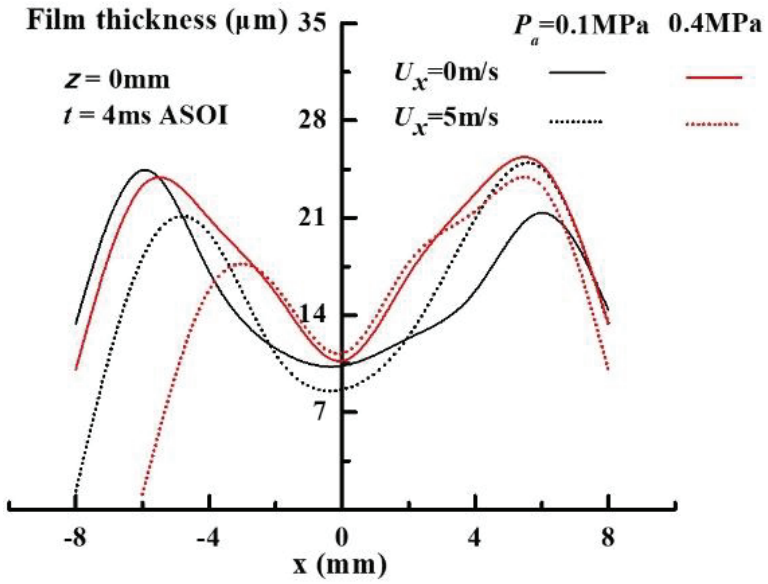

Figure 7.11 Film thickness distribution along x direction of CFD results.

7.5 Summary

The simulation results were taken for analyzing the effects of cross-flow and ambient pressure on the impingement spray. Some results were shown, such as the spray structures, spray tip penetration, vortex height, droplet size and velocity distributions. Although there are some difference between experiment and simulation results, the trend of effect by variable parameters agree well.

For the simulation results, the spray structure variations can illuminate the effect of cross-flow on impingement spray, and it shows the spray distortion under cross-flow condition. The spray tip penetration and vortex height own the same tendencies with the experimental results. For the spray droplet velocity distribution in the vertical plane, at the radial region apart from the impingement point (8 mm < x < 22 mm), the post-impingement spray near the wall moved fast along the wall; however, droplet velocities were small in the upper part (H > 4 mm). Without cross-flow, the shape of the film is distributed almost circle; however, with cross-flow of 5 m/s, the film width became smaller in cross-flow direction and larger in z direction.

Chapter 8 Conclusions

This study is aimed at clarifying the impingement spray characteristics, such as the spray structures, droplet size and velocity distributions of the impingement spray in cross-flow conditions. Dry-solvent was utilized as a test fuel in this study. Three impingement distances L_w were tested (25, 50 and 75 mm) under the cross-flow velocity range from 0 m/s to 50 m/s. The injection pressure was 10 MPa and the ambient pressure varied between 0.1 and 0.4 MPa. For the impingement spray structure observation, a high speed video camera and laser sheet were used in this study. PIA system will be used to measure the droplet size and velocity distribution of local spray. The droplet velocity distribution in wall-jet vortex will be measured by PIV system. A high speed video camera connected with a long-distance microscope was employed to obtain the near-field spray images.

The general results in this study are summarized in this chapter.

8.1 Impingement Spray Structure in Vertical Plane

The impingement spray structure, outline, spray tip penetration and vortex height under different cross-flow velocities, ambient pressures and distance distances were obtained by using a high speed video camera and laser sheet photography.

For the impingement spray structures, after spray impingement on the wall, the spray vertical momentum was converted into radial momentum, and a wall-jet vortex developed along the wall surface, resulting in a lower density for the post impingement spray. Under cross-flow condition, numerous tiny droplets in the middle and bottom of the spray were entrained by cross-flow, flowing to the downstream side. The main spray body was shifted downstream, and the spray trajectory had a large distortion in the windward side. It can be seen that cross-flow promote spray dispersion, and the droplets distributed non-uniformly at the leeward side. Moreover, the spray became dense and the penetration velocity of the spray tip was decreased because increased density of the ambient gas leads to increased air resistance. At smaller impingement distance case, more splashing droplets exited in front of spray vortex. In addition, after impingement the fuel-air mixture area increases with increasing impingement distance.

By the analysis of spray outlines in cross-flow, the cross-flow favors spray dispersion. Moreover, the spray outline distortion caused by cross-flow in the leeward side is larger than that in the windward side. In addition, under an approximate liquid-to-air momentum flux ratio q, when

the ambient pressure and cross-flow velocity were varied, at 2 ms ASOI the outlines of the spray in the windward side agree well, whereas the spray extended further in the leeward side at a lower ambient pressure.

With increase in the cross-flow velocity before impingement, the spray tip penetration decreased slightly, while it evidently increased after impingement. The increased cross-flow velocity led to an increase in the vortex height because of the enhanced spray dispersion. The high ambient pressure restrains the spray dispersion and leads to a shorter spray tip penetration and smaller vortex height. With increasing impingement distance, the spray tip penetration is increased. However, for the spray vortex height, the maximum value presents at 50 mm impingement distance.

8.2 Impingement Spray Structures in Horizontal Planes

Impingement spray images in horizontal planes were obtained by the laser sheet and a high speed video camera. In the middle part of spray the images were taken in the horizontal plane of y = 25mm. And near the wall region the images were taken in 3 mm intervals (from y = 42 mm to y = 48 mm).

In the horizontal plane of y = 25 mm, the movement of the Karman vortex-like structure was observed that resulted in a non-uniform distribution of droplets in the upper part of the spray in the leeward side. With increasing the cross-flow velocity, the fluctuation of spray structure became more obvious because the higher momentum of cross-flow is more easily lead to fluctuation of the liquid flow. In addition, with the increase of ambient pressure, the spray density is increased in the images and the spray fluctuation becomes more severe. Especially at the time of 10 ms ASOI, the shape of spray structure seemed like the letter S.

Near the wall region, with decreasing the distance from the wall surface, the fluctuation phenomenon became weak in the downstream region. It is worth noting that with decreasing the distance from the wall surface, the vacant region between the main spray body and the wall-jet vortex was decreased. In addition, at the plane of y = 45 mm, an empty belt area occurred in the vortex core region revealing that the density of the droplets in this region was quite low.

8.3 Droplet Size and Velocity Distribution of Impingement Spray

By employing the particle image analysis (PIA) optical diagnostic method, the Sauter mean diameter (SMD) and two droplet velocity components were investigated. The droplet velocity distribution in the region of wall-jet vortex was measured by PIV experiment.

Higher cross-flow velocity causes an increased proportion of large droplets in the windward side of spray, and the enhanced droplet breakup, resulting in a larger SMD in the windward side of spray and smaller SMD in the leeward side of spray. In the leeward side of spray, the droplet horizontal velocity gradually increases along the cross-flow direction, and after it reaches approximately the cross-flow velocity, the droplet horizontal velocity shows a large fluctuation in the downstream region. Moreover, the droplet vertical velocity decreases sharply from the center line of the main spray body to the spray periphery. At the downstream region of x = 20 mm, many droplets with negative vertical velocity were detected, and many droplet horizontal velocity was over the cross-flow velocity of 10 m/s at this region due to the interaction between cross-flow and wall-jet. By comparing the velocities of droplets, we found that compared with larger droplets, the smaller droplets are more easily affected by a cross-flow owing to the effect of drag acceleration. In addition, the increased cross-flow velocity leads to the droplet splash region shifting to the downstream side, where numerous secondary droplets are formed during impinging.

In the quiescent ambient, the velocity distribution in spray tip formed as a vortex structure after impingement, while the vortex structure of droplet velocity disappeared with the increase of cross-flow velocity. Detailed droplet velocity distribution of wall-jet vortex was analyzed in quiescent cross-flow velocity ambient at 3 ms ASOI. The droplet velocity of wall main jet was largest in the vortex region. However, in the stagnate region, the droplets velocity is almost 0 m/s.

8.4 Near-Field Spray in Cross-Flow

The effects of the cross-flow and ambient pressure on the near-field spray have been investigated using a long-distance microscopic and high speed video camera. The spray profiles at SOI, MOI and EOI under quiescent ambient and 5 m/s cross-flow with different ambient pressures have been descripted. Gray value distributions in the line of y = 3.75 mm under various cross-flow velocities

and ambient pressures have been discussed. The near-field spray outlines under different cross-flow velocities and ambient pressures were compared.

For near-field spray, the spray image at higher ambient pressure shows fewer ligaments. With increasing cross-flow velocity, the whole spray shifted downstream. The spray outline was wider at the initial stage (0.05ms ASOI) than that at steady stage (2ms ASOI) of spray evolution.

Under cross-flow condition, it can be observed that a large droplets cloud strips from the main body of spray at the time around SOI. The droplets distributions in the windward side and leeside are uneven at MOI. The spray structures at EOI appear diffuse and blurry. Increasing cross-flow velocity tend to form tinier droplets. Thus the cross-flow is beneficial to the fuel spray breakup.

8.5 Numerical Simulation

The simulation results were taken by CONVERGE software for analyzing the effects of cross-flow and ambient pressure on the impingement spray. Although there are some difference between experiment and simulation results, the trend of effect by variable parameters agree well.

For the simulation results, the spray structure variations can illuminate the effect of cross-flow on impingement spray, and it shows the spray distortion under cross-flow condition. The spray tip penetration and vortex height own the same tendencies with the experimental results. For the spray droplet velocity distribution in the vertical plane, at the radial region apart from the impingement point (8 mm < x < 22 mm), the post-impingement spray near the wall moved fast along the wall; however, droplet velocities were small in the upper part (H > 4 mm). Without cross-flow, the shape of the film is distributed almost circle; however, with cross-flow of 5 m/s, the film width became smaller in cross-flow direction and larger in z direction.

8.6 Recommendations for Future Works

More fundamental experiments need to be carried out for future understanding mechanism of the impingement spray and air flow in a real engine, such as the variable parameters of ambient pressure, ambient temperature, wet wall surface and higher cross-flow velocity.

The future work should be conducted at the conditions which are more close to the practical conditions. Firstly, the cross-flow velocity should be increased for observing the spray

fluctuation in the horizontal planes more clearly, which can be taken in the existing experimental device. In addition, the ambient pressure of 0.4 MPa is not high enough compared with the ambient pressure in a DISI engine. Therefore, a gas storage tank with larger volume should be provide in the future experiment. Moreover, the simulations results should be improved by optimizing the models and parameter selections. Moreover, more condition simulations need be carried out, such as changing the parameters of the ambient temperature and fuel.

Reference

[1] Lacis, A.A., Hansen, J.E. Russell, G.L., Oinas, V., and Jonas, J. The role of long-lived greenhouse gases as principal LW control knob that governs the global surface temperature for past and future climate change. *Tellus B* 2013.

[2] Dillon, M.E., Wang, G., and Huey, R.B. Global metabolic impacts of recent climate warming. *Nature* 2010; 467: 704-706.

[3] Schneider, S.H. Global warming: are we entering the greenhouse century. San Franciso, Sierra Club Books; 1989.

[4] Hislop, J. Oil, gas dominate global energy demand to 2040 – Exxon Mobil forecast. 2014. http://theamericanenergynews.com/energy-news/energy-demand-forecasts-exxon-mobil.

[5] Myung, C.L. and Park, S. Exhaust nanoparticle emissions from internal combustion engines: A review. *International Journal of Automotive Technology* 2012; 13(1): 9-22.

[6] Shi, B., Shimokuri, D., and Ishizuka, S. Methane/oxygen combustion in a rapidly mixed type tubular flame burner. *Proceedings of the Combustion Institute* 2013; 34(2): 3369-3377.

[7] Taylor, A.M.K.P. Science review of internal combustion engines. *Energy Policy* 2008; 36: 4657-4667.

[8] Alkidas, A.C. Combustion advancements in gasoline engines. *Energy Conversion and Management* 2007; 48: 751-2761.

[9] Moon, S., Choi, J., Abo-Serie, E., and Bae, C. The effects of injector temperature on spray and combustion characteristics in a single cylinder DISI engine. *SAE Technical Paper*, 2005-01-0101, 2005.

[10] Harada, J., Tomita, T., Mizuno, H., Mashiki, Z, and Ito, Y. Development of direct injection gasoline engine. *SAE Technical Paper, 970540,* 1997.

[11] Imberdis, O., Hartmann, M., Bensler, H., Kapitza. L., and Thevenin, D. A numerical and experimental investigation of a DISI-engine intake port generated turbulent flow. *SAE Technical Paper,* 2007-01-4047, 2007.

[12] Tagaki, Y., Itoh, T., Muranaka, S., Iiyama, A., Iwakiri, Y., Urushihara, T., and Naitoh, K. Simultaneous Attainment of Low Fuel Consumption, High Output Power and Low Exhaust Emissions in Direct Injection SI Engines. *SAE Technical Paper*, 980149, 1998.

[13] Drake, M.C., Fansler, T.D., Solomon, A.S., and Szekely, G.A. Piston fuel films as a source

of smoke and hydrocarbon emissions from a wall-controlled spark-ignited direct-injection engine. *SAE Technical Paper*, 2003-01-0547, 2003.

[14] Drake, M.C., Fansler, T.D., Lippert, A.M. Stratified-charge combustion: modeling and imaging of a spray-guided direct-injection spark-ignition engine. *Proceedings of the Combustion Institute* 2005; 30: 2684-2691.

[15] Zhao, F.Q., Lai, M.C., and Harrington, D.L. Automotive spark-ignited direct-injection gasoline engines. *Progress in Energy and Combustion Science* 1999; 25: 437-562.

[16] Chigier, N. Group combustion models and laser diagnostic methods in sprays: A review. Combustion and Flame 1983. 51: 127-139.

[17] Katashiba, H., Honda, T., Kawamoto, M., Sumida, M., Fukutomi, N., and Kawajiri, K. Improvement of center injection spray guided DISI performance. *SAE Technical Paper,* 2006-01-1001, 2006.

[18] Schwarz, C., Schunemann, E., Durst, B., Fischer, J., and Witt, A. Potentials of the spray-guided DI combustion system. *SAE Technical Paper*, 2006-01-1265, 2006.

[19] Szekely, G.A., Alkida, A. Combustion characteristics of a spray-guided direction stratified-charge engine with a high-squish piston. *SAE Technical Paper*, 2005-01-1937, 2005.

[20] Koch, T., Schanzlin, K., Boulouchos, K. Characterization and phenomenological modeling of mixture formation and combustion in a direct injection spark ignition engine. *SAE Technical Paper,* 2002-01-1138, 2002.

[21] Schanzlin, K., Koch, T., Tzannis, A.P., and Boulouchos, K. Characterization of mixture formation in direct injected spark ignition engine. *SAE Technical Paper*, 2001-01-1909, 2001.

[22] VanDerWege, B.A., Han, Z., and Lyer, C.O. Development and analysis of a spray-guided DISI combustion system concept. *SAE Technical Paper*, 2003-01-3105, 2003.

[23] Boot, M., Rijk, E., Luijten, C., et al. Spray impingement in the early direct injection premixed charge compression ignition regime. *SAE Technical Paper*, 2010-01-1501, 2010.

[24] Kim, Y.J., Lee, S.H., Cho, N.H. Effect of air motion on fuel spray characteristics in a gasoline direct injection engine. *SAE Technical Paper*, 1999-01-0177, 1999.

[25] Hiroyasu, H. and Arai, M. Structures of fuel spray in diesel engines. *SAE Technical Paper*, 900475, 1990.

[26] Dent., J.C. A basis for the comparison of various experimental methods for studying spray

penetration. *SAE Technical Paper*, 710571, 1971.

[27] Fujimoto, H., Sugihara, H., Tanabe, H., and Sato, G.T. Investigation on combustion in medium speed marine diesel engines using model chambers. *CIMAC-Congress*, Helsinki, 1981.

[28] Heywood, J.B. Internal combustion engine fundamentals. *Singapore: McGraw-Hill Book Company*, 1988.

[29] Dan, T., Takagishi, S., Senda, J., and Fujimoto, H. Organized structure and motion on diesel spray. *SAE Technical Paper*, 970641, 1997.

[30] Reitz, R.D., and Bracco, F.V. Mechanisms of breakup of round liquid jets. *Encyclopedia of Fluid Mechanics*, Gulf Pub, NJ 1986; 3: 233-249.

[31] Hiroyasu, H. and Arai, M., and Tabata, M. Empirical equations for the Sauter mean diameter of a diesel spray. *SAE Technical Paper*, 890464, 1989.

[32] Hiroyasu, H. and Nishida, K. Fuel spray trajectory and dispersion in a D.I. diesel combustion chamber. *SAE Technical Paper*, 890462, 1989.

[33] Hiroyasu, H., Shimizu, M., and Arai, M. Breakup length of a liquid jet and internal flow in a nozzle. *ICLASS-91*, 1991.

[34] Chehroudi, B., Chen, S.H., Bracco, F.V., and Onuma, Y. On the intact core of full-cone spray. *SAE Technical Paper*, 850126, 1985.

[35] Youle, A.J. and Salters, D.G. A conductivity probe technique for investigating the breakup of diesel sprays. *Atomization and sprays* 1994; 4: 253-262.

[36] He, L. and Ruiz, F. Effect of cavitation on flow and turbulence in plain orifices for high speed atomization. *Atomization and sprays*, 1995; 5: 569-584.

[37] Gülder, Ö.L., Smallwood, G.J., and Snelling, D.R. Diesel spray structure of transient full cone dense diesel sprays. *Commodia* 1994; 94: 355-360.

[38] Soteriou, C., Andrews, R., Smith, M., and Kunkulagunta, T. Through the diesel nozzle-a journey of discovery II, *ILASS-Europe*, Zürich, 2001.

[39] Wu, P.K. and Faethe, G.M. Onset and end of drop formation along the surface of turbulent liquid jet in still gases. *Phys. of Fluids* 1995; 7(11): 2915-2917.

[40] Arai, M., Shimizu, M., and Hiroyasu, H. Similarity between the breakup lengths of a high speed liquid jet in atmospheric and pressurized conditions. *Los Alamos National Laboratory*, 1991.

[41] Soteriou, C., Andrews, R., and Smith, M. Direct injection diesel sprays and the effect of cavitation and hydraulic flip on atomization. *SAE Technical Paper*, 950080, 1995.

[42] Tamaki, N., Shimizu, M., and Hiroyasu, H. Enhanced Atomization of a liquid jet by cavitation in a nozzle hole. *8th Int. Conf. on Liquid Atomization and Spray Systems*, Pasadena, CA, USA, 2000.

[43] Peterson, B. R..High-speed fuel and flow imaging to investigate misfires in a spray-guided direct-injection engine. University of Michigan, 2010.

[44] Moon, S., Bae, C., Choi, J., Abo-Serie, E. The influence of airflow on fuel spray characteristics from a slit injector. *Fuel* 2007; 86: 400-9.

[45] Guo, M., Nishida, K., Ogata, Y., Wu, CQ., Fan, QR. Experimental study on fuel spray characteristics under atmospheric and pressurized cross-flow conditions, second report: Spray distortion, spray area, and spray volume. *Fuel* 2017; 206: 401-8.

[46] Panão, M.R.O., Moreira, A.L.N., Durão, D.F.G. Effect of a cross-flow on spray impingement with port fuel injection systems for HCCI engines. *Fuel* 2013; 106: 249-57.

[47] Padala, S., Le, M.K., Kook, S., Hawkes, E.R. Imaging diagnostics of ethanol port fuel injection sprays for automobile engine applications. *Appl. Thermal Eng.* 2013; 52(1): 24-37.

[48] Lee, S., Kim, W., Yoon, W. Spray formation by a swirl spray jet in low speed cross-flow. *J. Mech. Sci. Technol.* 2010; 24(2): 559-68.

[49] Getsinger, D.R., Gevorkyan, L., Smith, O.I., Karagozian, A.R. Structural and stability characteristics of jets in crossflow. *J Fluid Mech.* 2014; 760: 342-67.

[50] Sinha, A., Prakash, R.S., Mohan, A.M., Ravikrishna, R.V. Airblast spray in crossflow–structure, trajectory and droplet sizing. *Int J Multiphase Flow* 2015; 72: 97–111.

[51] Ng, C.L., Sankarakrishnan, R., Sallam, K.A. Bag breakup of nonturbulent liquid jets in crossflow. *Int J Multiphase Flow* 2008; 34: 241–59.

[52] Yarin, A.L., Weiss, D.A. Impact of drops on solid surfaces: self-similar capillary waves, and splashing as a new type of kinematics discontinuity. *J Fluid Mech* 1995; 283:141–173.

[53] Panão, M.R.O., Moreira, A.L.N. Visualization and analysis of spray impingement under cross-flow conditions. *SAE Technical Paper* 2002; 2002-01-2664.

[54] Panão, M.R.O., Moreira, A.L.N. Spray impingement on a flat plate under cross-flow conditions. Zaragoza, Spain: ILASS-Europe 2002.

[55] Arcoumanis, C., Whitelaw, D.S., Whitelaw, J.H. Gasoline injection against surfaces and films. *Atomization and Sprays* 1997; 7(4): 437-56.

[56] Moriyoshi, Y., Uchida, R., Takagi, M., Kubota, M. Numerical and experimental analyses of mixture formation process using a fan-shaped DI gasoline spray: examinations on effects of crosswind and wall impingement. *SAE Technical Paper* 2009; 2009-01-1502.

[57] Panão, M.R.O., Moreira, A.L.N. Experimental study of the flow regimes resulting from the impact of an intermittent gasoline spray. *Exp. Fluids* 2004; 37: 834–55.

[58] Arcoumanis, C., Cutter, P.A. Flow and heat transfer characteristics of impinging diesel sprays under cross-flow conditions. *SAE Technical Paper* 1995; 950448.

[59] Andreassi, L., Facci, A.L., Krastev, V.K., Ubertini, S. Multidimensional modelling of gaseous injection: Analysis of an impinging jet. *International Journal of Heat and Fluid Flow* 2010, *31*(5), 909-915.

[60] Yu, H., Liang, X., Shu, G., Wang, Y., Zhang, H. Experimental investigation on spray-wall impingement characteristics of n-butanol/diesel blended fuels. *Fuel* 2016, 182: 248-258.

[61] Zhan, C., Feng, Z., Zhang, M., Tang, C., Huang, Z. Experimental investigation on effect of ethanol and di-ethyl ether addition on the spray characteristics of diesel/biodiesel blends under high injection pressure. *Fuel* 2018, 218: 1-11.

[62] Zama, Y., Sugawara, K., Akop, M. Z., Furuhata, T., Arai, M. Experimental study on velocity distribution of postimpingement diesel spray on a wall. Part 1: Effect of impingement angle on flow pattern. *Atomization and Sprays* 2014, 24(8):723-746.

[63] Bae, C., Kang, J. The structure of a break-up zone in the transient diesel spray of a valve-covered orifice nozzle. *Int J Engine Res* 2006; 7: 319–34.

[64] Tang, C., Guan, L., Feng, Z., et al. Effect of di-n-butyl ether blending with soybean-biodiesel on the near-nozzle spray characteristics. *Fuel* 2017; 191: 300-11.

[65] Tajima, K., Tsuru, D., Kawauchi, S., and Kato, H. Spray model verification via observation of diesel spray propagation in parallel flow field to injection direction. *ILASS-Japan 2011*; 194-198.

[66] Klopfenstein, R. Air velocity and flow measurement using a Pitot tube, *ISA Transactions* 1998, 37: 257-263.

[67] Motallebi, F. A review of the hot-wire technique in 2-D compressible flows. *Prog. Aerospace Sci. 1994*; 30: 267-294.

[68] Bhatia, J.C., Durst, F., and Jovanovic, J. Corrections of hot-wire anemometer measurements near walls, *J. Fluid Mech.* 1982, 122: 411-431.

[69] Andrews, G.E., Bradley, D., and Hundy, G.F. Hot wire anemometer calibration for measurements of small gas velocities, *Int. J. Heat Mass Transfer* 1972, 15: 1765-1786.

[70] Khalighi, B. and Huebler, M.S. A transient water analogue of a dual-intake-valve engine for intake flow visualization and full-field velocity measurements. *SAE Technical Paper,* 880519, 1988.

[71] Zhao, H., and Ladommatos, N. Engine combustion instrumentation and diagnostics, *Society of Automotive Engineers, Inc.*, 2001.

[72] Baumgarten, C. *Mixture Formation in Internal Combustion Engines*. Spring-Verlag Berlin Heidelberg New York, 2006.

[73] Kong, J. and Bae, C. Effect of nozzle hole geometry on non-evaporating diesel spray characteristics at high-pressure injection. *Atomization and Sprays* 2012, 22: 1-22.

[74] Katsura, N., Saito, M., Senda, J., et al. Characteristics of a diesel spray impinging on a flat wall. *SAE Technical Paper* 1989; 890264.

[75] Guo, M., Kishi, R., Shi, B., Ogata, Y., Nishida, K. Effects of cross-flow on fuel spray injected by hole-type injector for direct-injection gasoline engine. Second report: Spray pattern, droplet size, and vortex structure. *Atomization and Sprays* 2016; 26(1): 53-72.

[76] No, S.Y. Empirical correlations for penetration height of liquid jet in cross flow–a review. Estoril, Portugal: ILASS-Europe 2011.

[77] Guo, M., Shimasaki, N., Nishida, K., et al. Experimental study on fuel spray characteristics under atmospheric and pressurized cross-flow conditions. *Fuel* 2016; 184: 846-55.

[78] Andreassi, L., Ubertini, S., Allocca, L. Experimental and numerical analysis of high pressure diesel spray–wall interaction. *Int J Multiph Flow* 2007; 33(7): 742–65.

[79] Zhang, Y., Jia, M., Liu, H., et al. Development of a new spray/wall interaction model for diesel spray under PCCI-engine relevant conditions. *Atomization Sprays* 2014; 24(1): 41–80.

[80] Mundo, C.H.R., Sommerfeld, M., Tropea, C. Droplet-wall collisions: experimental studies of the deformation and breakup process. *Int J Multiph Flow* 1995; 21(2):151-73.

[81] Guan, L., Tang, C., Yang, K., et al. Effect of di-n-butyl ether blending with soybean-biodiesel on spray and atomization characteristics in a common-rail fuel injection system.

Fuel 2015; 140: 116-25.

[82] Zdravkovich, M.M. *Flow around circular cylinders: vol 1: fundamentals*, Oxford 1997; 79-85.

[83] Luo, H.L., Nishida, K., Uchitomi, S., et al. Microscopic behavior of spray droplets under flat-wall impinging condition. *Fuel* 2018; 219: 467-76.

[84] Leong, M.Y., McDonell, VC., Samulesen, S. Mixing of an airblast atomized fuel spray injected into a crossflow of air. *NASA/CR* 2000; 210467.

[85] Bai, C. X., Rusche, H., Gosman, A.D. Modeling of gasoline spray impingement. *Atomization and Sprays 2012*, *12*:1-3.

[86] Lee, S.H., Ryou, H.S. Comparison of spray/wall impingement models with experimental data. *J Propul Power* 2000; 16(6):939–45.

[87] Busch R. Untersuchung von Kavitationsphänomenen in Dieseleinspritzdüsen Ph.D. Thesis. Germany: University of Hannover; 2001.

[88] Huethorst, J.A.M. and Marra, J. Motion of marangeoni-contracted water drops across inclined hydrophilic surface. *Langmuir* 1991; 7: 2756-2763.

[89] Liu, A.B. and Reitz, R.D. Modeling the effects of drop drag and break-up on fuel spray. *SAE Technical Paper*, 930072, 1993.

[90] Launder, B.E. and Spalding, D.B. The numerical computation of turbulent flows. *Comp. Meth. Appl. Mech. Eng.* 1974; 3: 269-289.

[91] Su, T.F., Patterson, M.A., Reitz, R.D., and Farrell, P.V. Experimental and Numerical Studies of High Pressure Multiple Injection Sprays, *SAE Technical Paper*, 960861, 1996.